BRNO UNIVERSITY OF TECHNOLOGY
VYSOKÉ UČENÍ TECHNICKÉ V BRNĚ

FACULTY OF MECHANICAL ENGINEERING
FAKULTA STROJNÍHO INŽENÝRSTVÍ

INSTITUTE OF SOLID MECHANICS, MECHATRONICS AND BIOMECHANICS
ÚSTAV MECHANIKY TĚLES, MECHATRONIKY A BIOMECHANIKY

DUCTILE FRACTURE CRITERIA IN MULTIAXIAL LOADING – THEORY, EXPERIMENTS AND APPLICATION
DUCTILE FRACTURE CRITERIA IN MULTIAXIAL LOADING – THEORY, EXPERIMENTS AND APPLICATION

DOCTORAL THESIS
DIZERTAČNÍ PRÁCE

AUTHOR — **Ing. František Šebek**
AUTOR PRÁCE

SUPERVISOR — **prof. Ing. Jindřich Petruška, CSc.**
ŠKOLITEL

BRNO 2016

Abstrakt

Práce se zabývá tvárným lomem, který je výsledkem víceosého kvazi-statického monotónního namáhání doprovázeného rozsáhlými plastickými deformacemi, přičemž pro degradaci materiálu je uvažován lokální přístup. Ve výpočtech o rozvoji poškození rozhodují použité mezní podmínky tvárného lomu. Tyto byly teoreticky studovány v úvodu práce a po výběru vhodné mezní podmínky byl stanoven postup kalibrace. Dále byl rozpracován plán měření a realizovány zkoušky při pokojové teplotě na slitině hliníku 2024-T351, zahrnující tah, krut a tlak, pro studium rozvoje poškození a věrohodnou kalibraci vybraného fenomenologického modelu tvárného porušování, vyjádřeného pomocí lomového přetvoření a závislého na hydrostatickém tlaku a deviátoru tenzoru napětí. Mezní podmínka tvárného lomu byla posléze svázána s podmínkou plasticity. Plasticita byla pro zkoumaný materiál uvažována ve tvaru zohledňujícím i stav třetího invariantu deviátoru tenzoru napětí. Celý navržený přístup, plně aplikovatelný na víceosé úlohy, byl implementován pomocí uživatelské rutiny do komerčního programu založeného na explicitní variantě metody konečných prvků. V závěru práce je předložena aplikace navrženého přístupu k modelování tvárného porušování v podobě verifikace na vybraných zkušebních testech, z níž plynou závěry a doporučení pro další práci.

Klíčová slova

Tvárné porušování, mechanika poškození kontinua, explicitní metoda konečných prvků, kumulace poškození, změkčení materiálu, slitina hliníku.

Abstract

This thesis is concerned with ductile fracture, which is a result of multiaxial quasi-static monotonic loading accompanied with large plastic deformations, while the local approach is considered for material degradation. In computations, the damage evolution is governed by used ductile fracture criteria. These were theoretically studied in the introduction, and the calibration procedure was proposed after the choice of suitable fracture criterion. Next, the experimental program was designed, and the tests on aluminium alloy 2024-T351, concerning tension, torsion and compression, were realized at a room temperature for the investigation of damage accumulation and reliable calibration of chosen phenomenological ductile fracture criterion, expressed through the fracture strain, and dependent on the hydrostatic pressure and deviatoric stress tensor. The ductile fracture model was then coupled with the yield criterion. Plasticity was considered in the form of taking into account the state of third invariant of deviatoric stress tensor as well for investigated material. The whole proposed approach that is fully applicable to multiaxial problems was implemented using user subroutine into the commercial software, based on the explicit finite element method. In the end, the application of the proposed approach to modelling of ductile fracture is presented in the form of verification using chosen specimens, resulting in the conclusions and recommendations for future studies.

Keywords

Ductile fracture, continuum damage mechanics, explicit finite element method, damage accumulation, material weakening, aluminium alloy.

Declaration of originality

I, Ing. František Šebek, hereby declare that I have written this Ph.D. thesis on my own under the supervision of prof. Ing. Jindřich Petruška, CSc. I also declare that I have fully cited and referenced all information and results that are not original to this work.

Brno, 20. 07. 2016 Ing. František Šebek

Acknowledgement

I would like to express my deepest gratitude to my supervisor, prof. Ing. Jindřich Petruška, CSc., not only for his continuous guidance, priceless advice and inspiring comments, but also for support and sincere kindness throughout the whole study and research.

Contents

1 Introduction

"Science does not exist until it is published."

Drummond Rennie [90]

1.1 Motivation

The problem of ductile fracture in general has become motivating for engineers since *the Industrial Revolution*. With the onset of the industrialization and widespread use of various structural steels and alloys, the problem of fracture has occurred. Bridges and buildings have been constructed from structural steels. The aircraft, automotive, marine, railway and more other engineering fields have started to use metals. It has begun to be challenging to predict fractures in such sectors, especially where human factors and casualties have played a role. Finished products, assemblies, machinery, or structures may be subjected to extreme straining due to accidents, such as train wrecks, traffic collisions, aviation accidents, ship collisions or failures in nuclear or civil engineering. In such cases, it is a great task for engineers to predict the ductile fracture reliably.

There is also an amount of forming operations in industrial applications where large plastic deformations occur. Semi-finished products may be subjected to various shaping operations such as bending and twisting, or to forming operations such as forward extrusion, where the fracture is not desirable. On the other hand, material separation processes such as machining, cutting, or trimming – where violating the material integrity is intentional – are applied to semi-finished products before those get the required geometry and properties. Moreover, business competitiveness implies necessity of handling such processes in the most effective way. Therefore, many approaches to ductile fracture [111, 120, 212], more or less complex, have been proposed. However, the literature and experiences reveal that the statement "the more complicated the model, the better the reliability" does not necessarily apply. It may be stated that the more the model is sophisticated, the more expensive is the calibration and the more difficult is the application. It makes such models more academic, and less accessible in industry, so a compromise should be found.

However, it is worth noting that the fracture itself and its using have been as old as the human race.

1.2 Background and scope of research

Nowadays, the accurate prediction of ductile fracture has been extensively explored by many researchers, institutes and industrial companies [54, 88, 99, 179, 202], as described further. This thesis deals with *the ductile fracture* in the broader sense and does not concern the classical fracture mechanics as in [110, 176]. In this case, the concept of ductile fracture refers to large plastic energy consuming deformations of ductile polycrystalline metals under monotonic quasi-static loading conditions, as illustrated in Figure 1.1.

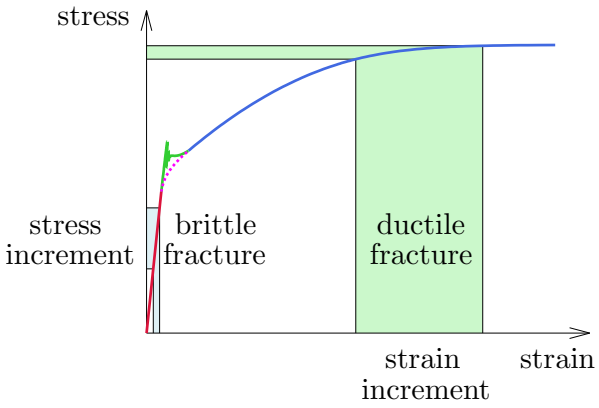

Figure 1.1: Different resolution for brittle and ductile fracture, respectively, [138].

Large plastic deformations refers to hundreds of percent in the present study. The whole problem is solved from the very beginning, when the virgin material is without any damage, although there may be an initial amount present. The local approach focuses on a material point where the damage is accumulated. The damage is tracked within the whole solid subjected to straining until the crack initiates and grows. In the final stage of the process, there may be material separation into two or more individual pieces. Moreover, the number of cracks is not limited, and these may occur simultaneously or subsequently in any part of observed solid.

Many approaches have been developed on how to model the crack initiation and propagation within *Finite Element Method* (FEM). *The element deletion technique* is one of the most spread in the scope of ductile fracture. This method, where the element that satisfies certain criterion is deleted, is adopted in this work. Actually, elements are not physically deleted, but stresses are set to zero, and zero stress and strain increments are passed for all deleted material points [223]. It may be easily used together with *adaptive remeshing*. There is also *a nonlocal damage approach*, besides the local point of view, which is based on weighted averaging of certain variable over a spatial neighbourhood of a material point. It solves the problem of mesh sensitivity and state variable localization [70, 91, 147, 165]. The next technique may be *the node separation method* based on separating nodes of element, in which the fracture criterion is satisfied, and its neighbouring elements [85, 114, 193]. Physical meaning of this method is clearer in contrast to previous one. Belitschko and Black [92] laid foundation of *eXtended Finite Element Method* (XFEM) on the basis of *partition of unity method* proposed by Melenk and Babuška [82]. Discontinuities in elements are allowed by enriching the degrees of freedom with special displacement functions and the method is not dependent on the finite element mesh [223].

Another approach to ductile fracture may be *cohesive zone models* [199]. These are based on a strip-yield model proposed by Barenblatt [29]. Dugdale [32] introduced similar model concerning the plastic zone ahead of a crack tip. Material behaviour of extended crack tip is described by the traction-separation law, or cohesive law, and the crack path has to be assumed or known in advance. Although cohesive elements could be used for all pairs of nodes [76], it is not practical due to high computational costs. As it is not such versatile approach as those reviewed in Chapter 4, it will not be described further.

Different discretization methods such as *finite cell method* may also be used for ductile fracture prediction [136, 211]. This method combines higher-order methods with fictitious or embedded domain approach. The original domain is embedded in a larger domain of a simpler shape, which may be easily meshed by rectangular or hexahedral elements with high convergence rate. Another family of methods are meshless ones. *Smoothed Particle Hydrodynamics* proposed by Gingold and Monaghan [51] is based on particles representing a given body, of which contributions are computed on the basis of neighbouring particles within a sphere of influence. It should be noted that the method is not based on discrete particles colliding with each other in compression and exhibiting a cohesive behaviour in tension. Instead, it is discretization method of continuum partial differential equations [223]. Another widespread mesh-free method is *Element Free Galerkin* introduced by Belitschko et al. [79]. The method uses nodes having a domain of influence. This domain does not depend on the nodes arrangement as depicted in Figure 1.2. Shape functions are formulated by applying the moving least squares approximation [59], while the approximation function is restricted to the node domain of influence [188].

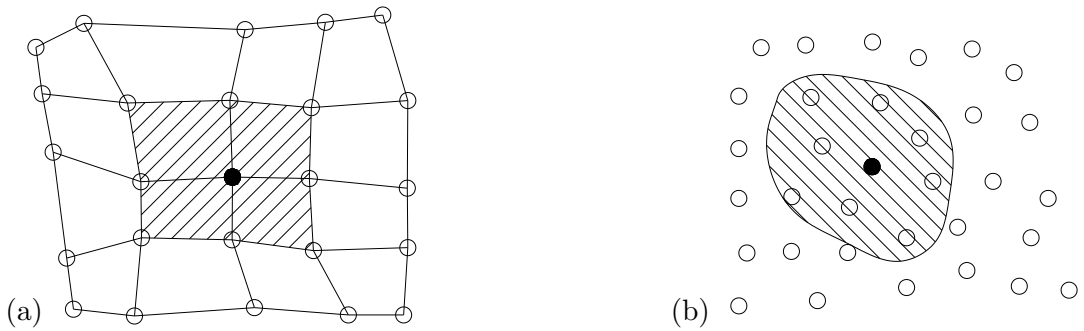

Figure 1.2: The domain of influence for: (a) the numerical method with nodal connectivity where the domains of solid nodes are shared; (b) meshless method [188].

The explicit FEM was used in the present study for advantages when compared to implicit formulation, which might fail to converge when solving severe discontinuities. Advantages include better handling of complicated contact conditions, accessibility of parallelization and computer time saving in case of very large problems [131]. The implicit code was, among others, used in some calibration processes within Abaqus/Standard. Vectorized User MATerial (VUMAT) subroutine was used within Abaqus/Explicit when the explicit integration scheme was used in scope of ductile fracture modelling. Version 6.14 of Abaqus/CAE was used within the present thesis.

1.3 Objectives of the study

Various ductile fracture models have been developed, as described further, since the second half of the last century. The main goals may be summarized in the following points:

- To theoretically and experimentally study the multiaxial ductile fracture criteria and their application in the scope of Continuum Damage Mechanics (CDM). The main focus deals especially with the experimental program carried out on Aluminium Alloy (AA) 2024-T351 in order to reliably calibrate chosen continuum damage model.
- To conduct the study of nonlinear damage accumulation and its influence on the prediction of the ductile fracture. A special attention is paid to the problem of material weakening and to the estimation of related material constants.
- To discuss the prediction capability and reliability of suggested approaches using verification on existing fracture tests.

2 Characterization of the stress state

The characterization of the stress state shall follow the introduction, because some terms are not used uniformly, consistently, or even correctly.

2.1 Stress state related variables

The stress state is based on three stress invariants using the Cauchy stress tensor $\boldsymbol{\sigma}$ and deviatoric stress tensor which states

$$\mathbf{S} = \boldsymbol{\sigma} + p\mathbf{I}, \tag{2.1}$$

where p is the hydrostatic pressure and $\mathbf{I}$ is the identity matrix. Then, the first invariant of the Cauchy stress tensor is defined as

$$I_1 = \mathrm{tr}(\boldsymbol{\sigma}). \tag{2.2}$$

Second and third invariants of the deviatoric stress tensor are, respectively,

$$J_2 = \frac{1}{2}\mathbf{S} : \mathbf{S}, \tag{2.3}$$

$$J_3 = \det(\mathbf{S}). \tag{2.4}$$

Using the plastic strain tensor $\boldsymbol{\epsilon}^p$, the deviatoric plastic strain may be expressed as

$$\mathbf{e}^p = \boldsymbol{\epsilon}^p - \frac{1}{3}\mathrm{tr}(\boldsymbol{\epsilon}^p)\mathbf{I}. \tag{2.5}$$

Assumption of plastic incompressibility, or volume constancy, gives $\mathrm{tr}(\boldsymbol{\epsilon}^p) = 0$, so the Equation 2.5 yields in $\mathbf{e}^p = \boldsymbol{\epsilon}^p$, which implies the deviatoric plastic strain tensor is identical to plastic strain tensor. Then, the equivalent plastic strain increment may be expressed as

$$\dot{\bar{\epsilon}}^p = \sqrt{\frac{2}{3}\dot{\mathbf{e}}^p : \dot{\mathbf{e}}^p}, \tag{2.6}$$

while the instantaneous equivalent plastic strain is defined as

$$\bar{\epsilon}^{pl} = \sqrt{\frac{2}{3}\mathbf{e}^p : \mathbf{e}^p}. \tag{2.7}$$

No matter how trivial it seems, it is important not to confuse the cumulative equivalent plastic strain (Equation 2.6) with instantaneous quantity in Equation 2.7. The equivalent plastic strain used further in cumulative fashion is used within the damage accumulation. This is used not only in ductile fracture problems, but also similarly in fatigue [134, 148].

Besides the hydrostatic pressure, the mean stress is also useful and used in description of the stress state. Using $\sigma_1 \geq \sigma_2 \geq \sigma_3$ as principal stresses, it is defined as

$$\sigma_m = -p = \frac{I_1}{3} = \frac{\sigma_1 + \sigma_2 + \sigma_3}{3}. \tag{2.8}$$

Von Mises equivalent stress [8] may be used to describe the yield criterion. It takes the following form

$$\bar{\sigma} = \sqrt{3J_2} = \sqrt{\frac{3}{2}\mathbf{S} : \mathbf{S}}. \tag{2.9}$$

In the following text, it is suitable to introduce dimensionless pressure dependence parameter such as the stress triaxiality. The stress triaxiality ranging $-\infty \leq \eta \leq \infty$ is

$$\eta = \frac{\sigma_m}{\bar{\sigma}} = \frac{I_1}{3\sqrt{3J_2}}. \tag{2.10}$$

Deviatoric stress state, often called *the Lode dependence*, may be expressed by more variables as described further. Lode parameter [13] is defined as follows

$$\mu = \frac{2\sigma_2 - \sigma_1 - \sigma_3}{\sigma_1 - \sigma_3}, \tag{2.11}$$

with range $-1 \leq \mu \leq 1$. Lode parameter characterizes position of the second principal stress σ_2 in relation to the first and third principal stresses, σ_1 and σ_3, respectively. Note that $\mu = -1$ when $\sigma_1 > \sigma_2 = \sigma_3$, $\mu = 0$ when $\sigma_2 = (\sigma_1 + \sigma_3)/2$ and $\mu = 1$ when $\sigma_1 = \sigma_2 > \sigma_3$.

The normalized third invariant of deviatoric stress tensor may be used as another variable for describing the deviatoric stress state as

$$\xi = \frac{27}{2}\frac{J_3}{\bar{\sigma}^3} = \frac{\sqrt{27}}{2}\frac{J_3}{J_2^{\frac{3}{2}}}, \tag{2.12}$$

ranging $-1 \leq \xi \leq 1$. The condition of plane stress uniquely gives [111]

$$\xi = -\frac{27}{2}\eta\left(\eta^2 - \frac{1}{3}\right). \tag{2.13}$$

Various angles may be used for the description of Lode dependence. Lode angle and azimuth angle with ranges $0 \leq \theta_L \leq \pi/3$ and $-\pi/6 \leq \theta_A \leq \pi/6$, respectively, are

$$\theta_L = \frac{1}{3}\arccos(\xi) \qquad \text{and} \qquad \theta_A = -\frac{1}{3}\arcsin(\xi) = \arctan\left(\frac{\mu}{\sqrt{3}}\right). \tag{2.14}$$

Finally, the normalized Lode angle is the one of widely used variables in describing the Lode dependence. Depending on other given deviatoric stress state parameters, it can be written as

$$\bar{\theta} = 1 - \frac{6}{\pi}\theta_L = -\frac{6}{\pi}\theta_A = 1 - \frac{2}{\pi}\arccos(\xi) = -\frac{6}{\pi}\arctan\left(\frac{\mu}{\sqrt{3}}\right), \tag{2.15}$$

and it lies in the range $-1 \leq \bar{\theta} \leq 1$.

2.2 Geometrical representation of the stress state

The most conventional way of how to geometrically represent the stress state is to use the Cartesian coordinate system of principal stresses $(\sigma_1, \sigma_2, \sigma_3)$, the so-called Haigh–Westergaard space. This space might be identically interpreted in cylindrical coordinate system (r, θ_L, q) with r as the radius and q as the hydrostatic axis where the principal stresses are equal. Furthermore, the transformation to spherical coordinate system (r, φ, θ_L) may be established. These three coordinate systems are depicted in Figure 2.1a.

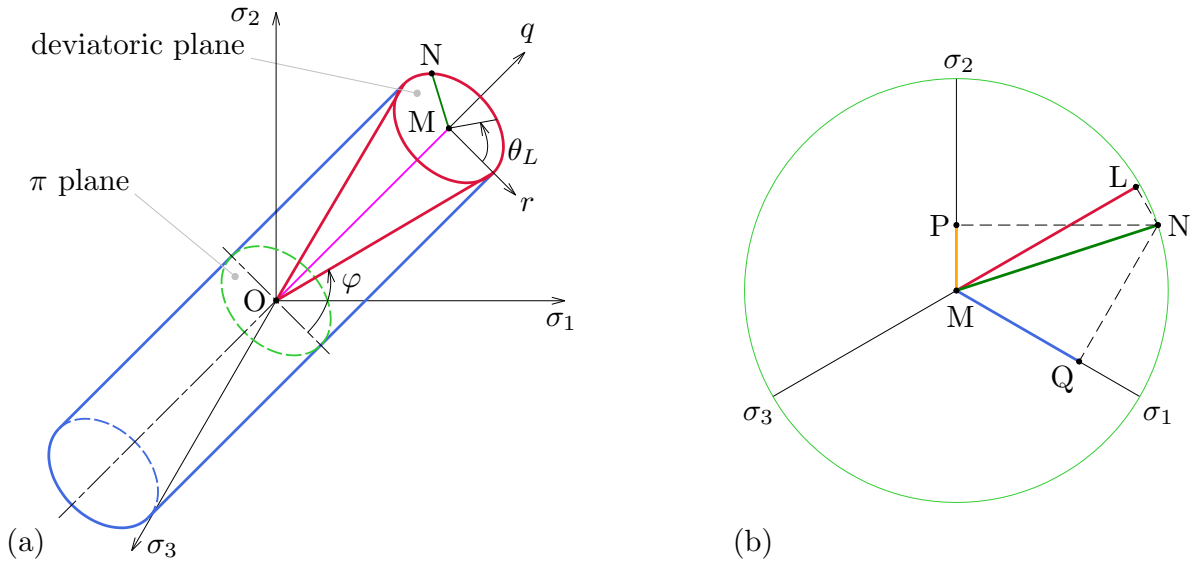

Figure 2.1: Stresses: (a) in Haigh–Westergaard space; (b) on deviatoric plane [120].

The elevation angle in the spherical coordinate system is defined as

$$\varphi = \operatorname{arccotan}\left(\frac{3}{\sqrt{2}}\eta\right). \tag{2.16}$$

General stress vector $\overrightarrow{\mathrm{ON}}$ in the Cartesian coordinate system can be decomposed into two vectors. In vector $\overrightarrow{\mathrm{OM}}$ perpendicular to deviatoric plane, which regards the hydrostatic part, as

$$\|\overrightarrow{\mathrm{OM}}\| = \frac{\sqrt{3}}{3} I_1 = \sqrt{3}\sigma_m, \tag{2.17}$$

and vector $\overrightarrow{\mathrm{MN}}$ in the deviatoric plane regarding the deviatoric part, which reads

$$\|\overrightarrow{\mathrm{MN}}\| = \sqrt{2J_2} = \sqrt{\frac{2}{3}}\bar{\sigma}. \tag{2.18}$$

Additionally, vectors after the projection onto the deviatoric plane are depicted in Fig. 2.1b. These may be expressed by using deviatoric stresses as

$$\|\overrightarrow{\mathrm{MQ}}\| = \sqrt{\frac{3}{2}}S_1, \qquad \|\overrightarrow{\mathrm{MP}}\| = \sqrt{\frac{3}{2}}S_2 \qquad \text{and} \qquad \|\overrightarrow{\mathrm{ML}}\| = \sqrt{\frac{3}{2}}S_3. \tag{2.19}$$

Geometrical representation of both Lode and azimuth angles is depicted in Figure 2.2 on a deviatoric plane, also referred as an octahedral plane, or π plane when containing an origin of Haigh–Westergaard space [156, 163, 168].

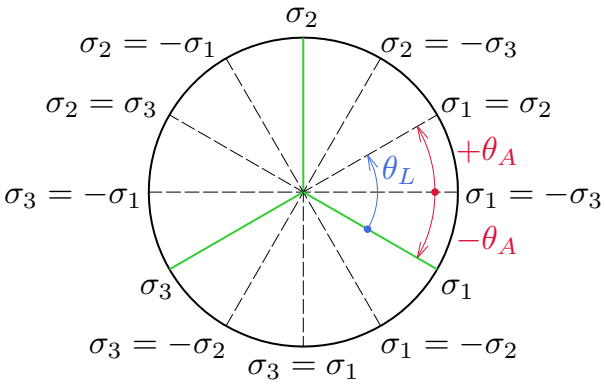

Figure 2.2: Azimuth and Lode angle on the deviatoric plane [120].

Here follows the summary of relations between described deviatoric stress state variables in basic loading conditions. Note that $\xi = \bar{\theta} = 1$, $\mu = -1$, $\theta_A = -\pi/6$ and $\theta_L = 0$ for axisymmetric tension, $\xi = \bar{\theta} = -1$, $\mu = 1$, $\theta_A = \pi/6$ and $\theta_L = \pi/3$ for axisymmetric compression, $\xi = \bar{\theta} = \mu = \theta_A = 0$ and $\theta_L = \pi/6$ for plane strain or generalized shear.

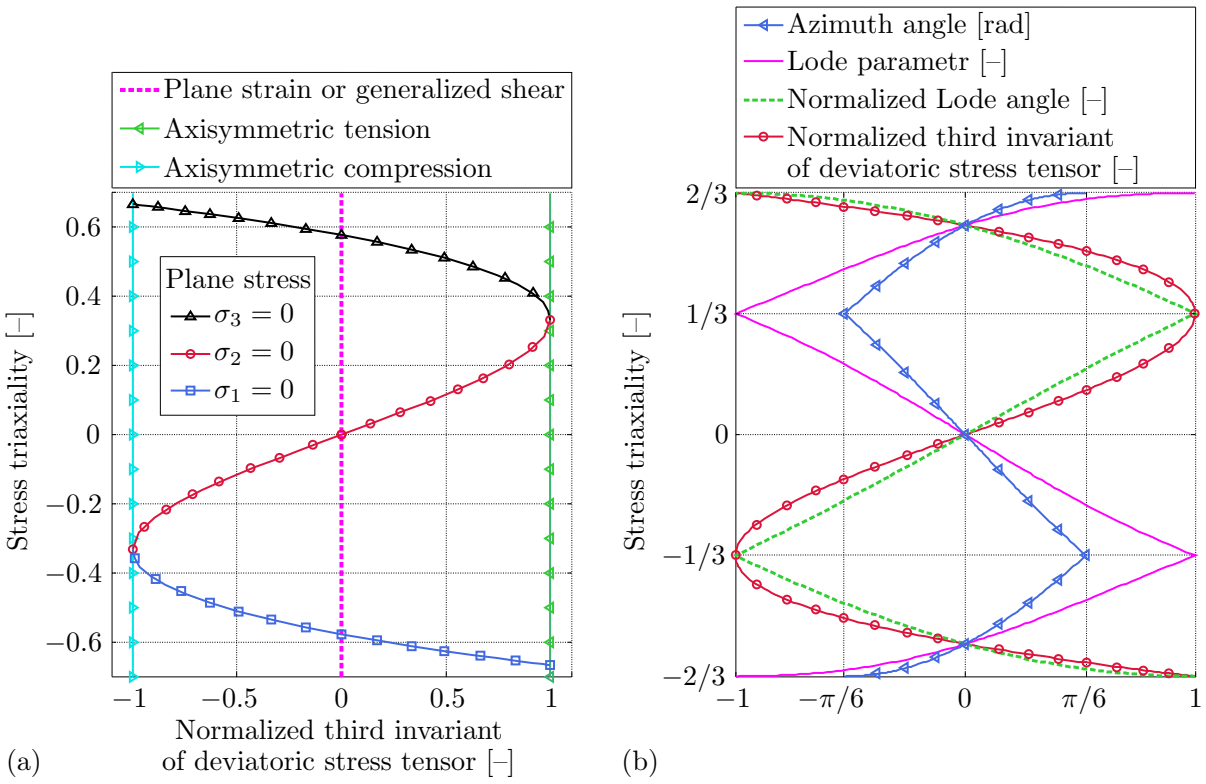

Figure 2.3: The stress triaxiality dependence: (a) on the normalized third invariant of deviatoric stress tensor; (b) on various deviatoric stress state variables [212].

It may be also suitable to illustrate the stress states on the plane of stress triaxiality and certain deviatoric stress state parameter. In the Figure 2.3a, there are depicted various loading conditions on the plane of stress triaxiality and the normalized third invariant of deviatoric stress tensor. There is a geometrical interpretation of relationship between the stress triaxiality and various deviatoric stress state variables in the Figure 2.3b.

2.3 Loading path proportionality

The loading path is also an important issue in scope of ductile fracture. The radial loading is one of the premises in case of ductile fracture criteria. Therefore, the averages of state variables from calibration fracture tests are used.

Radial loading path is derived from a constant slope in the plane of mean and equivalent stresses, respectively, corresponding to constant stress triaxiality. Such path extends radially from the origin (Fig. 2.4a) and the stress tensor components are increased proportionally with monotonically increasing loading variable along it. So radial loading is also known as *proportional loading*. In cases where the loading paths do not have constant slopes over the entire loading history, these are nonradial or nonproportional (Fig. 2.4b) [185].

The loading path deviates from proportional, even in the case of smooth cylindrical specimen beyond the ultimate tensile strength [154]. The problem significantly arises in the case of universal specimens. Those are specimens reaching different stress states by changing the loading conditions, such as the so-called butterfly specimen (Figure 2.5a) inspired by the one designed by Arcan et al. [52]. This specimen – intended for biaxial loading – is probably one of the most problematic, not only from the nonproportionality point of view, but also from the complexity of geometry manufacturing. Various geometries such as with double curvature [113, 128, 213] or just with a flat domain [125, 169] were proposed.

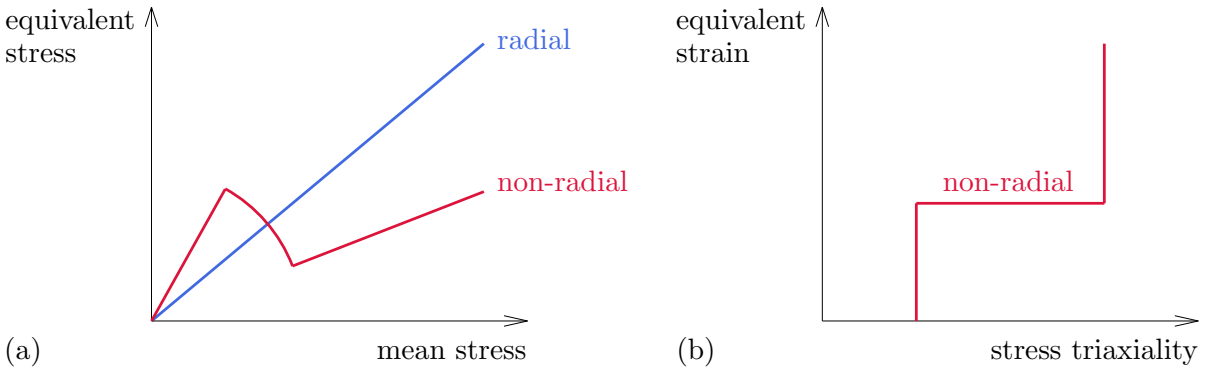

Figure 2.4: Plane of: (a) mean and equivalent stresses with radial and nonradial loading paths; (b) stress triaxiality and equivalent strain with nonradial path [185].

Another noteworthy universal specimen is a tubular one (Figure 2.5b) inspired by the specimen designed by Lindholm et al. [55] for torsional loading. It may have either geometry similar to the original one [145, 160, 173] or double notched tubular geometry [121, 122]. These may be tested under the combination of tension and torsion. The compression and torsion loading combination has been rare and it was incorporated in following works [174, 183].

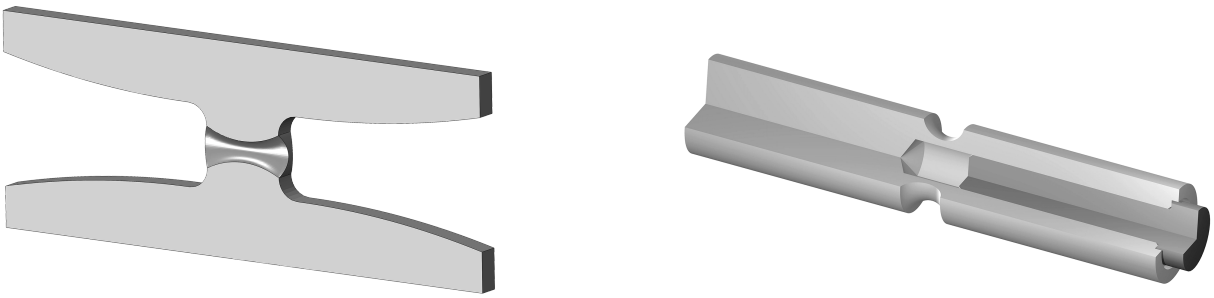

(a) (b)

Figure 2.5: Specimen having geometry of a: (a) butterfly; (b) notched tube [242].

It was also reported that problems arise when there is a high strain concentration [213]. Therefore, such geometries as compact tension or three-point bending specimens were avoided in designing the experimental program.

Nonproportionality in scope of loading paths might lead to discrepancies in calibrating the models and considerable differences between computations and reality represented by experiments. Therefore, emphasis was put to design and keep loading paths of calibration fracture tests as proportional as possible. A final calibrated fracture model may be used for complex nonproportional loading paths, but there are still some issues to be solved.

3 Mechanisms of ductile fracture

Physics of ductile crack formation is discussed in this chapter. It has been studied that the pressure dependence is the key to the crack formation. This dependence was studied, among others, by Bridgman [35], Oyane [46], Hancock and Mackenzie [49], Hancock and Brown [63] and later by Bao [115]. The dependence of the fracture strain on the stress triaxiality is depicted in Figure 3.1 with four highlighted stress triaxiality regions.

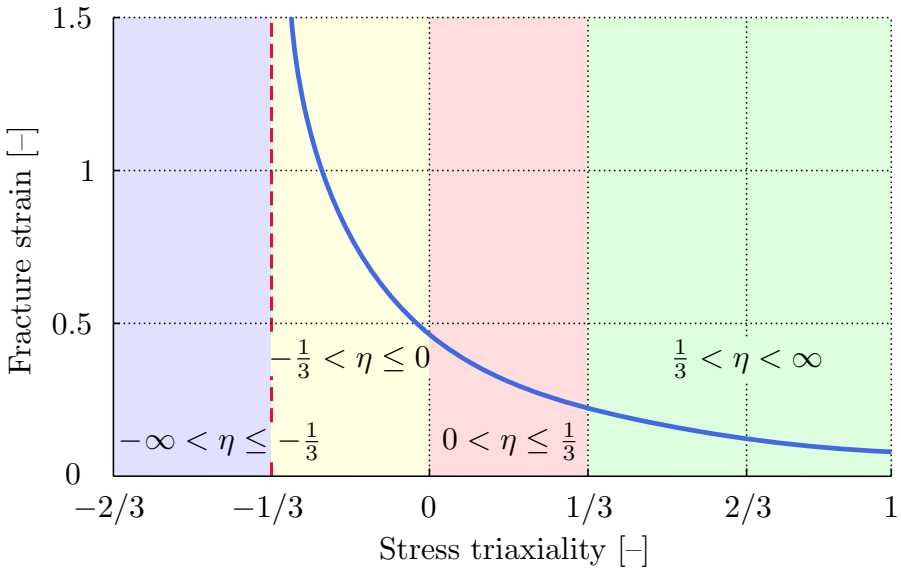

Figure 3.1: Fracture strain dependence on the stress triaxiality [68, 197].

Clausing [42] later found out that the ductility is also substantially reduced when the stress state is changed from axisymmetric tension to plane strain. Wilkins [54] developed model covering the pressure dependence as well as deviatoric stress dependence, which accounts for fracture strain decreasing as the shear load increases. Since the Xue–Wierzbicki model [111] had been developed, it was assumed that the deviatoric stress state plays a vital role in ductile fracture together with hydrostatic pressure. Possible mechanisms of ductile fracture in accordance to the stress triaxiality are simply described in the following paragraphs.

High stress triaxialities $(1/3 < \eta < \infty)$ is the region where the failure is mainly caused by *the void nucleation, growth and coalescence* (Figure 3.2a). Voids most often nucleate on the boundary of the second phase particles which are generally harder than the base metal. This mechanism might be perfectly observed at notched round bars under tensile loading.

Intermediate stress triaxialities ($0 < \eta \leq 1/3$) exhibit mixture of stated fracture mechanisms.

Low stress triaxialities ($-1/3 < \eta \leq 0$) region is probably the least studied one regarding the crack formation and propagation. Due to upsetting tests, among others, it is assumed that the failure is caused by *the shear mechanism* (Figure 3.2b).

No damage and fracture ($-\infty < \eta \leq -1/3$)[1] region, the so-called cut-off representing a threshold of the stress triaxiality below which the damage and fracture does not occur[2], is based on recent experimental observations [98, 105, 109]. Due to results conducted on the aluminium alloy 2024-T351, the value was estimated as $\eta = -1/3$. Recent results show that this value might goes below that threshold. Khan and Liu [175] conducted the biaxial compression test in the channel fixture developed by Khan et al. [124] on the same alloy where the stress triaxiality decreased from $-1/3$ to -0.495. Tutyshkin et al. [215] obtained the stress triaxialies ranging from $-1/3$ to $-2/3$ in the study of cylindrical specimens of DC01 steel, aluminium–magnesium alloy and pure copper containing artificial voids. Kweon [172] studied the damage at negative stress triaxiality in scope of the mesoscale crystal plasticity based damage model and conducted simulations covering the stress triaxialities from -0.75 to 0 . Therefore, the genuine cut-off value has not been certain yet, moreover, it substantially varies with each material.

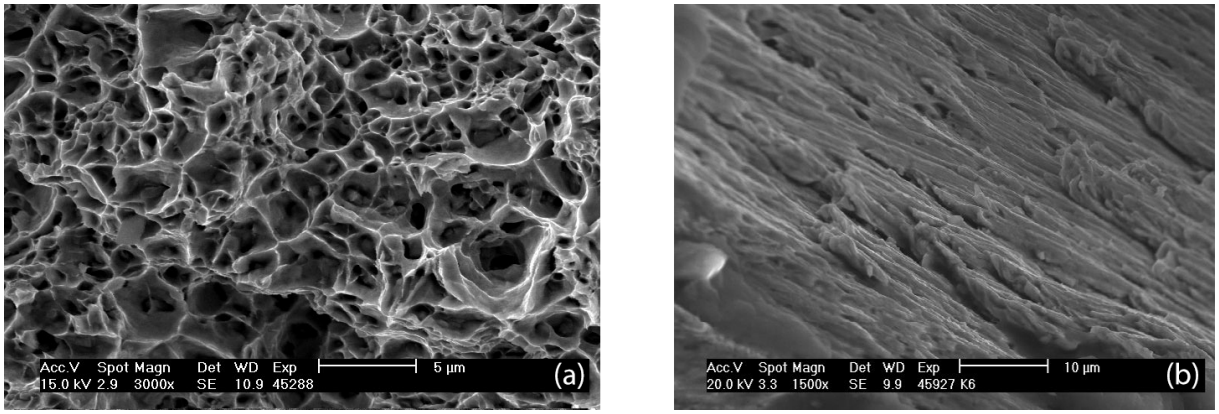

Figure 3.2: Fractographs illustrating two mechanisms of ductile fracture: (a) void nucleation, growth and coalescence; (b) shear mechanism (after Bořkovec [133]).

It should be noted that the major research was focused on the high stress triaxialities in the past. The range of negative stress triaxialities and the cut-off value have been still the subject of extensive investigations.

[1] Based on assumption that the cut-off value lies at $\eta = -1/3$.

[2] There is an analogy to assuming no fracture in case of $-\sigma_1 = -\sigma_2 = -\sigma_3$ in scope of brittle fracture.

4 Overview of existing approaches

Many authors have provided more or less detailed overviews [96, 97, 133, 142, 183], but there is still no uniform attitude yet. Basic approaches may be classified as follows:

- Phenomenological criteria.
- Continuum damage mechanics.
- Void nucleation, growth and coalescence.
- Porosity based models.

Another well known approach is *Forming Limit Diagram* (FLD) [33, 39, 132]. However, it is limited only to sheet metal forming. FLD is defined in the space of major and minor in-plane strains and it is used to predict the onset of necking. The strain-based FLD is strongly loading path dependent. An extension of FLD is *Fracture Forming Limit Diagram* (FFLD) where there are two in-plane strains at the point of fracture [81, 179]. Typical FLD and FFLD are shown in Figure 4.1. Another noteworthy fracture model applicable to thin sheets and extrusions under the plane stress condition is the CrashFEM [99].

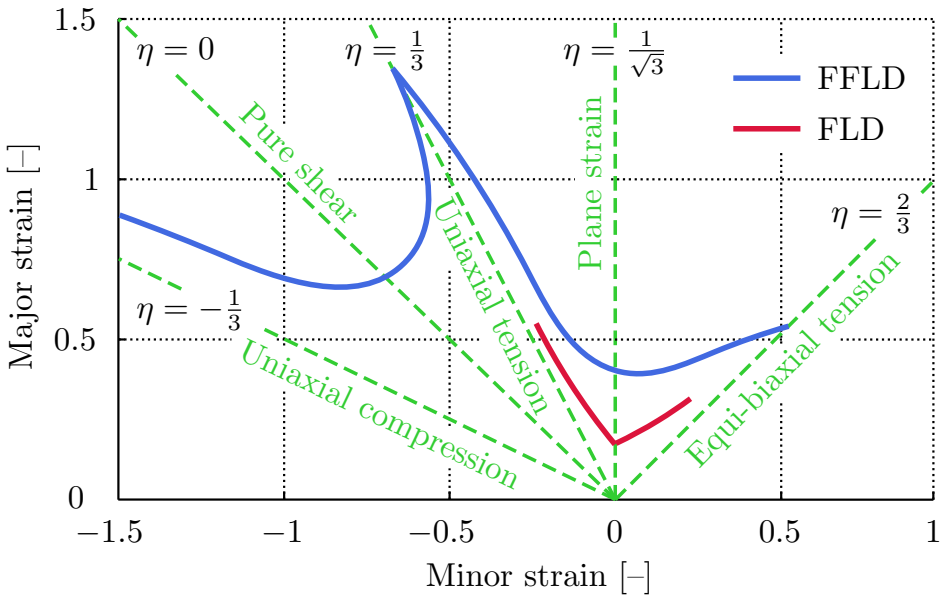

Figure 4.1: FLD and FFLD in the space of major and minor strains [178].

4.1 Phenomenological criteria

In the beginnings, phenomenological criteria were developed by engineers who needed to predict the ductile crack initiation and propagation in bulk or sheet metal forming processes. These macroscopically based criteria were relatively simple and with limited usage in the range of stress states in which they were calibrated.

Freudenthal [20] presented energy criterion defining a limiting amount of the plastic work per unit volume. The expression is integrated until it reaches a critical value which indicates the onset of fracture as

$$\int_0^{\hat{\epsilon}^f} \bar{\sigma}\, \mathrm{d}\bar{\epsilon}^p = C_F, \tag{4.1}$$

where C_F is one material constant and $\hat{\epsilon}^f$ represents the fracture strain for a given loading path.

Cockcroft and Latham [38] proposed that the crack formation is associated with tensile stress even in predominantly compressive processes. The model can be expressed by following expression as

$$\int_0^{\hat{\epsilon}^f} \bar{\sigma} \left\langle \frac{\sigma_1}{\bar{\sigma}} \right\rangle \mathrm{d}\bar{\epsilon}^p = C_{CL}. \tag{4.2}$$

The fraction expresses a non-dimensional stress concentration factor. Variable C_{CL} is one material constant of this model.

Brozzo et al. [44] modified the criterion proposed by Cockcroft and Latham [38] and included the dependence on the mean stress through

$$\int_0^{\hat{\epsilon}^f} \frac{2\sigma_1}{3(\sigma_1 - \sigma_m)}\, \mathrm{d}\bar{\epsilon}^p = C_B, \tag{4.3}$$

where C_B is one material constant.

Oh et al. [53] suggested that it is more reasonable to include just the stress ratio in the model proposed by Cockroft and Latham [38], so the dimensionless model, as in previous case, takes form

$$\int_0^{\hat{\epsilon}^f} \left\langle \frac{\sigma_1}{\bar{\sigma}} \right\rangle \mathrm{d}\bar{\epsilon}^p = C_{MCL}, \tag{4.4}$$

where C_{MCL} is one material constant.

There are multiple other simple criteria containing only one material constant as these listed above. Those are often called empirical models. Further, the focus will be paid to more sophisticated ones where the crack initiation is predicted by the accumulated damage depending on certain weighting function $\bar{\epsilon}^f(\text{state variables})$, apart from the model proposed by Wilkins et al. [54] where the criterion is formulated slightly differently.

Macroscopically, fracture occurs when the damage indicator reaches a critical value, most often unity. Linear incremental relationship between the damage and equivalent plastic strain, when the damage parameter ranges from 0 to 1, may be written as

$$D = \int_0^{\hat{\epsilon}^f} \frac{1}{\bar{\epsilon}^f(\text{state variables})}\, \mathrm{d}\bar{\epsilon}^p. \tag{4.5}$$

Damage $D = 0$ denotes the virgin material without any damage while the material experiences a complete loss of ductility and failures when $D = 1$.

Wilkins et al. [54] pointed out that besides the hydrostatic pressure, the deviatoric stress also enhances the damage. The material fails when the damage D exceeds the critical damage D_c over the critical distance r_c,

$$D = \int_0^{\hat{\epsilon}^f} w_1 w_2 \, \mathrm{d}\bar{\epsilon}^p = D_c, \tag{4.6}$$

where both D_c and r_c are material constants, w_1 is the hydrostatic pressure weighting function and w_2 is the asymmetric strain weighting function, both given as, respectively,

$$w_1 = \left(\frac{1}{1 + pW_1} \right)^{W_2}, \tag{4.7}$$

$$w_2 = (2 - A)^{W_3}, \tag{4.8}$$

where $W_1, \ldots, W_3$ are material constants and A is the parameter denoting the loading asymmetry as

$$A = \max \left(\frac{S_2}{S_3}, \frac{S_2}{S_1} \right), \tag{4.9}$$

where $S_1 \geq S_2 \geq S_3$ are principal stress deviators. Model contains five material constants and does not include the cut-off value.

Johnson and Cook [62] presented the constitutive model considering large strains, high strain rates and high temperatures as

$$\bar{\sigma} = \left(A_{JC} + B_{JC} \left(\bar{\epsilon}^p \right)^n \right) \left(1 + C_{JC} \ln \dot{\bar{\epsilon}}^{p\star} \right) \left(1 - T_h^{D_{JC}} \right), \tag{4.10}$$

where A_{JC}, B_{JC}, C_{JC} and D_{JC} are material constants, $\dot{\bar{\epsilon}}^{p\star}$ is the dimensionless equivalent plastic strain rate, n is the strain hardening exponent and T_h is homologous temperature,

$$\dot{\bar{\epsilon}}^{p\star} = \frac{\dot{\bar{\epsilon}}_p}{\dot{\bar{\epsilon}}^0} \qquad \text{and} \qquad T_h = \frac{T - T_r}{T_m - T_r}, \tag{4.11}$$

$\dot{\bar{\epsilon}}^0$ is the reference strain rate (usually $1.0\,\mathrm{s}^{-1}$), T is the temperature, T_r is the room temperature and T_m is the melting temperature. In Equation 4.10, the term in first bracket describes the strain hardening, terms in second and third brackets represent the effects of strain rate and temperature, respectively. Model contains five material constants.

Later, Johnson and Cook [68] also provided the fracture model involving the strain rate and temperature dependence with following weighting function of damage

$$\bar{\epsilon}^f \left(\eta, \dot{\bar{\epsilon}}^{p\star}, T_h \right) = \left(N_1 + N_2 \mathrm{e}^{N_3 \eta} \right) \left(1 + N_4 \ln \dot{\bar{\epsilon}}^{p\star} \right) \left(1 + N_5 T_h \right), \tag{4.12}$$

where $N_1, \ldots, N_5$ are five material constants. The term in first bracket represents the pressure dependence, terms in second and third brackets have the same meaning as in Equation 4.10 described above. The model does not include the cut-off value.

Bao and Wierzbicki [98, 105] developed new designs of specimens for a wide range of the stress triaxiality ($-1/3 \leq \eta \leq 0.95$) and conducted several tests to study the ductile crack formation. It was found that the fracture locus is more complicated, as in Figure 4.2, and that the approximation cannot be expressed as a monotonic function of the stress triaxiality as in Figure 3.1. Three ranges of stress triaxiality with simple analytical expression for each range were distinguished and the cut-off value at $\eta \leq -1/3$ was assumed. The expressions take form

$$\bar{\epsilon}^f(\eta) = \begin{cases} B_1 \left(\eta + 1/3\right)^{B_2} & \text{if } -1/3 < \eta \leq 0 \\ B_3\eta^2 - B_4\eta + B_5 & \text{if } 0 < \eta \leq 0.4 \\ B_6/\eta & \text{if } 0.4 < \eta \leq \infty \end{cases}, \tag{4.13}$$

where $B_1, \ldots, B_6$ are six material constants. There was also confirmed the importance of the cut-off value presence in scope of high velocity perforations by using this criterion [103, 112, 118].

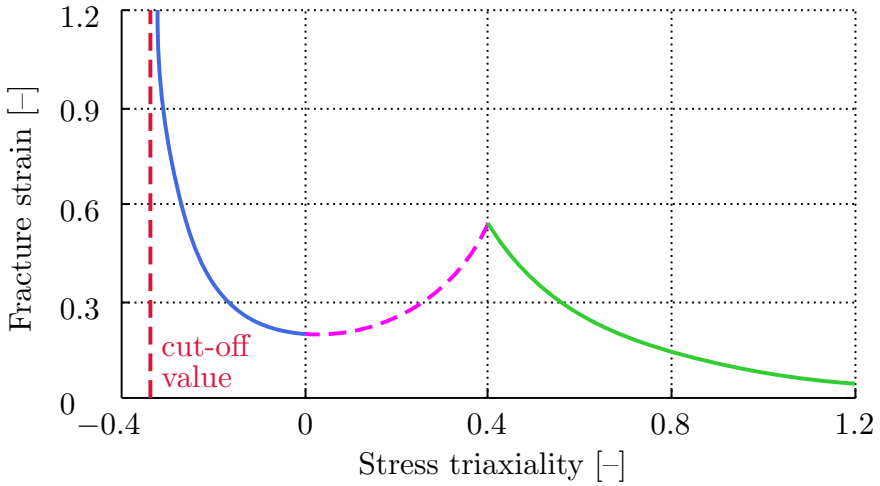

Figure 4.2: Fracture locus in the space of fracture strain and stress triaxiality [101].

The above findings led to the formation of new criteria which concern, apart from the pressure dependence, also the deviatoric stress state dependence. Thus, the equivalent fracture strain is dependent both on the stress triaxiality and on a certain deviatoric stress state parameter. Then, the fracture locus has been most often expressed as an envelope in the space of $(\bar{\epsilon}^f, \eta, \bar{\theta})$ (Figure 4.3b).

In the Figure 4.3, magenta lines denote the plane strain or generalized shear, red lines denote the axisymmetric tension and blue lines denote the axisymmetric compression[3].

[3] Hereinafter, for interpretation of references to colour, the reader is referred to the electronic version of this work.

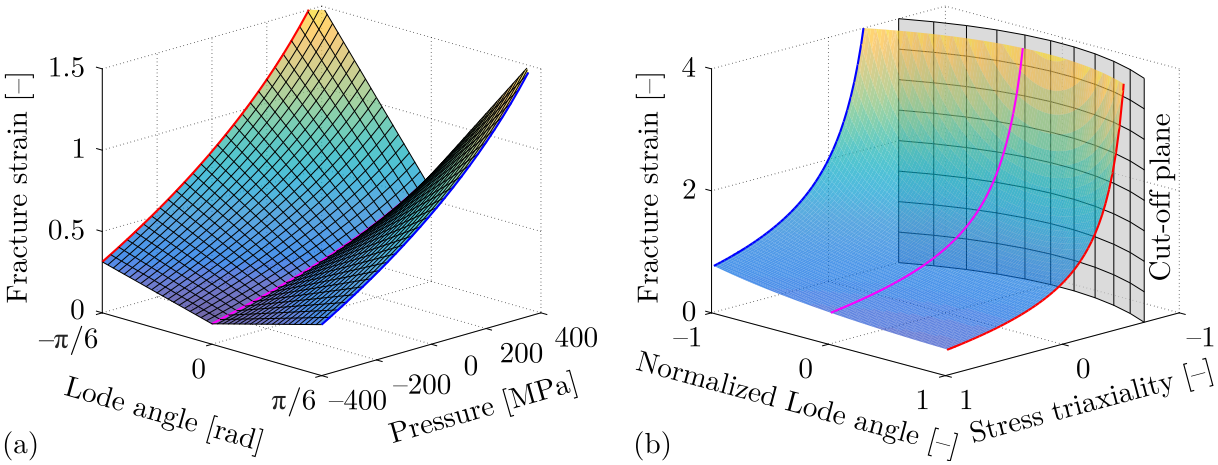

Figure 4.3: Fracture envelope: (a) of model proposed by Xue [120, 126] in the scope of CDM; (b) of its typical shape depicted together with the cut-off plane [233].

The simple criteria in integral form mentioned in the initial part of this section (page 24) may be also expressed in the space mentioned above. The hardening rule has to be chosen first in case of dimensional criteria such as proposed by Freudenthal [20] or Cockcroft and Latham [38]. One of the simplest hardening rules is the one proposed by Hollomon [15]

$$\bar{\sigma} = K\bar{\epsilon}^{n}, \tag{4.14}$$

where K is the strength coefficient and $\bar{\epsilon}$ is total equivalent strain.

Then, the criteria may be transformed from the space of $(\sigma_1, \sigma_2, \sigma_3)$ to $(\bar{\sigma}, \eta, \mu)$ by using following expressions [201]

$$\sigma_1 = \bar{\sigma}\left(\eta + \frac{3-\mu}{3\sqrt{3+\mu^2}}\right), \tag{4.15}$$

$$\sigma_2 = \bar{\sigma}\left(\eta + \frac{2\mu}{3\sqrt{3+\mu^2}}\right), \tag{4.16}$$

$$\sigma_3 = \bar{\sigma}\left(\eta - \frac{3+\mu}{3\sqrt{3+\mu^2}}\right). \tag{4.17}$$

For simplicity, only the nondimensional criteria were transformed using the previous procedure.

In case of model proposed by Oh et al. [53], the weighting function of damage is

$$\bar{\epsilon}^{f}(\eta, \mu) = C_{MCL}\left(\eta + \frac{3-\mu}{3\sqrt{3+\mu^2}}\right)^{-1}. \tag{4.18}$$

It is noteworthy that the criterion is dependent both on the stress triaxiality and Lode parameter in this form and has the cut-off value as well.

Finally, the model proposed by Brozzo et al. [44] takes after transformation the following form

$$\bar{\epsilon}^f(\eta,\mu) = C_B\left(\frac{2}{3} + \frac{2\eta\sqrt{3+\mu^2}}{3-\mu}\right)^{-1}. \tag{4.19}$$

It is also dependent both on the stress triaxiality and Lode parameter and it has got the cut-off value.

Xue–Wierzbicki model [111] concerned the Lode dependence through the normalized third invariant of deviatoric stress tensor. The weighting function of damage, symmetric with respect to the third invariant of deviatoric stress tensor, is expressed as

$$\bar{\epsilon}^f(\eta,\xi) = C_1 e^{-C_2\eta} - \left(C_1 e^{-C_2\eta} - C_3 e^{-C_4\eta}\right)\left(1-|\xi|^{\frac{1}{n}}\right)^n, \tag{4.20}$$

where $C_1,\ldots,C_4$ are four material constants. There is no cut-off plane[4].

Bai and Wierzbicki [135] later postulated the asymmetric fracture envelope, not symmetric with respect to the normalized Lode angle, with following weighting function

$$\begin{aligned}\bar{\epsilon}^f\left(\eta,\bar{\theta}\right) = &\left[\frac{1}{2}\left(D_1 e^{-D_2\eta} + D_5 e^{-D_6\eta}\right) - D_3 e^{-D_4\eta}\right]\bar{\theta}^2 \\ &+ \frac{1}{2}\left(D_1 e^{-D_2\eta} - D_5 e^{-D_6\eta}\right)\bar{\theta} + D_3 e^{-D_4\eta},\end{aligned} \tag{4.21}$$

where $D_1,\ldots,D_6$ are six material constants. Model does not include the cut-off plane.

Extended Mohr–Coulomb criterion [156], based on [1, 6], was expressed through fracture stress at first. Then, it was transformed to strain based space by using the metal plasticity with pressure and Lode dependence [135] and Hollomon hardening law to be

$$\begin{aligned}\bar{\epsilon}^f\left(\eta,\bar{\theta}\right) = &\left\{\frac{K}{E_2}\left[1 - c_\eta\left(\eta-\eta_0\right)\right]\right. \\ &\left[c_\theta^s + \frac{\sqrt{3}}{2-\sqrt{3}}\left(c_\theta^{ax} - c_\theta^s\right)\left\{\sec\left(\frac{\pi}{6}\bar{\theta}\right) - 1\right\}\right] \\ &\left.\left[\sqrt{\frac{1+E_1^2}{3}}\cos\left(\frac{\pi}{6}\bar{\theta}\right) + E_1\left\{\eta + \frac{1}{3}\sin\left(\frac{\pi}{6}\bar{\theta}\right)\right\}\right]\right\}^{-\frac{1}{n}}.\end{aligned} \tag{4.22}$$

Variables E_1 and E_2 are two material constants of the asymmetric fracture envelope which have to be calibrated from fracture tests. Apart from strength coefficient and strain hardening exponent, the rest four constants c_η, c_θ^s, c_θ^{ax} and η_0 are related to plasticity. Model includes the cut-off plane which can be explicitly expressed. If the von Mises yield criterion is adopted, Equation 4.22 can be rewritten into form

$$\bar{\epsilon}^f\left(\eta,\bar{\theta}\right) = \left\{\frac{K}{E_2}\left[\sqrt{\frac{1+E_1^2}{3}}\cos\left(\frac{\pi}{6}\bar{\theta}\right) + E_1\left\{\eta + \frac{1}{3}\sin\left(\frac{\pi}{6}\bar{\theta}\right)\right\}\right]\right\}^{-\frac{1}{n}}. \tag{4.23}$$

[4] There is not particular cut-off value but specific plane because the criteria are no longer two dimensional.

Lou et al. [179] proposed model with dependence on the stress triaxiality and normalized maximum shear stress. Lou and Huh [194] made an extension considering the stress triaxiality and Lode dependence. Later, Lou et al. [212] derived modification considering a changeable cut-off for the stress triaxiality which can be explicitly expressed as well. Weighting function of damage for this asymmetric fracture envelope is in form

$$\bar{\epsilon}^f(\eta,\mu) = L_3 \left(\frac{2}{\sqrt{3+\mu^2}}\right)^{-L_1} \left(\left\langle \frac{1}{1+C_L}\left(\eta + \frac{3-\mu}{3\sqrt{3+\mu^2}} + C_L\right)\right\rangle\right)^{-L_2}, \tag{4.24}$$

where $L_1, \ldots, L_3$ are material constants and parameter C_L represents the sensitivity of the cut-off to the stress triaxiality. So this model has four material constants.

Hosford–Coulomb model [226, 227] is based on Mohr–Coulomb criterion [1, 6] deployed for fracture. Tresca equivalent stress [2] was substituted by the one proposed by Hosford [45], so it was also derived in the stress based form at first. After transformation by using Hollomon hardening law, the asymmetric weighting function of damage reads

$$\bar{\epsilon}^f\left(\eta,\bar{\theta}\right) = \left(\frac{K}{A_2}\left[\left(\frac{1}{2}\left[(f_1-f_2)^{A_1}+(f_2-f_3)^{A_1}+(f_1-f_3)^{A_1}\right]\right)^{\frac{1}{A_1}} + A_3(2\eta+f_1+f_3)\right]\right)^{-\frac{1}{n}}, \tag{4.25}$$

where $A_1, \ldots, A_3$ are three material constants of this cut-off including model and $f_1, \ldots, f_3$ are normalized Lode angle dependent trigonometric functions given as, respectively,

$$f_1 = \frac{2}{3}\cos\left[\frac{\pi}{6}\left(1-\bar{\theta}\right)\right], \tag{4.26}$$

$$f_2 = \frac{2}{3}\cos\left[\frac{\pi}{6}\left(3+\bar{\theta}\right)\right], \tag{4.27}$$

$$f_3 = -\frac{2}{3}\cos\left[\frac{\pi}{6}\left(1+\bar{\theta}\right)\right]. \tag{4.28}$$

4.2 Continuum damage mechanics

CDM is based on the macroscopic observation of solids. In this case, the constitutive model is coupled with the damage and those influence each other. The degradation process and loss of the load carrying area are due to the irreversible process of void nucleation and growth during straining. This approach represents an alternative to the porosity based models in a phenomenological way. Damage models are often called coupled, compared with phenomenological models which are often called uncoupled. It is because in the case of phenomenological criteria, the damage is influenced by the plasticity but not vice versa.

Kachanov [28] laid the foundations of continuum damage mechanics in the context of creep. He assumed the weakening factor $w = 1$ at the initial moment where there is no damage and that $w = 0$ at the moment of rupture. He pointed out that the weakening factor need not to be scalar and presented the following power law

$$\dot{w} = -f(T) \left(\frac{\sigma^\star}{w} \right)^{f(t)}, \tag{4.29}$$

where $f(T)$ and $f(t)$ are possible functions of temperature and time, respectively, $\sigma^\star$ is the highest tensile stress and whole fraction represents the effective stress. If compressive stresses were present, the tensile ones were supposed not to be small compared to them.

Rabotnov [34] also dealt with creep and suggested that the matrix material degrades through damage parameter D_s which is related to the weakening factor through

$$w = 1 - D_s. \tag{4.30}$$

Thus, the parameter $D_s = 0$ when there is no damage and $D_s = 1$ when the material experiences the loss of load carrying area.

In general, the damage parameter corresponding to reduction of load carrying area may not necessary to be the same as the damage indicator describing the reduction of ductility, thus

$$D_s \neq D. \tag{4.31}$$

The equivalent matrix stress σ_M is supposed to be greater than the equivalent stress which satisfies the load–displacement curve obtained from experiment, therefore it can be written as

$$D_s \leq D. \tag{4.32}$$

Xue [120] adopted a material constant β as the weakening exponent, implicating

$$D_s = D^\beta. \tag{4.33}$$

Finally, the requirement from Equation 4.32 is satisfied when $\beta \geq 1$.

Lemaitre [65, 66] developed *the concept of effective stress* with respect to isotropic material. The expression for the effective stress with the use of damage parameter D_s is

$$\tilde{\sigma} = \frac{\sigma}{1 - D_s}. \tag{4.34}$$

This emphasizes that the presence of voids raises the effective stress. *The hypothesis of strain equivalence* was also adopted, so one dimensional linear elasticity involving damage is

$$\tilde{\epsilon}^e = \frac{\tilde{\sigma}}{E} = \frac{\sigma}{E(1 - D_s)}, \tag{4.35}$$

where $\tilde{\epsilon}^e$ is the effective elastic strain and E is Young's modulus. With respect to Ramberg–Osgood constitutive equation [16], the effective plastic strain for the three dimensional case reads

$$\tilde{\epsilon}^p = \left(\frac{\tilde{\sigma}}{K} \right)^{\frac{1}{n}} = \left(\frac{\bar{\sigma}}{K(1 - D_s)} \right)^{\frac{1}{n}}. \tag{4.36}$$

Lemaitre further introduced the damage strain energy release rate, similar to the strain energy release rate or crack driving force in classical fracture mechanics, as follows

$$-Y = \frac{\bar{\sigma}^2}{2E(1-D_s)^2}\left[\frac{2}{3}(1+\nu)+3(1-2\nu)\eta^2\right], \tag{4.37}$$

where ν is the Poisson's ratio. Then, the damage evolution law can be written as

$$\dot{D}_s = \begin{cases} 0 & \text{if } \tilde{\epsilon}^p < \bar{\epsilon}^{th} \\ \frac{1}{1-D_s}\left(\frac{-Y}{S_r}\right)^{s_r}\dot{\tilde{\epsilon}}_p & \text{if } \tilde{\epsilon}^p \geq \bar{\epsilon}^{th} \end{cases}, \tag{4.38}$$

where S_r and s_r are temperature and material dependent terms, respectively, and $\bar{\epsilon}^{th}$ is the damage strain threshold. The fracture occurs when the damage parameter reaches its critical value D_{cr} which is assumed to be another material property. So this model includes four material constants. The stress triaxiality cut-off value was implemented later [166] as well as the influence of deviatoric stress state [217, 220]. Broumand and Khoei [195] found Lemaitre's approach very effective when employed as a non-local together with the use of XFEM.

Chaboche valuably contributed with clear summarization of the main basic features of previous continuum damage mechanics approaches and reviewed some practical damage growth equations [71, 72].

Bonora [84] presented generally nonlinear damage evolution law in the form

$$\mathrm{d}D_s = \alpha\frac{(D_{cr}-D_0)^{\frac{1}{\alpha}}}{\ln\hat{\epsilon}^f - \ln\bar{\epsilon}^{th}}\left[\frac{2}{3}(1+\nu)+3(1-2\nu)\eta^2\right](D_{cr}-D_s)^{\frac{\alpha-1}{\alpha}}\frac{1}{\tilde{\epsilon}^p}\,\mathrm{d}\tilde{\epsilon}^p, \tag{4.39}$$

where variable α is the exponent of damage and D_0 is the initial amount of damage, often taken equal to zero due to its difficult measurability. Model contains five material constants. Later, Bonora and Newaz [89] extended the concept to the low cycle fatigue.

The effect of the initial damage introduced on some surface layers, caused for example by machining process [216] or by blanking process [231], was studied in the scope of uncoupled models with the use of Finite Element Analysis (FEA).

Børvik et al. [94] provided ductile damage model for penetration and impact related problems based on constitutive and fracture models proposed by Johnson and Cook [62, 68] and CDM approach introduced by Lemaitre [66]. This model included the associated flow rule and effects of strain rate and temperature through following expression

$$\bar{\sigma} = (1-D_s)\left(A_B + B_B\left(\tilde{\epsilon}^p\right)^n\right)\left(1+\dot{\tilde{\epsilon}}^{p\star}\right)^{C_B}\left(1-T_h^{D_B}\right), \tag{4.40}$$

where A_B, B_B, C_B and D_B are material constants and $\dot{\tilde{\epsilon}}^{p\star}$ is the dimensionless effective plastic strain rate defined similarly as in original model of Johnson and Cook through

$$\dot{\tilde{\epsilon}}^{p\star} = \frac{\dot{\tilde{\epsilon}}_p}{\dot{\tilde{\epsilon}}^0}. \tag{4.41}$$

This model involves five material constants. Term representing the effect of strain rate in Equation 4.40 is modified with respect to Camacho and Ortiz [83] to avoid unwanted effects when $\dot{\tilde{\epsilon}}^{p\star} < 1$. Considering this modification, the weighting function of damage, which does not concern any stress triaxiality cut-off value, can be written as

$$\bar{\epsilon}^f\left(\eta, \dot{\bar{\epsilon}}_p, T_h\right) = \left(M_1 + M_2 \mathrm{e}^{M_3\eta}\right)\left(1 + \dot{\tilde{\epsilon}}^{p\star}\right)^{M_4}\left(1 + M_5 T_h\right), \tag{4.42}$$

where $M_1, \ldots, M_5$ are material constants. The damage evolution during straining is

$$\dot{D}_s = \begin{cases} 0 & \text{if } \tilde{\epsilon}^p < \bar{\epsilon}^{th} \\ \frac{D_{cr}}{1-D_s}\frac{1}{\bar{\epsilon}^f - \bar{\epsilon}^{th}}\dot{\bar{\epsilon}}_p & \text{if } \tilde{\epsilon}^p \geq \bar{\epsilon}^{th} \end{cases}. \tag{4.43}$$

Fracture occurs as D_s reaches critical damage D_{cr} which is material constant as well, so the model includes seven material constants.

Saanouni has also been distinctly involved in continuum damage mechanics, following Lemaitre's approach, and strongly aimed on practical applicability in metal forming processes as a prediction of chevron cracks in cold extrusion of cylindrical bar, crack propagation in the blanking of thin sheet, or thin sheet deformation after the slitting due to the residual stress [116, 130].

Xue [120, 126] introduced damage plasticity model involving the sensitivity to the hydrostatic pressure and Lode dependence. Material behaviour is defined by hardening function $\sigma_M(\bar{\epsilon}^p)$ following von Mises yield criterion. Then, material deterioration reads

$$\bar{\sigma} = w\sigma_M = (1 - D_s)\sigma_M = (1 - D^\beta)\sigma_M. \tag{4.44}$$

The nonlinear damage evolution is expressed as follows

$$D = \int_0^{\bar{\epsilon}^f} m\left(\frac{\bar{\epsilon}^p}{\bar{\epsilon}^f\left(p, \bar{\theta}\right)}\right)^{m-1} \frac{\mathrm{d}\bar{\epsilon}^p}{\bar{\epsilon}^f\left(p, \bar{\theta}\right)}. \tag{4.45}$$

Finally, the weighting function of damage may be expressed as

$$\bar{\epsilon}^f\left(p, \bar{\theta}\right) = \tilde{\epsilon}^f\left[1 - \hat{q}\ln\left(1 - \frac{p}{p_{lim}}\right)\right]\left[1 + (1 - \hat{\gamma})\left|\bar{\theta}\right|^{\hat{k}}\right], \tag{4.46}$$

where $\tilde{\epsilon}^f$ is the uniaxial tensile fracture strain without confining pressure, $\hat{q}$ is the shape parameter, p_{lim} is the limiting pressure (parameter governing the cut-off), $\hat{\gamma}$ is the fracture strain ratio and $\hat{k}$ is Lode dependence exponent. The model contains seven material constants and the typical shape of fracture envelope is show in Figure 4.3a. The pressure sensitivity, term in the first bracket in Equation 4.46, is based on observations made by Bridgman [35]. Lode dependence, term in the second bracket in Equation 4.46, was derived separately on the work of Wilkins et al. [54].

It shall be noted that there is another approach to ductile fracture combining the phenomenological criteria with continuum damage mechanics. The model is *partially coupled* with plasticity to incorporate *the post-initiation behaviour* [152, 157, 219]. So it is based on the weakening effect, but rather for dealing with the prediction of crack propagation than for the weakening itself, because the slant fracture is usually not computationally predicted by models without incorporating the material weakening [190].

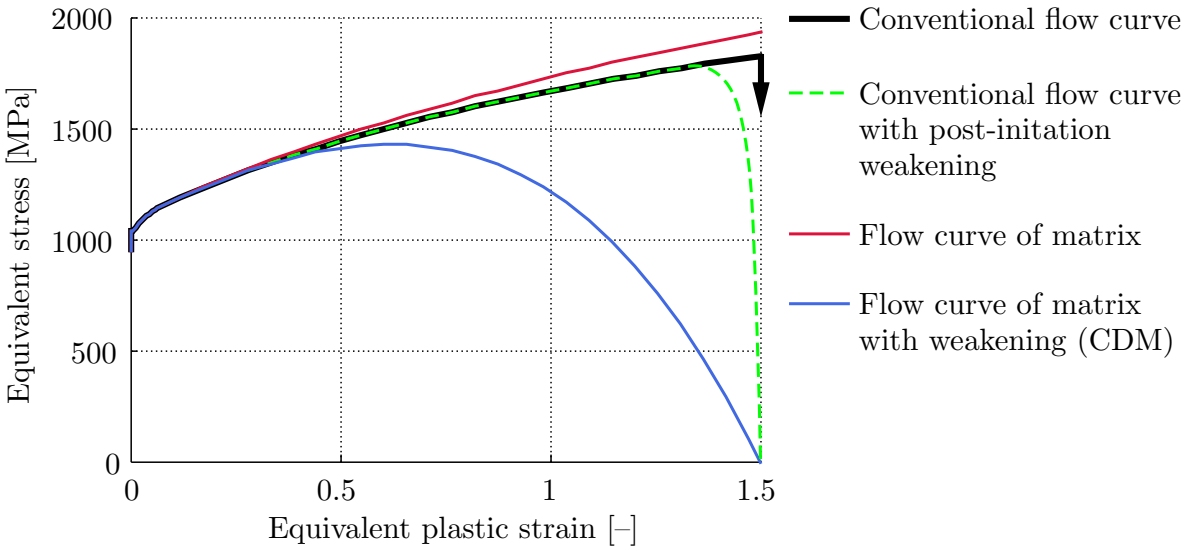

Figure 4.4: Stress–strain curves for different approaches to ductile fracture.

The problem of crack propagation is caused by finite element size. Generally, the smaller the length of the element, the easier the crack propagation in slant fracture fashion is triggered. In case of phenomenological criteria, the most affected elements, where there is accumulated a critical amount of damage, are deleted. It causes instantaneous formation of a free surface and drop in force–displacement response. In fact, it should take some time for the crack to propagate throughout the elements length. This is incorporated using weakening after crack initiation.

The element can gradually lose its strength (see Figure 4.4) through

$$\bar{\sigma} = \begin{cases} \bar{\sigma} & \text{if } D \leq D_p \\ \bar{\sigma} \left(\frac{D_{cr} - D}{D_{cr} - D_p} \right)^{\bar{m}} & \text{if } D_p < D < D_{cr} \\ 0 & \text{if } D = D_{cr} \end{cases}, \tag{4.47}$$

where D_p is damage parameter at the moment of crack initiation within an element and $\bar{m}$ is a weakening parameter. These, together with critical damage D_{cr} in the moment of element deletion, are additional material constants to arbitrary phenomenological ductile fracture model and introduce the post-initiation weakening [152].

4.3 Void nucleation, growth and coalescence

Theoretical research of the void nucleation, growth and coalescence (Figure 4.5) has been mostly performed on the Representative Volume Element (RVE) containing the void. Such microscopic approach was then used for studying macroscopic behaviour of the complex material containing voids, second phase particles and inclusions.

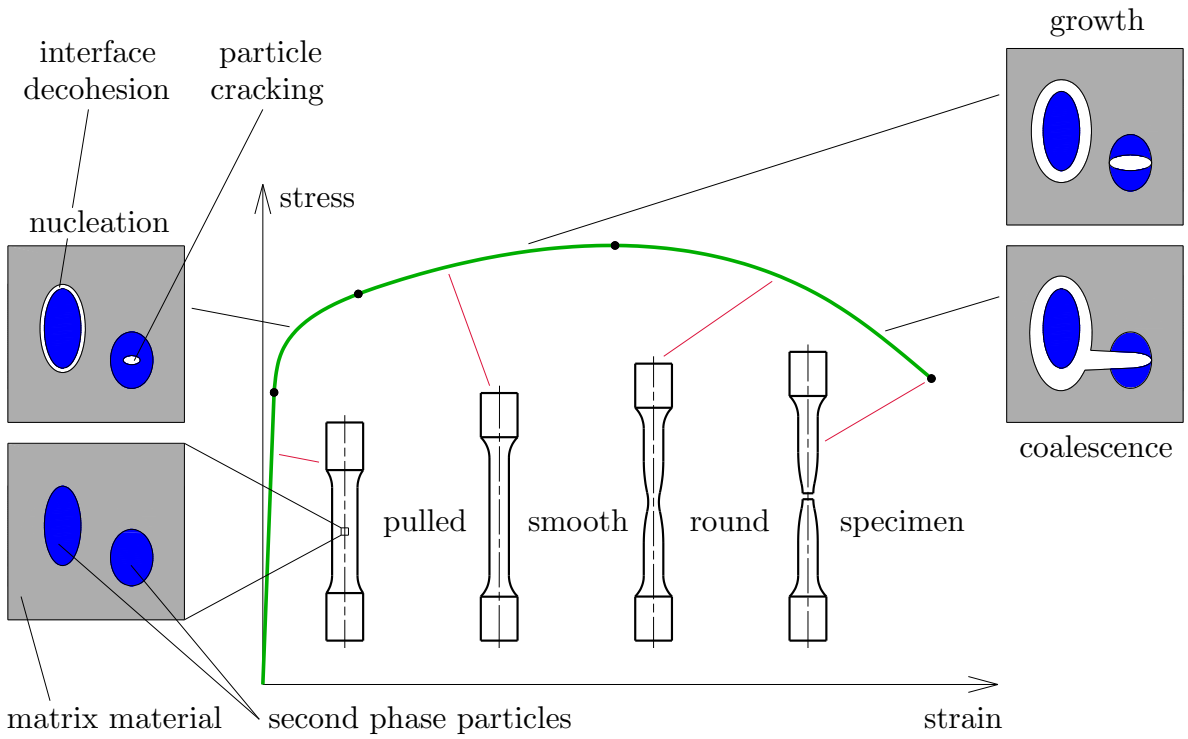

Figure 4.5: Void nucleation, growth and coalescence during the tension [123].

McClintock [40] assumed the material to contain sets of cylindrical holes of elliptical cross-section. Major and minor directions of the applied stresses were parallel with their axes. The damage accumulated to unity at fracture through following expression

$$D = \int_0^{\bar{\epsilon}^f} \frac{1}{\ln F_f} \left[\frac{\sqrt{3}}{2(1-n)} \sinh\left(\frac{\sqrt{3}(1-n)}{2} \frac{\sigma_a + \sigma_b}{\bar{\sigma}} \right) + \frac{3}{4} \frac{\sigma_a - \sigma_b}{\bar{\sigma}} \right] \mathrm{d}\bar{\epsilon}^p, \tag{4.48}$$

where F_f is a relative hole growth factor and the only one material constant of this model. Variables σ_a and σ_b denote applied stresses in major and minor directions, respectively. The model has a cut-off value when transformed into the space of $(\bar{\epsilon}^f, \eta, \bar{\theta})$ [228].

Rice and Tracey [41] studied the growth of a spherical void and suggested criterion, which does not include the cut-off value, for a simple tensile remote field as

$$\int_0^{\bar{\epsilon}^f} 0.283 \mathrm{e}^{\frac{\sqrt{3}}{2}\eta} \, \mathrm{d}\bar{\epsilon}^p = C_{RT}, \tag{4.49}$$

where C_{RT} is one material constant.

Le Roy et al. [58] followed up on the work of Rice and Tracey [41] and developed it further, allowing the change of void shape. However, these efforts were rather theoretical.

RTCL [97] is a criterion combining model proposed by Rice and Tracey [41] for high stress triaxialities and model proposed by Cockcroft and Latham [38] for intermediate and low stress triaxialities. The damage, also involving the cut-off value at $\eta = -1/3$, reads

$$D = \begin{cases} 0 & \text{if } \eta \leq -1/3 \\ \int_0^{\hat{\epsilon}^f} 2\frac{1+\eta\sqrt{12-27\eta^2}}{3\eta+\sqrt{12-27\eta^2}}\,\mathrm{d}\bar{\epsilon}^p & \text{if } -1/3 < \eta < 1/3\,. \\ \int_0^{\hat{\epsilon}^f} \frac{1}{1.65}\mathrm{e}^{\frac{3}{2}\eta}\,\mathrm{d}\bar{\epsilon}^p & \text{if } \eta \geq 1/3 \end{cases} \tag{4.50}$$

The fracture occurs when the damage reaches its critical value D_{RTCL} which is one material constant of this model. Here, the model proposed by Rice and Tracey was a modified version derived by Fischer et al. [78]. The model proposed by Cockcroft and Latham given here was derived with the use of von Mises yield criterion, assuming the plane stress state in a certain plane and with neglecting certain shear stress components [97]. The classification of RTCL as void nucleation, growth and coalescence model is questionable when the model proposed by Cockcroft and Latham was assumed to be phenomenological.

4.4 Porosity based models

Porosity based models differ from those mentioned above. These stand on similar theoretical background as previous microscopic approach, but do not accumulate the damage separately from yielding. Instead, it is assumed that the material is porous containing isolated spherical or cylindrical voids at microscopic level and the influence of such voids is incorporated in constitutive framework, instantly affecting the plastic flow. Then, the porosity serves as such a failure indication.

Gurson [47, 48, 50] laid foundations of the widespread porosity based model and assumed idealized matrix as a perfectly rigid plastic material obeying the von Mises yield criterion. The approximate upper bound yield function for volumetrically symmetric deformations around a single spherical void (see Figure 4.6) can be written as

$$\Phi = \left(\frac{\bar{\sigma}}{\sigma_M}\right)^2 + 2f_G \cosh\left(\frac{3}{2}\frac{\sigma_m}{\sigma_M}\right) - f_G^2 - 1, \tag{4.51}$$

where f_G is the void volume fraction. The yield function takes a form of von Mises yield criterion when $f_G = 0$.

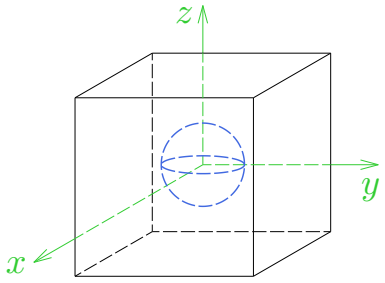

Figure 4.6: RVE with a spherical void [207].

Tvergaard and Needleman [57, 60, 64] provided well-known modification of the model proposed by Gurson [47, 48, 50], the so-called GTN model, due to predicting the complete loss of material load carrying capacity at unrealistic level. Then, the approximate yield function can be rewritten as

$$\Phi = \left(\frac{\bar{\sigma}}{\sigma_M}\right)^2 + 2q_{GTN}f^\star \cosh\left(\frac{3}{2}\frac{\sigma_m}{\sigma_M}\right) - \left(q_{GTN}f^\star\right)^2 - 1, \tag{4.52}$$

where q_{GTN} is a material constant and $f^\star$ is void volume function defined as

$$f^\star = \begin{cases} f_G & \text{if } f_G \leq f_c \\ f_c + \frac{q_{GTN}^{-1} - f_c}{f_F - f_c}\left(f_G - f_c\right) & \text{if } f_G > f_c \end{cases}, \tag{4.53}$$

where f_c is the critical value of void volume fraction and f_F is the void volume fraction at fracture. For $f^\star = f_G$ and $q_{GTN} = 1$ the criterion degenerates to form that was proposed by Gurson [47, 48, 50] (Equation 4.51).

Previous modification was followed by many others and Gurson-like model has been of interest to many researches [77, 161, 222]. The original GTN model was derived for volumetrically symmetric deformations and it was shown that Lode dependence needs to be introduced to improve the predictive capability and accuracy in shear dominant loading conditions [139, 207, 225].

5 Experiments

5.1 Aluminium alloy 2024-T351

All experiments were conducted on AA 2024-T351. This Al–Cu–Mg alloy, which was solution heat treated, stress-relieved stretched and then cold worked, has face-centred cubic structure [144] and is widely used in aviation and aerospace engineering, among others, for various components because of its high strength to weight ratio and good fatigue resistance. It has negligible strain rate sensitivity up to $5000\,\mathrm{s}^{-1}$ [203]. It is commonly extruded or forged. On the contrary, the welding and soldering are not recommended. This alloy is also widely used by researches to examine ductile fracture behaviour [98, 175] as well as fatigue [150]. The chemical composition of the particular supplied alloy is given in Table 5.1. It was obtained by glow discharge optical emission spectroscopy on Spectrumat GDS 750. The results are averages from three measurings.

Table 5.1: Chemical composition of AA 2024-T351.

Element	Si	Fe	Cu	Mn	Mg	Cr	Zn	Ti	Ni
Volume [Weight %]	0.07	0.25	4.3	0.52	1.71	0.00	0.01	0.04	0.00

The material was supplied as a cold rolled plate of metal with dimensions $1500 \times 1000 \times 20\,\mathrm{mm}$ (Figure 5.1). Then it was cut into 5 pieces ($300 \times 1000 \times 20\,\mathrm{mm}$) along the shorter side by water jet cutting to facilitate handling and specimen manufacturing. The aforementioned cutting method was used to prevent the formation of heat affected zones.

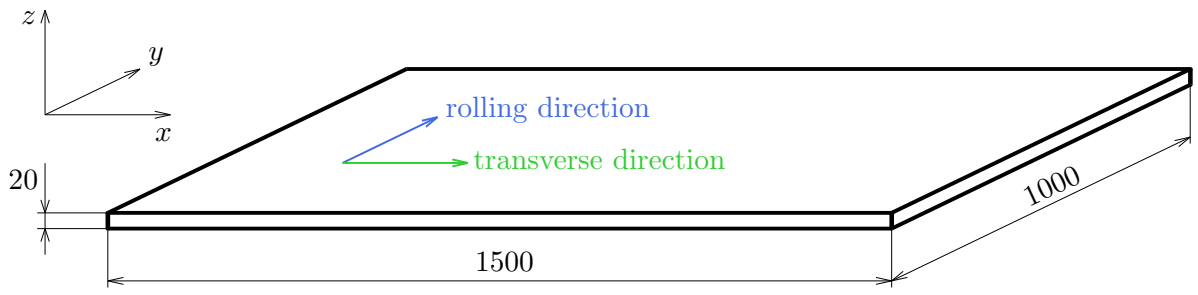

Figure 5.1: Detailed drawing of supplied plate of aluminium alloy 2024-T351.

Specimens, taken in two transverse directions x and y, respectively, were polished and etched for metallographic analysis. The rolling[5] and transverse directions, depicted in Figure 5.1, were estimated from the size and orientation of grains shown in Figure 5.2.

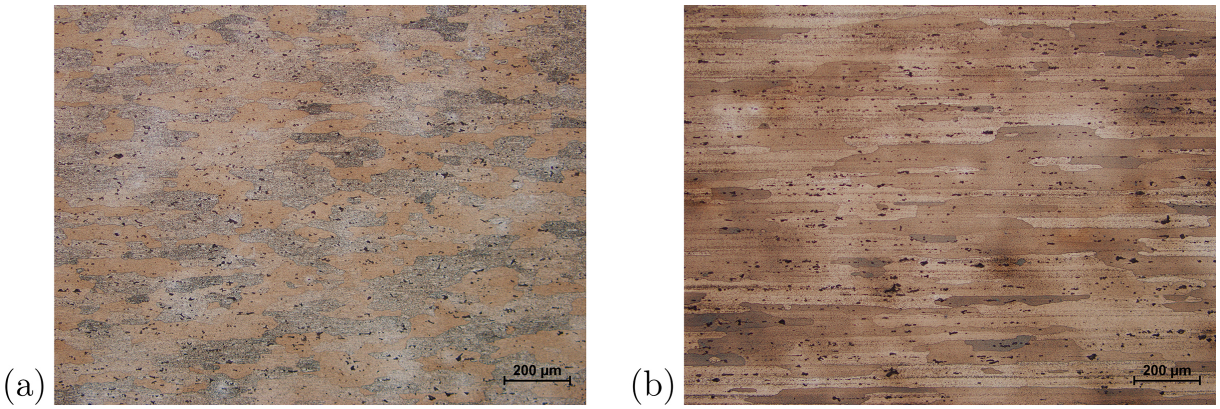

Figure 5.2: Micrograph of cross-section along: (a) x direction; (b) y direction.

Among others, the rolling direction was studied by fractography using scanning electron microscope, Tescan LYRA3 XMH equipped by Oxford Instruments with Energy Dispersive X-ray Spectroscopy (EDS) analyser, through secondary and backscattered electrons. Transcrystalline ductile fracture, or the so-called dimpled rupture, governed mostly by the void nucleation and growth was observed. There was also brittle fracture of present intermetallic particles. There was significant banding of intermetallic particles for post-mortem specimen from the rolling direction (Figure 5.3).

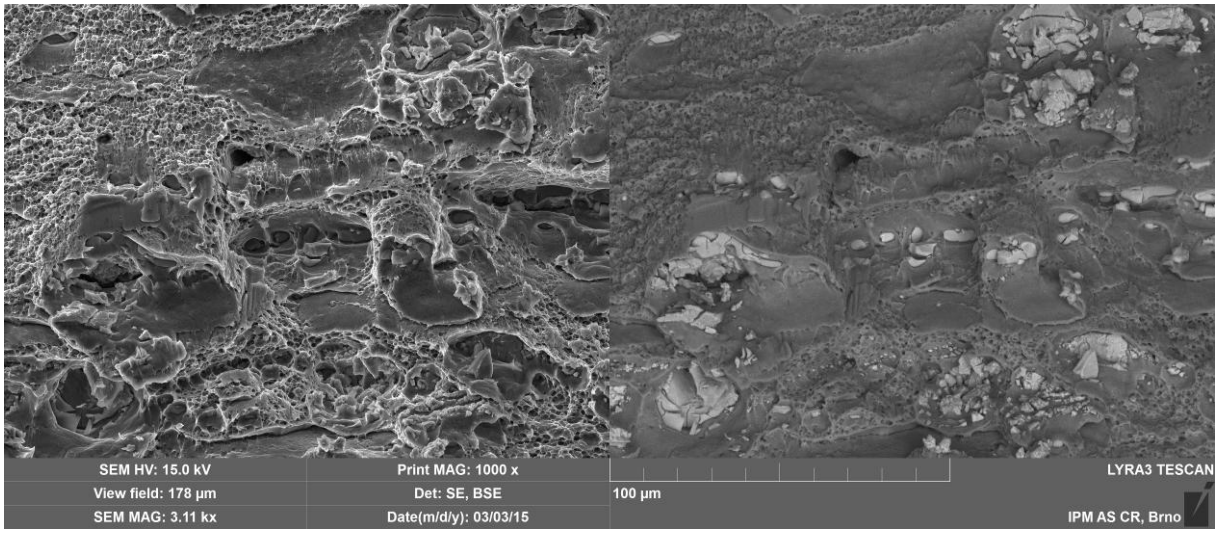

Figure 5.3: Fractograph from the rolling direction.

[5] Also called longitudinal direction in the present study.

Only one moderate banding of intermetallic particles was observed, in the case of x direction, as depicted in Figure 5.4, which is consistent with assumption that this is the direction transverse to rolling.

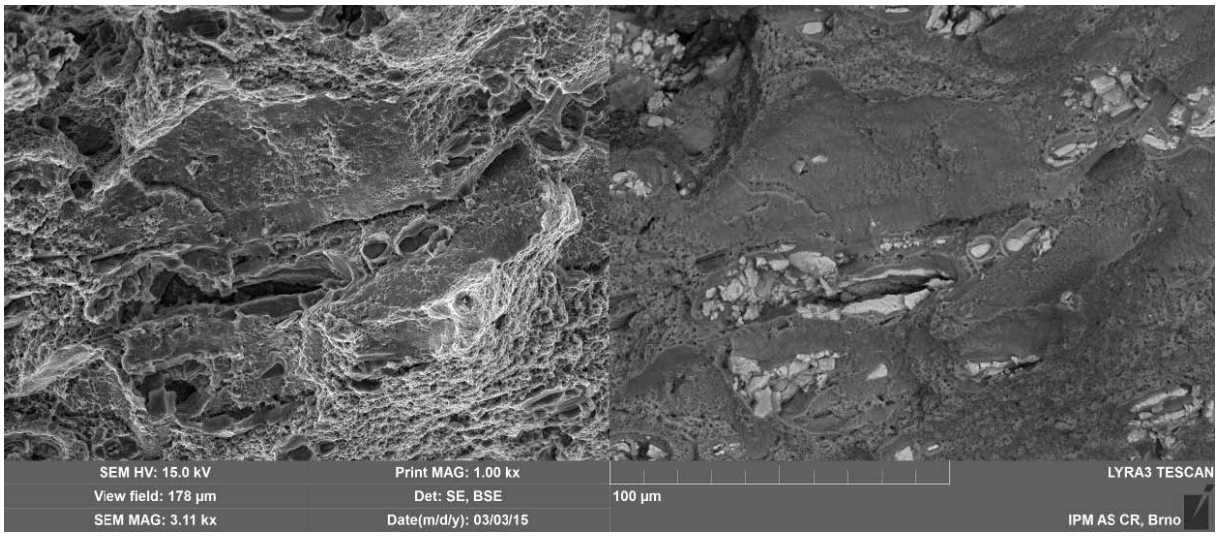

Figure 5.4: Fractograph from the transverse direction.

There was also notable omni-directional particle cracking in case of fracture surface from transverse direction (Figure 5.5).

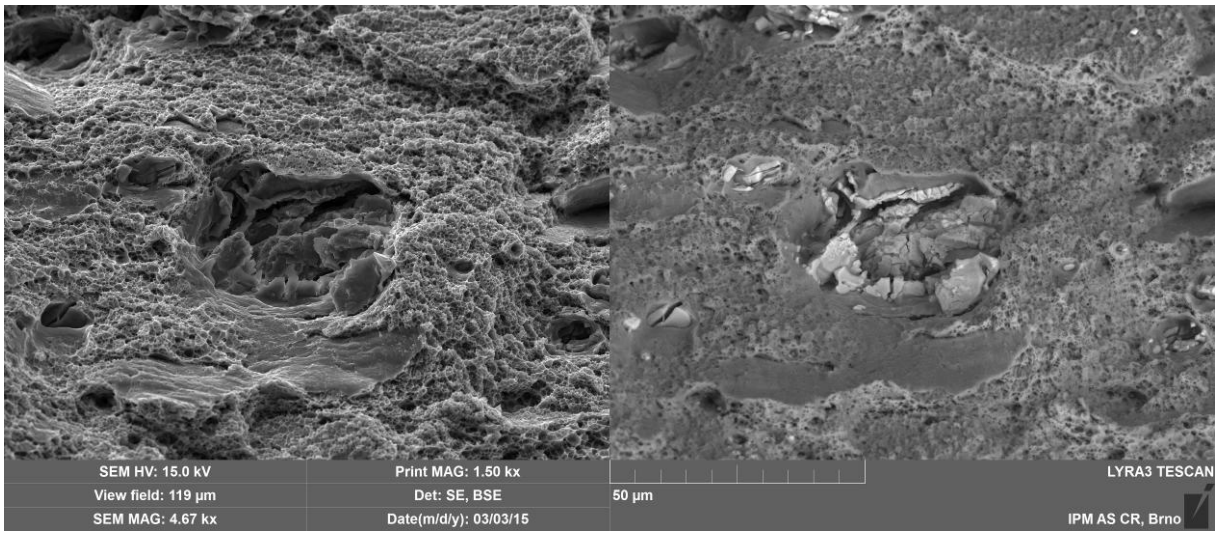

Figure 5.5: Fractograph from x direction depicting omni-directional cracked particle.

There was probable presence of following intermetallic phases in microstructure, Al_2Cu, Al_2CuMg, Al_7Cu_2Fe, $Al_4Cu_2Mg_8Si_7$, AlCuFeMnSi and Mg_2Si, which is consistent with elements found by chemical microanalysis using EDS (Figure 5.6).

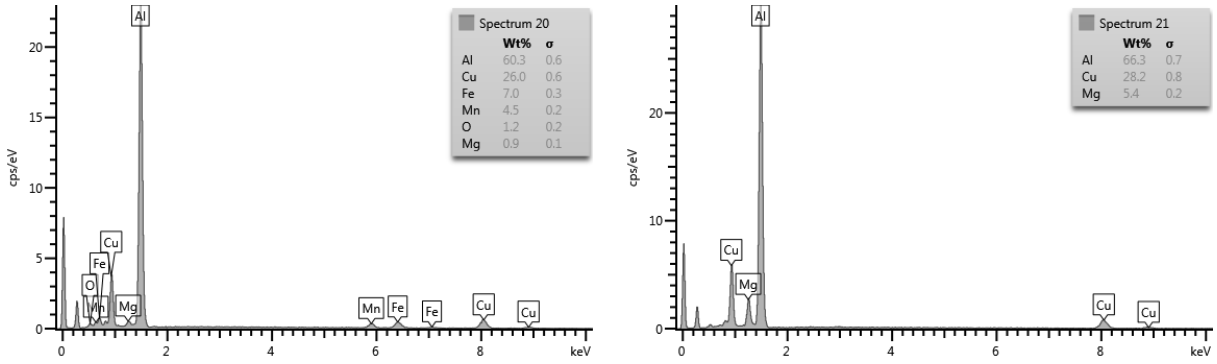

Figure 5.6: EDS analysis results for two different spectra.

5.2 Experimental program

In order to obtain *the flow curve* for description of material plastic flow, as well as to calibrate *the fracture model*, there was an experimental program designed and carefully carried out at a room temperature. There are schematic drawings of chosen specimens with their basic dimensions in Figure 5.7 and Table 5.2 where there is an outline of the designed experimental program.

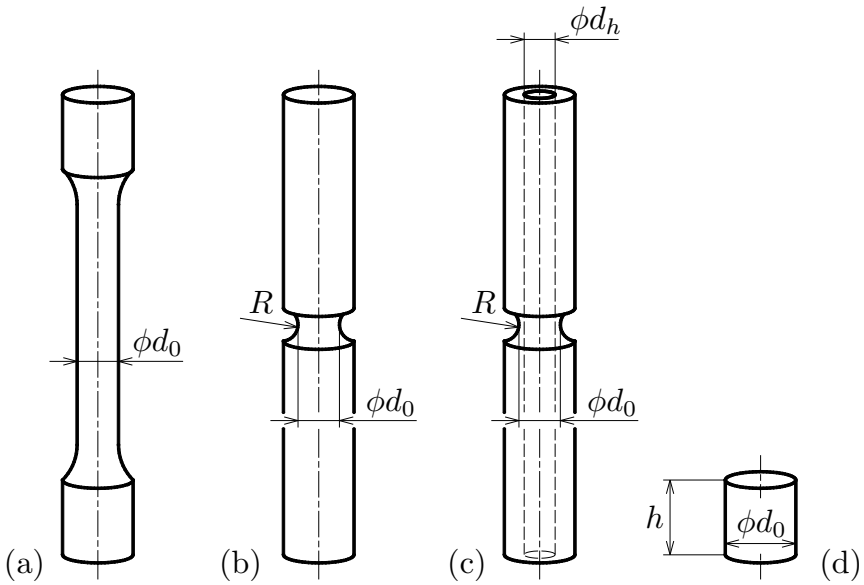

Figure 5.7: Schematic drawings of specimen types used in experimental program: (a) smooth cylindrical; (b) notched cylindrical; (c) notched tubular; (d) cylindrical.

Theoretical values of the initial stress triaxiality for specimens loaded in tension in Table 5.2 were calculated by using Equation 5.4 derived in the following paragraphs.

While σ_z is the axial stress, R is the neck radius and d is the actual diameter of the round bar (Figure 5.8a), Bridgman [35] derived for post-necking phase that

$$\frac{\sigma_z}{\bar{\sigma}} = 1 + \ln\left(\frac{\left(\frac{d}{2}\right)^2 + dR - r^2}{dR}\right). \tag{5.1}$$

When the stress distribution in the minimum cross-sectional area of the neck is axially symmetric, von Mises yield criterion gives [94]

$$\eta = \frac{\sigma_z}{\bar{\sigma}} - \frac{2}{3}. \tag{5.2}$$

If the Equation 5.2 is inserted into the Equation 5.1, and R and d_0 are assumed as the notch radius and the initial diameter in the notch (Figure 5.8b), respectively, the initial stress triaxiality of notched cylindrical specimen on the axis, where there is a maximum value when $r = 0$, is

$$\eta = \frac{1}{3} + \ln\left(1 + \frac{d_0}{4R}\right). \tag{5.3}$$

Later, the formula was modified for aluminium alloy by using the FEA into form [98]

$$\eta = \frac{1}{3} + \sqrt{2}\ln\left(1 + \frac{d_0}{4R}\right). \tag{5.4}$$

Table 5.2: Designed experimental program.

Test	Radial loading condition	Specimen type	Initial stress triaxiality [–]	Normalized Lode angle [–]
1		Figure 5.7a, $d_0 = 6\,\text{mm}$	1/3	1
2		Figure 5.7b, $d_0 = 9\,\text{mm}$, R13	0.559	1
3	Tension	Figure 5.7b, $d_0 = 9\,\text{mm}$, R6.5	0.754	1
4		Figure 5.7b, $d_0 = 9\,\text{mm}$, R4	0.965	1
5		Figure 5.7c, $d_0 = 9\,\text{mm}$, R4, $d_h = 7\,\text{mm}$	$\sqrt{3}/3$	0
6	Torsion	Figure 5.7b, $d_0 = 9\,\text{mm}$, R4, $d_h = 8\,\text{mm}$	0	0
7	Compression	Figure 5.7e, $d_0 = 8\,\text{mm}$, $h = 12\,\text{mm}$	$-1/3$	-1

There are depicted theoretical positions of the fracture tests in the space of the stress triaxiality and normalized third invariant of deviatoric stress tensor in the Figure 5.9. The geometry of the notched cylindrical specimen with the shallowest notch radius was designed in order to have approximately the same stress triaxiality as the tensile loaded notched tube. The remaining two notched cylindrical specimens with sharper notch radii were designed in order to keep approximately the same interval to each other with respect to stress triaxiality.

There were also realized experiments on flat plate specimen loaded in tension. Unfortunately, these were not included in the calibration because of problems with dramatic changing of normalized Lode angle arising with the use of Lode dependent plasticity (Chapter 9). The whole issue is described in Appendix A.

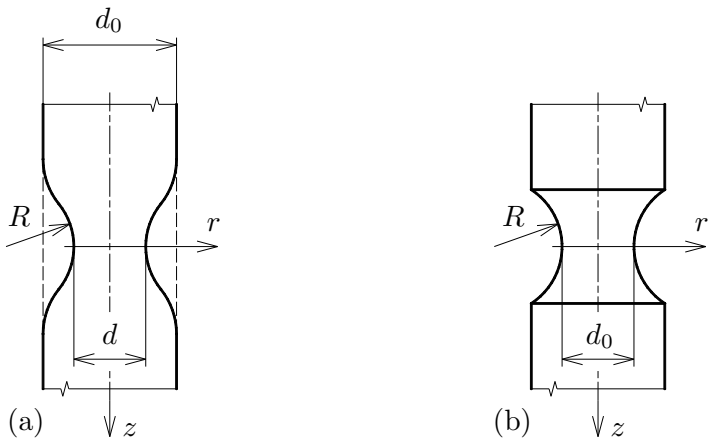

Figure 5.8: Dimensions related to: (a) the necking of smooth cylindrical specimen under tension in z axis; (b) the notched cylindrical specimen under tension in z axis.

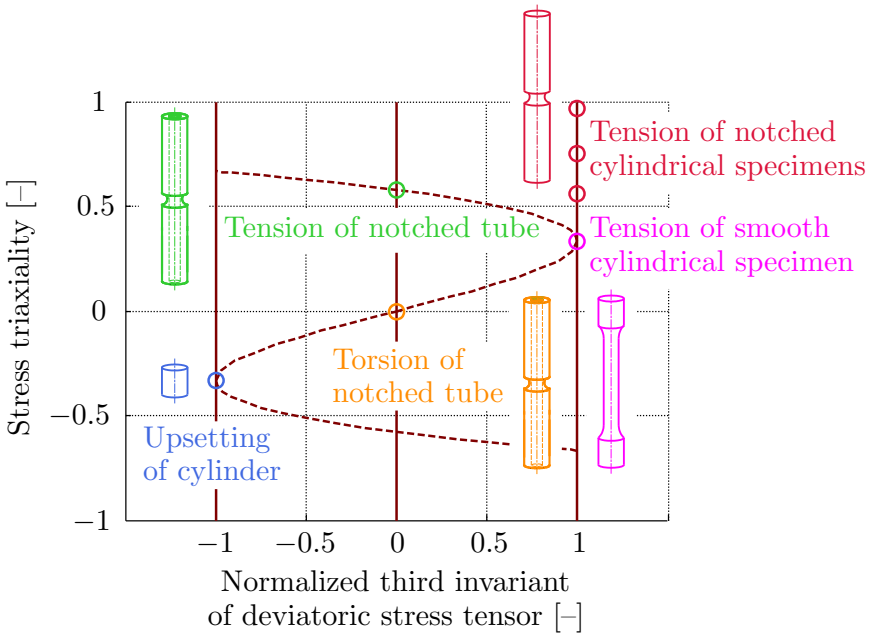

Figure 5.9: Theoretical positions of the fracture tests in the plane of stress states.

5.3 Tensile tests of smooth cylindrical specimens with discussion on anisotropy

AA 2024-T351 has been assumed as isotropic by many researches [98, 105, 175] as well as anisotropic [104, 203]. In order to study the degree of anisotropy, there were conducted 5 tensile tests of smooth cylindrical specimens (Figure 5.10[6]) both in rolling and transverse directions and then the average force–displacement curves were determined (Figure 5.11).

[6] Where no roughness is prescribed, the value Ra 3.2 is taken in the present study.

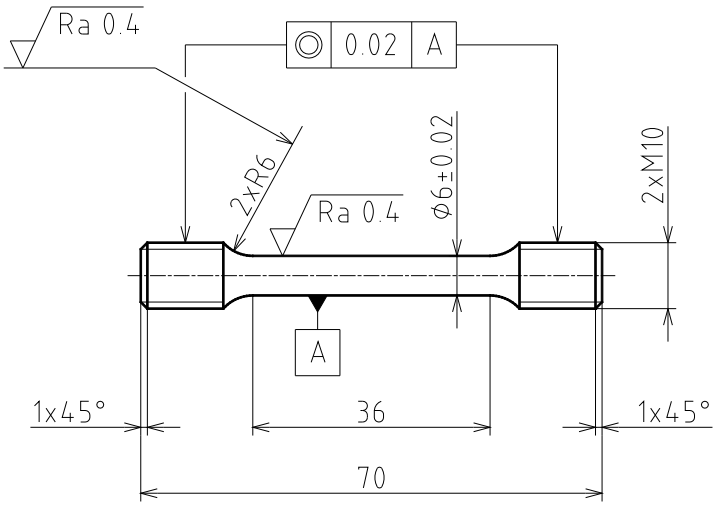

Figure 5.10: Detailed drawing of the smooth cylindrical specimen with 6 mm diameter.

Testing machine Zwick Z250 Allround-Line, tCII, and extensometer Zwick multiXtens were used for tensile testing under displacement control. To ensure the quasi-static loading, the test speed was 1 mm/min until the yield point when it was smoothly transferred to 2 mm/min. The gauge length was 30 mm.

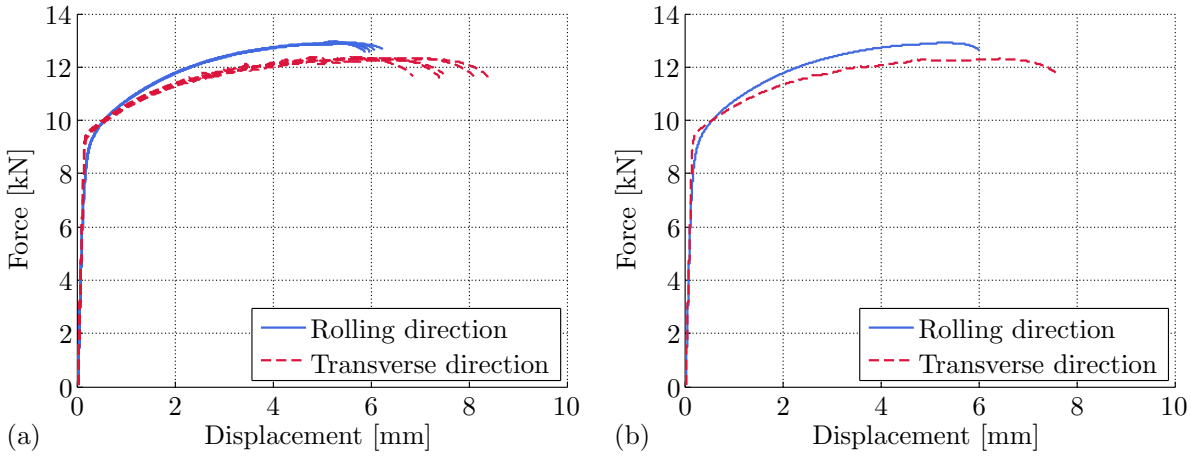

Figure 5.11: Force–displacement: (a) curves for 5 tensile tests both in the rolling and transverse directions; (b) curves averaged in the rolling and transverse directions.

There is a higher ultimate strength in the y direction (Figure 5.11) which corresponds to results from metallographic analysis and proves that y is really the rolling direction, although there is a higher yield stress and ductility in transverse direction. Nevertheless, this material behaviour corresponds to the one obtained by Bao in compression [98].

There are post-mortem smooth cylindrical specimens from rolling and transverse directions shown in Figures 5.12 and 5.13, respectively.

Finally, we assumed the material to be isotropic due to obtained results. The anisotropy was involved neither by means of the plasticity [203] nor the fracture [137, 237] in the present study as well as by means of no directional distortional hardening [95, 129].

Figure 5.12: Post-mortem 6 mm diameter round bars from the rolling direction.

Figure 5.13: Post-mortem 6 mm diameter round bars from the transverse direction.

It should be noted that the Portevin–LeChatelier effect [11] was also apparent in the transverse direction. The serrations are depicted for two chosen parts of force–displacement responses in Figure 5.14. This effect was not accounted for further.

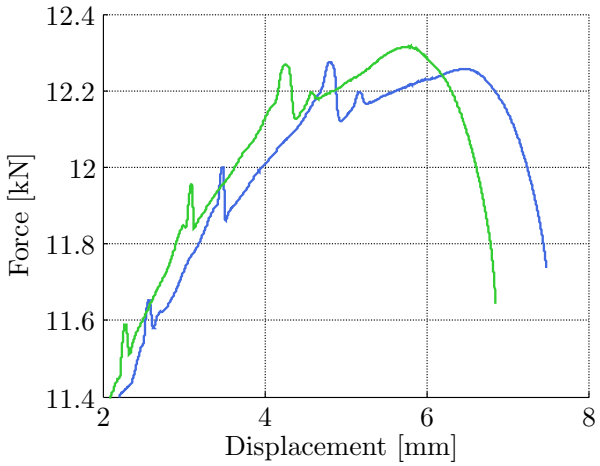

Figure 5.14: Portevin–LeChatelier effect in the transverse direction.

5.4 Discussion on the crack formation in tensile tests

Xue [120] pointed out that there were different mechanisms of ductile fracture in tensile tests of smooth cylindrical specimens with 6, 9 and 15 mm diameters. In case of 6 mm diameter, there was observed a classic dimpled (cup and cone) fracture. There was a slant fracture in case of 9 mm diameter and finally, there was a mixed slant and cup and cone mode in case of 15 mm diameter.

Here, the slant fracture was observed on smooth cylindrical specimens in rolling direction (Figure 5.15a) in tensile testing and cup and cone or coexisting fracture mechanisms in transverse direction (Figures 5.15b and 5.15c).

(a) (b) (c)

Figure 5.15: Fracture surface of cylindrical specimen from the: (a) rolling direction (slant); (b) transverse direction (coexisting mode); (c) transverse direction (dimpled).

Moreover, additional tensile tests were carried out on 3 smooth cylindrical specimens with 10 mm diameter in rolling direction (Figure 5.16) under the same conditions as in the previous section. There was a slant fracture observed (Figure 5.17) as in the case of smaller diameter of smooth specimens in rolling direction. Therefore, the size effect is not an option. More likely, the crack formation in tensile tests is dependent on the longitudinal or transverse directions so as the Portevin–LeChatelier effect.

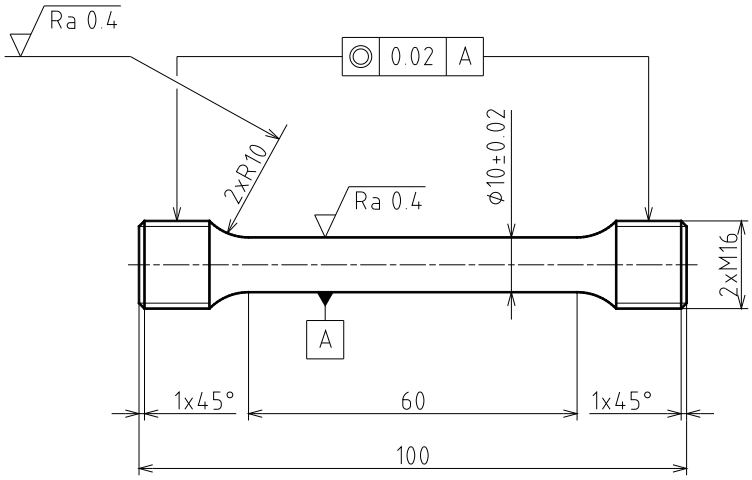

Figure 5.16: Detailed drawing of the smooth round specimen with 10 mm diameter.

Figure 5.17: Post-mortem 10 mm diameter round specimens from the rolling direction.

Olympus LEXT OLS3100 confocal laser scanning microscope was used in order to find the angle of fracture surface to applied loading, in the case of specimen from longitudinal direction. Reconstructed fracture surface revealed that it was approximately 45° (Figure 5.18), in the plane of maximum shear stress.

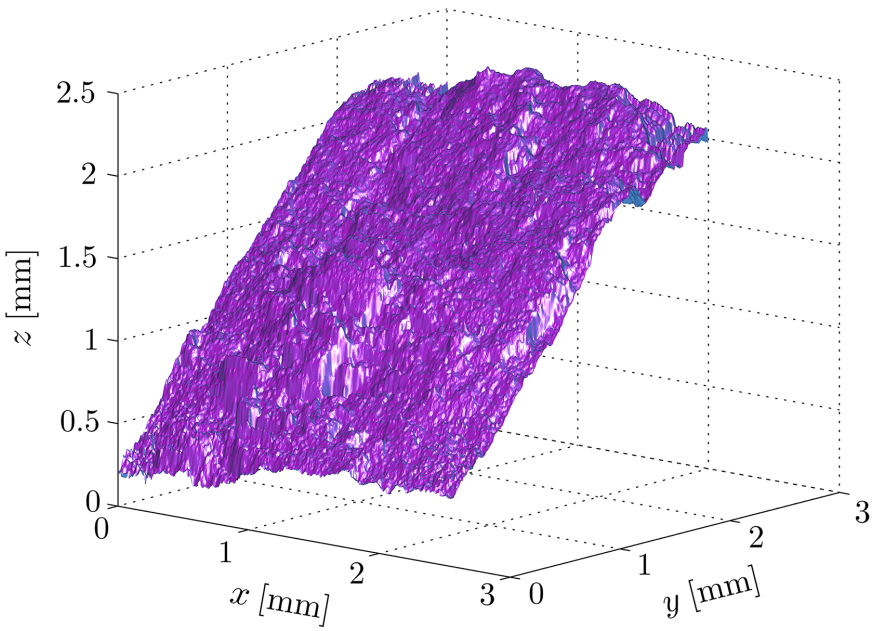

Figure 5.18: Reconstructed fracture surface for specimen from the rolling direction.

The presented problem of crack formation might be related to motion of dislocations on the slip plane as well. Nevertheless, it will not be further developed in this study. Hereinafter, all experiments will be done within the rolling (longitudinal) direction.

5.5 Tensile tests of notched cylindrical specimens

Tensile tests of notched cylindrical specimens were carried out to map the pressure dependence in the case of axisymmetric tension. Three various geometries were used, with three specimens for each geometry, from the shallow notch to the sharpest one. These 3 specimens had the same dimensions, the same diameter in the minimum cross-sectional area of the notch, except for the notch radius (Figure 5.19). Again, testing machine Zwick Z250 Allround-Line, tCII, and extensometer Zwick multiXtens were used for tensile testing under the displacement control. The test speed was 1 mm/min during whole test to ensure the quasi-static loading. The gauge length was 30 mm in all cases.

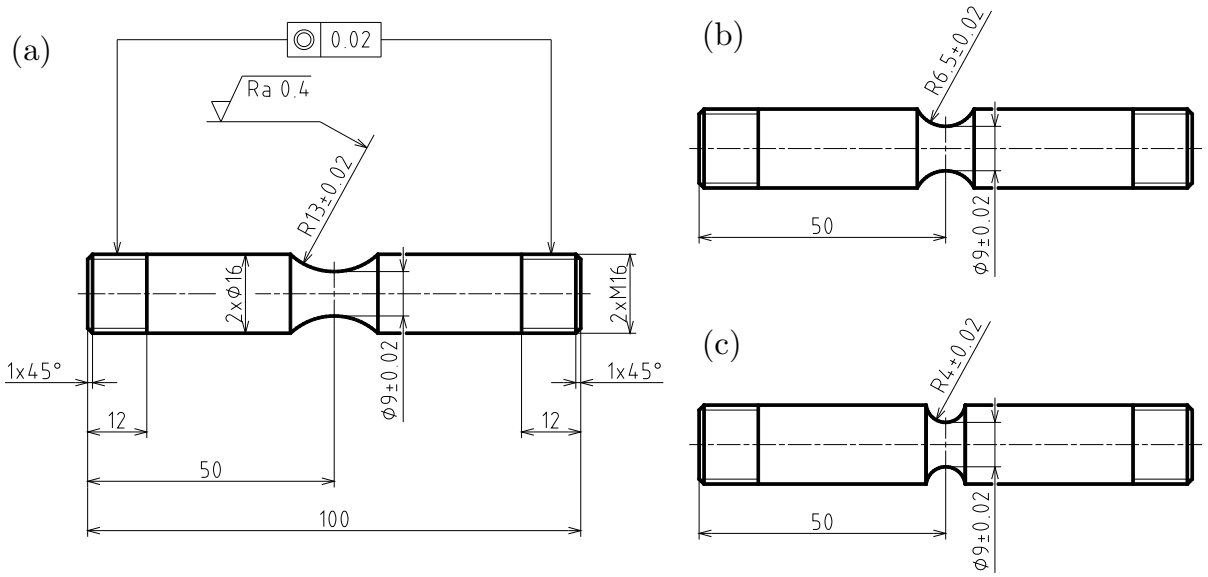

Figure 5.19: Detailed drawing of notched cylindrical specimen: (a) with $d_0 = 9\,\text{mm}$, $R = 13\,\text{mm}$; (b) with $d_0 = 9\,\text{mm}$, $R = 6.5\,\text{mm}$; (c) with $d_0 = 9\,\text{mm}$, $R = 4\,\text{mm}$.

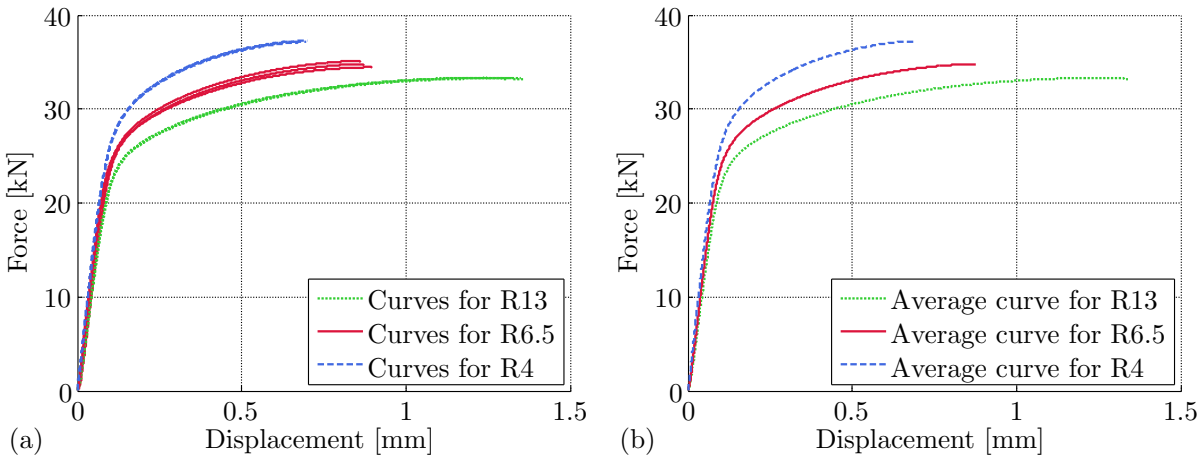

Figure 5.20: Force–displacement responses of notched round bars: (a) for 3 tensile tests per the notch radius; (b) for the average ones distinguished via the notch radius.

Force–displacement curves together with the average ones are depicted in Figure 5.20 where the notch sensitivity may be clearly seen.

The post-mortem specimens of all three geometries are shown in Figure 5.21.

Figure 5.21: Post-mortem notched cylindrical specimens: (a) with $d_0 = 9\,\text{mm}$, $R = 13\,\text{mm}$; (b) with $d_0 = 9\,\text{mm}$, $R = 6.5\,\text{mm}$; (c) with $d_0 = 9\,\text{mm}$, $R = 4\,\text{mm}$.

5.6 Tensile tests of notched tubular specimens

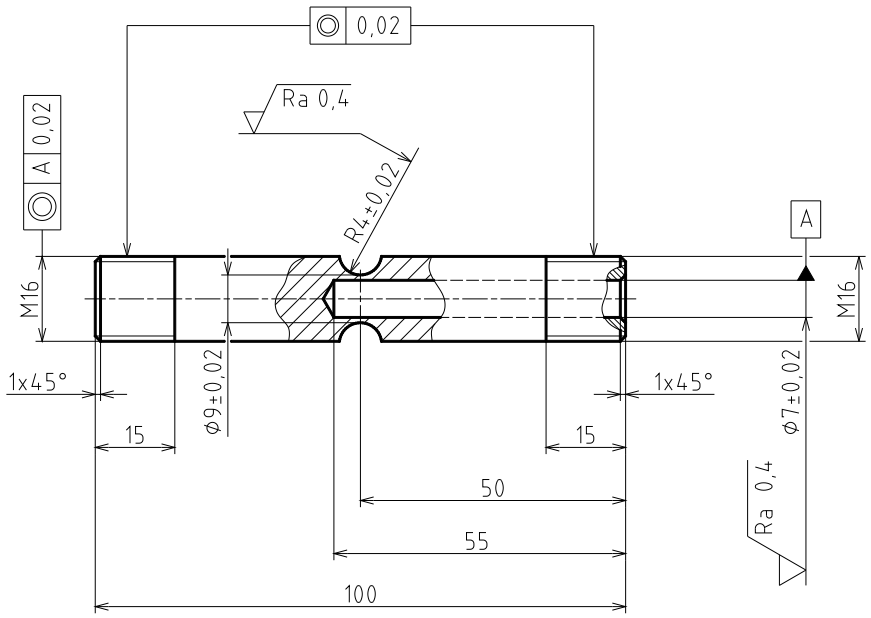

Figure 5.22: Detailed drawing of notched tubular specimen for tensile tests.

Tensile tests of notched tubular specimens were conducted in order to describe the plane strain condition. A detailed drawing of notched tubular specimen is given in Figure 5.22.

Zwick Z250 Allround-Line, tCII, and extensometer Zwick multiXtens were used for tensile testing under the displacement control as well as in previous tensile tests. To ensure the quasi-static loading, the test speed was 1 mm/min during whole test. The gauge length was 30 mm.

Two universal joints[7] were employed between upper and lower grips in order to adjust the perfect alignment of the specimen, with 1 mm thick wall to minimize the loading imperfections. It was in contrast with previous tensile tests, where only one universal joint was used.

Force–displacement curves together with the average ones are depicted in Figure 5.23.

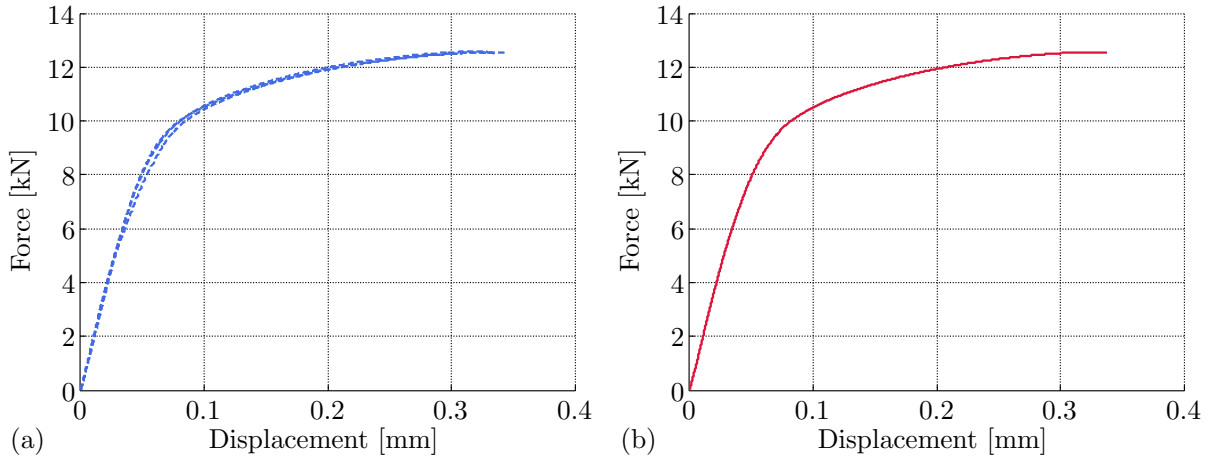

Figure 5.23: Force–displacement: (a) responses for 3 tensile tests of notched tubular specimens; (b) response averaged of all 3 tensile tests of notched tubular specimen.

The post-mortem specimens with present slant fracture are shown in Figure 5.24.

Figure 5.24: Post-mortem notched tubular specimens after tensile tests.

This geometry was alternatively designed instead of flat plate to reliably describe the plane strain under high stress triaxiality, as mentioned in the end of Section 5.2.

[7] Also called Cardan joints.

5.7 Torsion tests of notched cylindrical specimens

Torsion tests were conducted in order to describe the pure shear condition by using notched tubular specimen as depicted in Figure 5.25. Two different diameters in the hole (8 and 8.5 mm) were drilled in order to minimize introducing residual stresses into the thin wall in the finalizing of the hole surface. The tubular specimen was chosen despite there being realized torsion tests of cylindrical specimens [171]. In the case of tube, the fracture initiation may be aligned with the final separation. This is problematic in the case of the cylindrical specimen, where there is almost no straining close to the axis and the initiation moment does not have to be recognised from the torque–twist angle response.

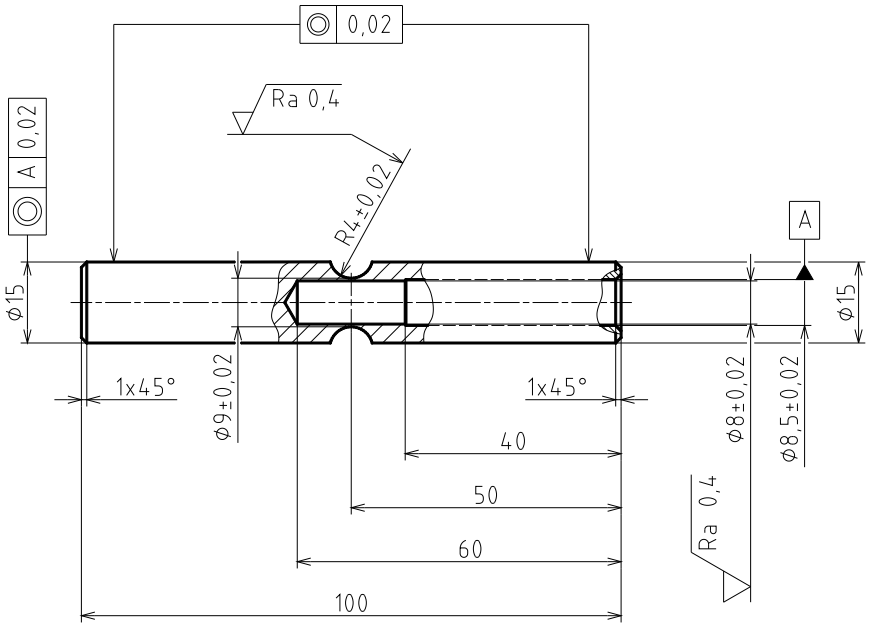

Figure 5.25: Detailed drawing of notched tubular specimen for torsion tests.

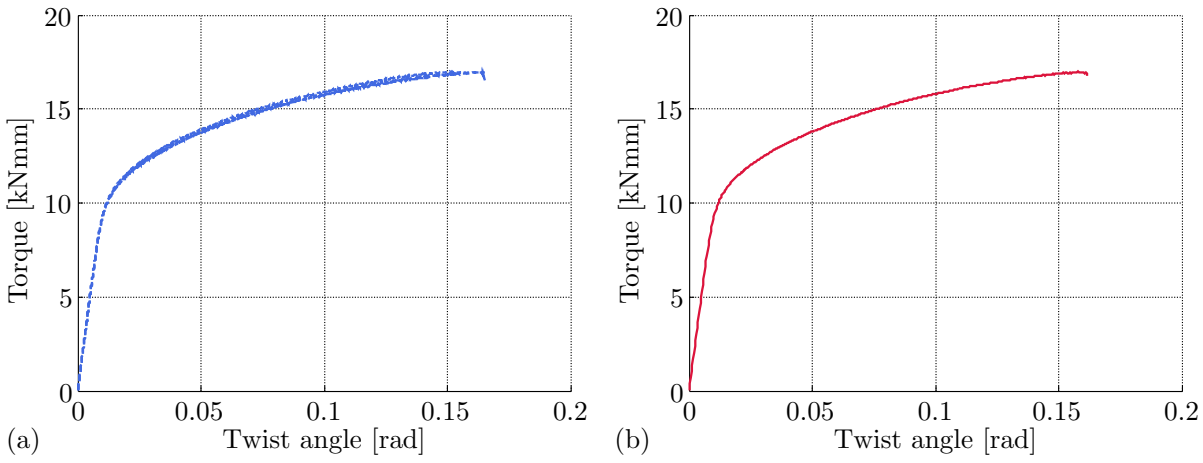

Figure 5.26: Torque–twist angle: (a) curves for 3 torsion tests of notched tubular specimens; (b) curve averaged of all 3 torsion tests of notched tubular specimens.

MTS 809 Axial/Torsional Testing System was used. The test speed was 0.001 rad/s. The twist angle was taken from 646 Hydraulic Collet Grip. It might be better to employ some gauge such as MTS 632.68F-08 High-Temperature Axial/Torsional Extensometer with 25 mm gauge length but in this case, there was unfortunately not enough space to mount it on the specimen.

Torque–twist angle responses together with the average one are depicted in Figure 5.26.

Post-mortem specimens are shown in Figure 5.27.

Figure 5.27: Post-mortem notched tubular specimens after torsion tests.

5.8 Upsetting tests of cylindrical specimens

Five upsetting tests of the cylindrical specimen were carried out according to the detailed drawing in Figure 5.28. The dimensions were designed so that the height to diameter ratio was 1.5 to prevent problems with small strains during loading.

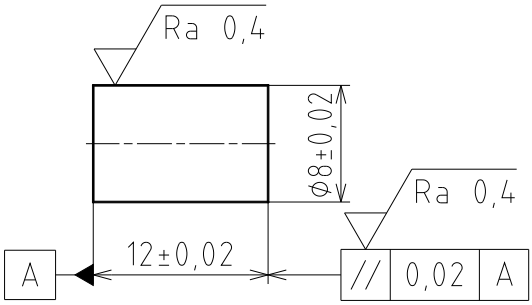

Figure 5.28: Detailed drawing of the cylinder for upsetting tests.

Instron 8801 testing system with dynamic load cell Instron Dynacell ±100 kN and Instron Clip-On strain gauge extensometer were used. During the experiments, the test speed was 1 mm/min.

The force–displacement responses together with the averaged one are depicted in Figure 5.29.

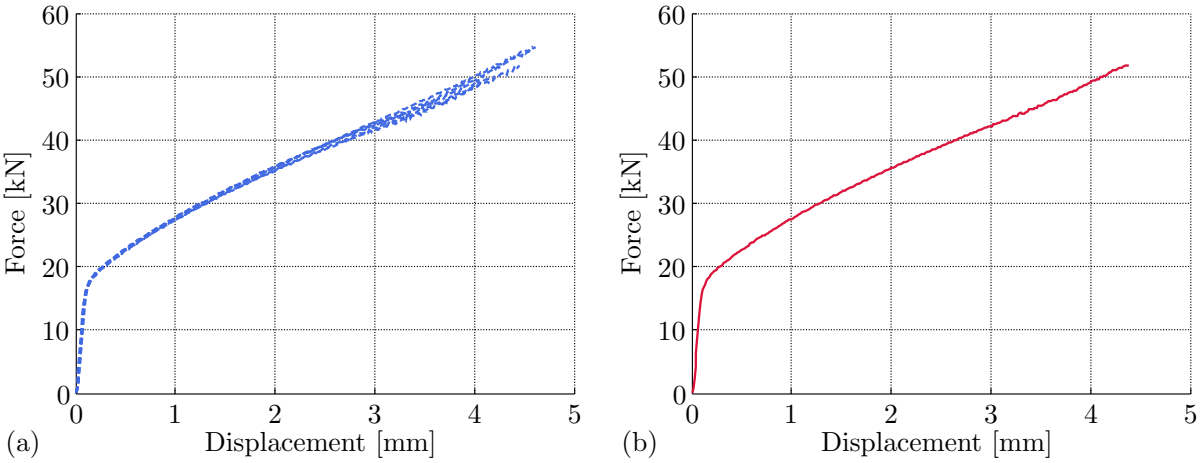

Figure 5.29: Force–displacement: (a) curves for 5 cylindrical specimens loaded in compression; (b) curve averaged of all 5 upsetting tests of cylindrical specimens.

The contact surfaces were lubricated with the molybdenum disulfide (MoS_2) to eliminate the friction. Minor barrelling effect of cylinders can be observed (Figure 5.30) which suggests that there was some amount of friction. The correct value of the friction coefficient had to be iteratively found by numerical simulations of the test, as described further.

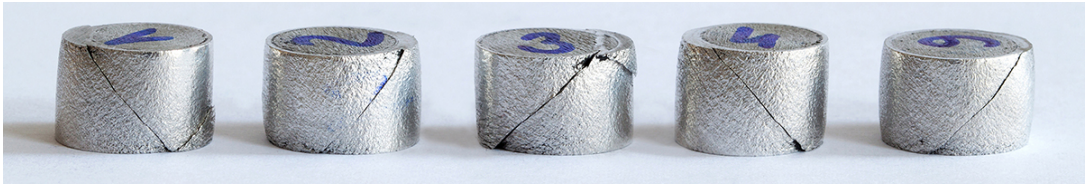

Figure 5.30: Cracked cylindrical specimens after upsetting tests.

6 Stress and strain relationship

For further work, it is necessary to determine the curve which characterizes the material behaviour and gives the relationship between deformation and stress in a plastically deforming solid. Some other basic mechanical properties of AA 2024-T351 were estimated except for the stress–strain curve. Matrix material was assumed to follow von Mises yield criterion obeying associative flow rule[8], no matter which plasticity is used further. Nonetheless, it should be assured that the conditions for tensile test of smooth cylindrical specimen are kept the same in further considerations[9]. The isotropic hardening (Figure 6.1), which is not capable to take into account the Bauschinger effect [5], was adopted.

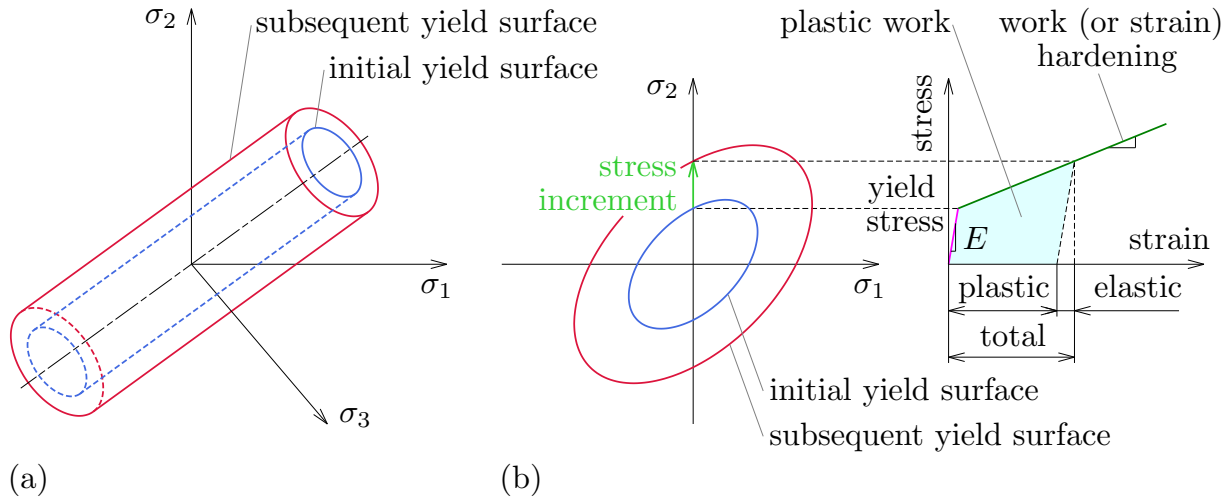

Figure 6.1: Isotropic hardening of von Mises yield surface at Haigh–Westergaard stress space: (a) in three dimensions $(\sigma_1, \sigma_2, \sigma_3)$; (b) in two dimensions (σ_1, σ_2) [182].

The stress–strain relationship is also important in calibration of fracture model. The problem may be solved by using some artificial neural network systems with learning algorithms, due to the coupling effect in scope of continuum damage mechanics, but at this moment it is still too time consuming [189].

[8] Also called associated flow rule.

[9] Including the Lode dependence in plasticity.

There have been many studies developed for estimating the stress–strain curve [35, 106, 164]. First of all, the average force–displacement curve was used for calculating the engineering stress–strain curve (Figure 6.3) through

$$s = \frac{F}{S_0} \qquad \text{and} \qquad e = \frac{\Delta l}{l_0}, \tag{6.1}$$

where s is the engineering stress, F is the force, S_0 is the initial cross-sectional area, e is the engineering strain, Δl is the elongation[10] and l_0 is the gauge length.

Young's modulus was estimated 72.5 GPa using the engineering curve from which the true stress–strain curve (Figure 6.3) was calculated until the ultimate tensile strength by

$$\sigma = s(1+e) \qquad \text{and} \qquad \epsilon = \ln(1+e), \tag{6.2}$$

where σ is the true stress and ϵ is the true strain.

The density was estimated as $\rho = 2770\,\mathrm{kg/m^3}$ by using measured dimensions and weight of the reference block of material.

Poisson's ratio was estimated by using density, Young's modulus and wave velocity. The velocity was measured by using Ultrasonic thickness gauge OLYMPUS 38DL PLUS with contact transducer M110 of 5 MHz. The average value from 5 measuring was $v = 6347\,\mathrm{m/s}$. The wave velocity can be expressed as [43]

$$v = \sqrt{\frac{E}{\rho}\frac{1-\nu}{(1+\nu)(1-2\nu)}}. \tag{6.3}$$

Poisson's ratio was estimated as $\nu = 0.34$ after expressing it from previous equation and solving it within Maple 17.

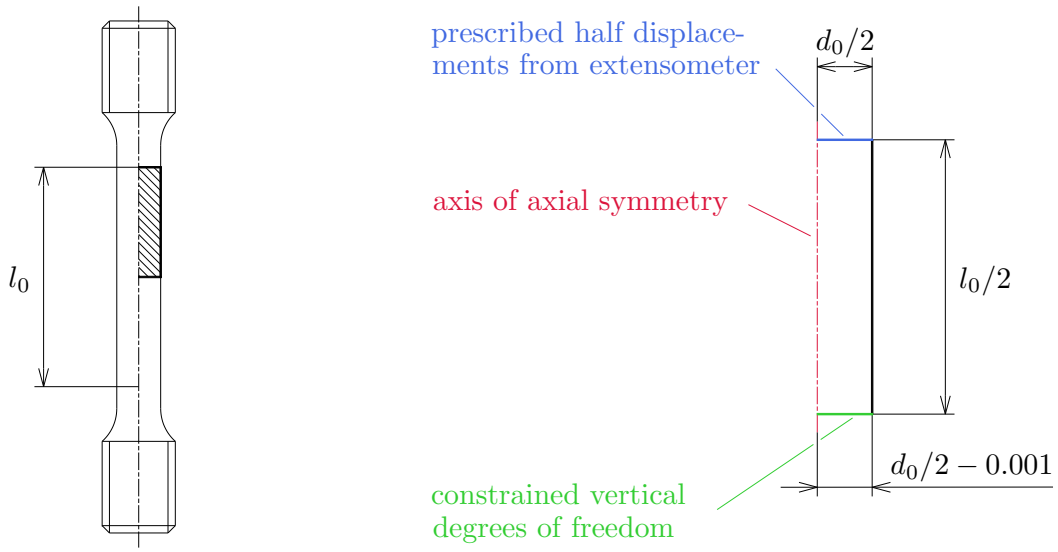

Figure 6.2: Analysis domain and dimensions of tensile coupon for computations.

[10] Also referred as displacement in figures in the present thesis.

Then, the tensile test was numerically simulated within the implicit code of Abaqus. Simplified geometry with boundary conditions is depicted in Figure 6.2. Diameter d_0 was considered 5.91 mm in this particular case, because there was unfortunately not respected requirements on tolerance and it could have played a considerable role. Mapped mesh was created using a 4-node bilinear axisymmetric quadrilateral elements CAX4R with reduced integration, hourglass control and characteristic size of 0.075 mm. Correct deformation of the specimen was ensured by introducing slight imperfection in the bottom (Figure 6.2).

Hereinafter, the mesh size was based on the study of mesh dependence (convergence) carried out earlier in scope of ductile fracture [135, 214, 224, 233] and considering the available hardware[11] as well.

The extrapolated curve of equivalent stress against equivalent plastic strain[12] was determined using the true curve in multi-linear form by trial and error method, on the basis of comparison of force–displacement curves from experiment and computation until the satisfying match was reached (Figure 6.5).

Then, Swift hardening law was fitted to obtained flow curve by using nonlinear least square method within the script in MATLAB R2012b. The law takes form [24]

$$\bar{\sigma} = K(\epsilon^0 + \bar{\epsilon}^p)^n, \tag{6.4}$$

where ϵ^0 is the reference strain. There has been an amount of stress–strain relationships proposed, as by Hollomon [15] or Voce [18]. Swift hardening rule was chosen due to containing both the strength coefficient and strain hardening exponent. Furthermore, the hardening law can be fitted within the plastic deformations and directly used in numerical simulations requiring the plastic response separately from the elastic one. Fitted material constants of Swift hardening law are listed in Table 6.1 and the curve plotted with the use of these constants is depicted in Figure 6.4. It should be noted that the strain hardening exponent is close to the true strain at ultimate tensile strength [108] which was 0.1642.

Table 6.1: Material constants of Swift hardening law for AA 2024-T351.

Strength coefficient [MPa]	Reference strain [–]	Strain hardening exponent [–]
788.60	0.0031	0.1888

Force–displacement curve obtained from numerical simulation by using the fitted flow curve and the one by using Swift hardening law are compared to the experimentally obtained one in Figure 6.5.

[11] 32 GB of random access memory and Intel® Core™ i7-3770 processor with 3.4 GHz frequency.

[12] Also called the flow curve.

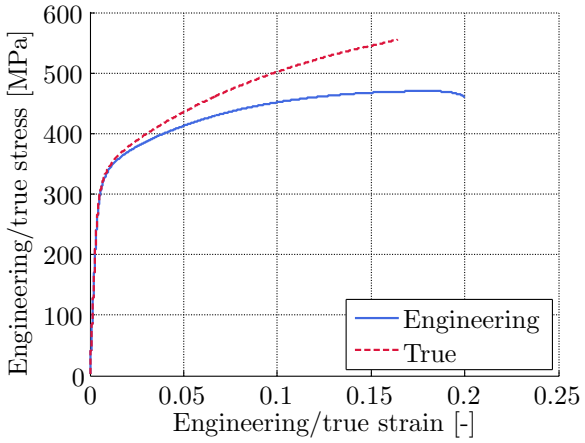

Figure 6.3: Engineering and true stress–strain curves of AA 2024-T351.

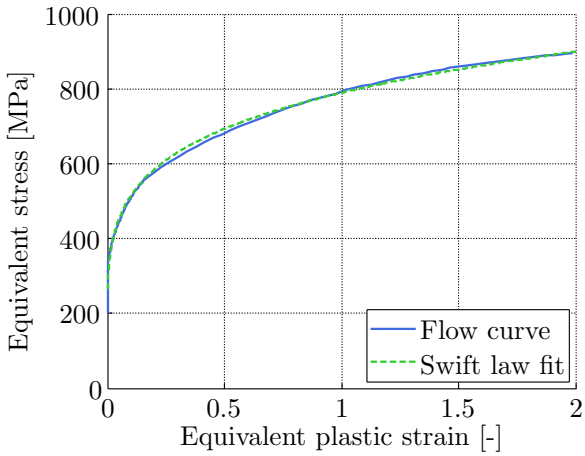

Figure 6.4: Flow curve and fitted Swift hardening law of AA 2024-T351.

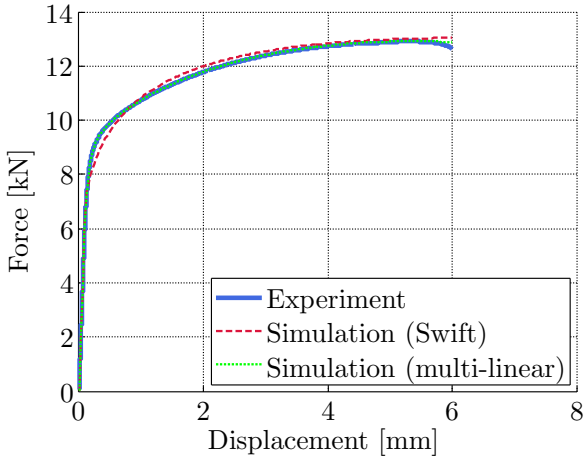

Figure 6.5: Force–displacement curves from experiment and simulations.

7 Damage accumulation

Miner [17] proposed linear cumulative damage rule on the basis of Palmgren hypotheses [10] of fatigue under variable amplitude loading, nowadays the so-called Palmgren–Miner rule. Later on, nonlinear damage accumulation was proposed by Marco and Starkey [27], double linear damage rule by Manson [37], or double damage curve approach by Manson and Halford [67], depicted in Figure 7.1a.

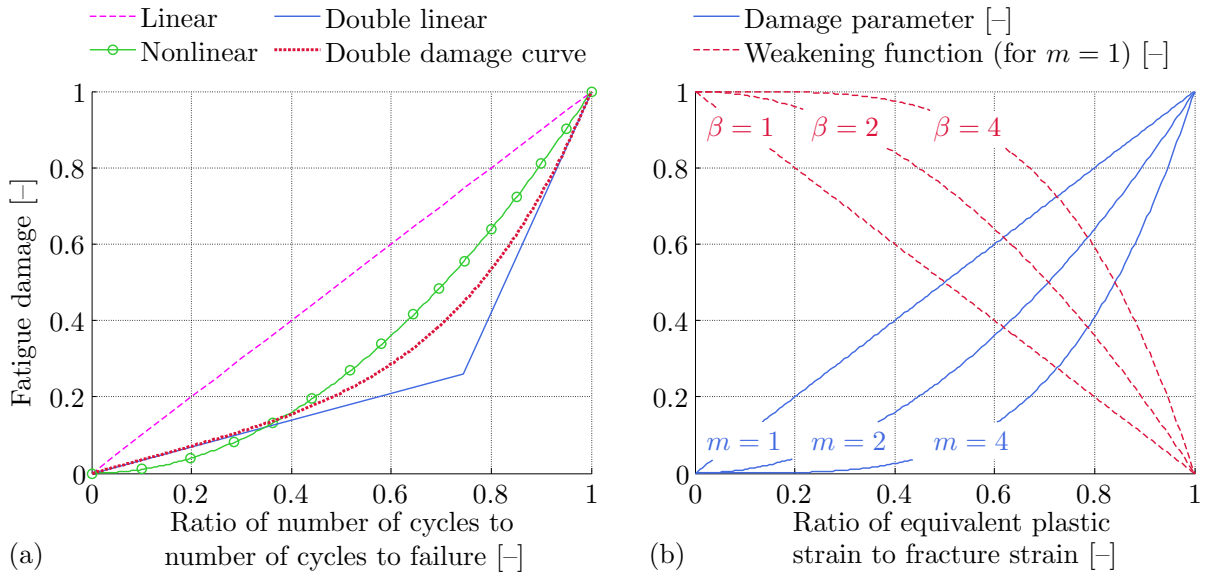

Figure 7.1: Damage accumulation in: (a) fatigue [86]; (b) ductile fracture.

Similar approach may be found in ductile fracture related problems. The damage had been assumed as linear function of equivalent plastic strain in the beginnings and it has been considered as nonlinear in the course of time. The damage accumulation, stated as acceleration process analogically to approach of Marco and Starkey [27], which degenerates into linear function when $m = 1$ is adopted, can be expressed as [120]

$$D = \left(\frac{\bar{\epsilon}^p}{\bar{\epsilon}^f} \right)^m . \tag{7.1}$$

The greater the damage, the more the material weakens. Damage accumulation with material weakening is illustrated in Figure 7.1b. The case study of using different damage accumulation is given in Appendix B.

7.1 Stepwise experiments

Xue [120] proposed to derive the damage exponent using stepwise experiments as later used by Basu and Benzegra [230] for studies of the loading path dependence. Two tensile tests of cylindrical specimens (Figure 7.2a) with different stress triaxiality are run until fracture. Then, a larger specimen is pulled onto prescribed deformation, less than the one needed for fracture, the test is interrupted and the deformed specimen is machined into a smaller specimen, inducing different stress triaxiality under tensile loading so that the loading path is changed (Figure 7.2b). Finally, the smaller specimen is pulled until fracture.

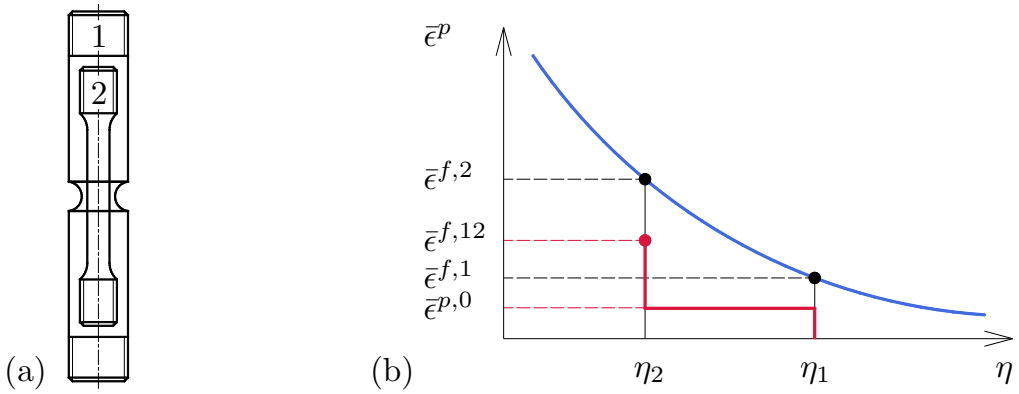

Figure 7.2: Stepwise experiment: (a) specimens; (b) nonproportional loading path.

Then, the damage exponent can be determined by integrating the damage along the nonproportional loading path by using variables defined by Figure 7.2b as

$$D = \left(\frac{\bar{\epsilon}^{p,0}}{\bar{\epsilon}^{f,1}}\right)^m + \left(\frac{\bar{\epsilon}^{f,12}}{\bar{\epsilon}^{f,2}}\right)^m - \left(\frac{\bar{\epsilon}^{p,0}}{\bar{\epsilon}^{f,2}}\right)^m = 1. \tag{7.2}$$

Xue [120] estimated the damage exponent $m = 2$ on the basis of Bridgman's results [35] who changed the stress triaxiality not by means of specimen's geometry but by elevated hydrostatic pressure in extensive experimental campaign.

Stepwise testing was conducted within the present study as well. A notched cylindrical specimen with $d_0 = 9\,\text{mm}$ and $R = 4\,\text{mm}$ depicted in Figure 5.19c was used for the first step. A smooth cylindrical specimen with certain imperfection (Figure 7.3) was used in the second step. The initial imperfection was used in order to ensure the fracture occurrence in the locus where the root of the notch of previous specimen was.

It should be noted that the evaluation of such experiments yields some error due to using the total equivalent strain instead of a plastic one. The elastic part of total strain should be separated. Strains $\bar{\epsilon}^{p,0}$, $\bar{\epsilon}^{f,1}$, $\bar{\epsilon}^{f,2}$ and $\bar{\epsilon}^{f,12}$ are rather total values than plastic ones and also uniaxial, because those were calculated from necking of the specimen. Assuming the volume constancy, total equivalent strain may be related to actual and initial diameter of the round bar, d and d_0, respectively, according to Figure 5.8a through

$$\bar{\epsilon} = 2\ln\frac{d_0}{d}. \tag{7.3}$$

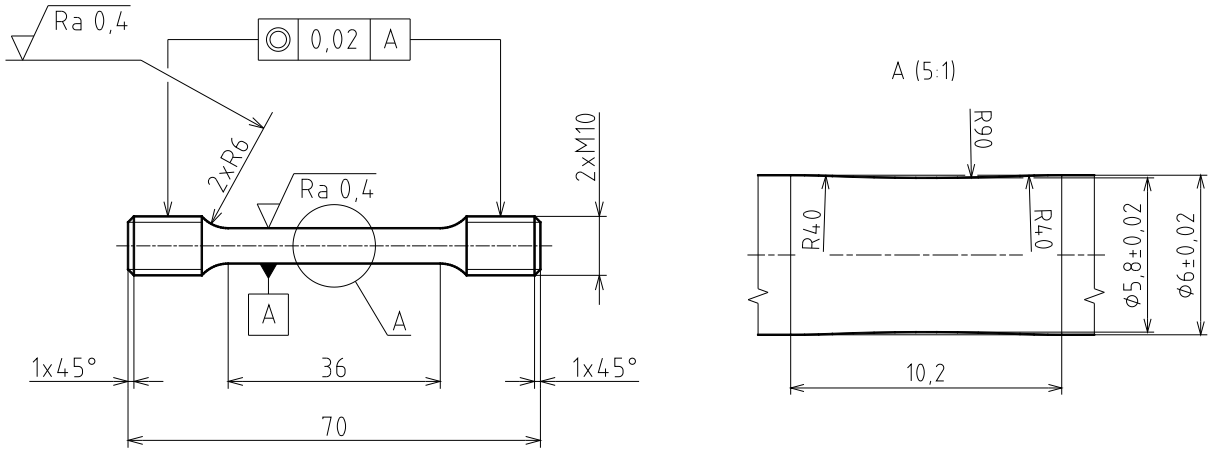

Figure 7.3: Smooth cylindrical specimen with initial geometrical imperfection.

If uniform equivalent strain over the minimum cross-sectional area of the neck is assumed, the fracture strain can be, using d_f as the diameter after tensile test, expressed as

$$\bar{\epsilon}^f = 2 \ln \frac{d_0}{d_f}. \tag{7.4}$$

The experiments were conducted in two levels of prestrain $\bar{\epsilon}^{p,0}$. There were used always 3 specimens for each level to provide higher reliability. The damage exponent estimations are summarized in Table 7.1.

Table 7.1: Damage exponents for AA 2024-T351.

$\bar{\epsilon}^{p,0}$ [–]	$\bar{\epsilon}^{f,1}$ [–]	$\bar{\epsilon}^{f,2}$ [–]	$\bar{\epsilon}^{f,12}$ [–]	m [–]
0.055	0.163	0.251	0.239	1.72
0.100			0.244	4.13

There is a huge discrepancy in results so the sensitivity analysis follows. The case of $\bar{\epsilon}^{p,0} = 0.100$ was chosen (see Table 7.1). Then, the influence of $\bar{\epsilon}^{p,0}$ and $\bar{\epsilon}^{f,12}$ on the damage exponent was studied.

The value of prestrain $\bar{\epsilon}^{p,0}$ may be influenced by choice. Therefore it is desirable to keep it low compared to $\bar{\epsilon}^{f,1}$ so as to maintain $\bar{\epsilon}^{f,12}$ in reasonable range where the damage exponent does not change dramatically, such as in case when the $\bar{\epsilon}^{f,12}$ approaches $\bar{\epsilon}^{f,2}$ (Figure 7.4).

Marini et al. [69] and Tai [74] also conducted extensive stepwise testing. The damage exponent calculations are given in Appendix C. Anyway, it is apparent that this approach is highly unstable and sensitive to input data. Therefore, it is not convenient for the damage exponent calibration in the present form and another technique should be introduced, as described further.

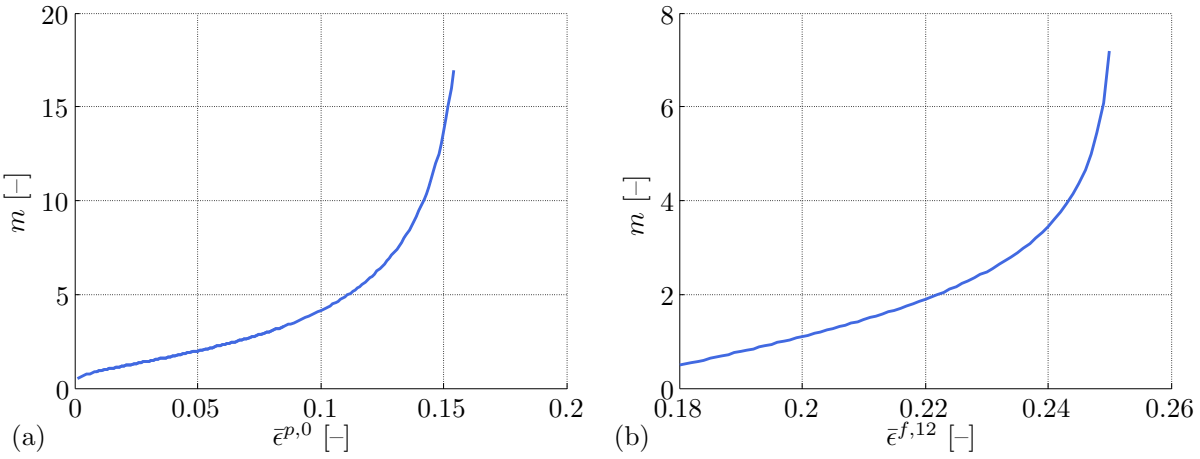

Figure 7.4: Sensitivity analysis of damage exponent on: (a) $\bar{\epsilon}^{p,0}$;(b) $\bar{\epsilon}^{f,12}$.

7.2 Cyclic loading

Xue [126] presented another approach of estimating the damage exponent on the basis of low cycle fatigue, where the plastic strain is responsible for the damage as well[13] and obtained $m = 1.73$ by using the curve of plastic strain amplitude against number of cycles to fracture of AA 2024-T6[14] [31]. Xue [134] also obtained $m = 2.04$ for the same material and experimental data set in the publication where a unified expression for low cycle and ultra low cycle fatigue was proposed, but over a different range of number of cycles to fracture. In addition, there has been apparent endeavour to find a smooth transition between the monotonic and low cycle loading in ultra low cycle fatigue[15] [210].

The so-called Manson–Coffin relationship reads [25, 26]

$$\epsilon^{p,a} = \epsilon'_f N_f^c, \tag{7.5}$$

where $\epsilon^{p,a}$ is the plastic strain amplitude, ϵ'_f is the fatigue ductility coefficient, N_f is number of cycles to fracture and c is the fatigue ductility exponent.

The experimental data after Coffin and Tavernelli [31] were also fitted by Manson–Coffin relationship here. Nonlinear least square method with Levenberg–Marquardt algorithm within MATLAB graphical user interface was used. The result is plotted in Figure 7.5 for $\epsilon'_f = 0.289$ and $c = -0.553$. Those values are comparable to results presented by Osgood for AA 2024-T351, $\epsilon'_f = 0.22$ and $c = -0.59$ [61]. It should be noted that the value of the fatigue ductility coefficient is close to the fracture strain for monotonic tension [36, 107] which was 0.2346 in numerical simulation conducted in Chapter 6. Finally, Xue [126] derived the relationship between damage exponent and fatigue ductility coefficient as

$$m = -\frac{1}{c}. \tag{7.6}$$

Then, the damage exponent is $m = 1.81$ for $c = -0.553$ by using the previous equation.

[13] As independently investigated by Manson [25] and Coffin [26] in scope of thermal fatigue.

[14] Solution heat treated, then artificially aged.

[15] Also called extremely low cycle fatigue.

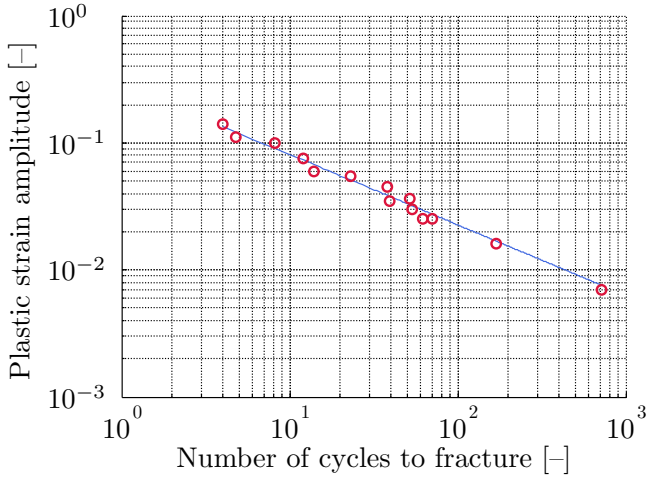

Figure 7.5: Fit to experiments of 2024-T6 after Coffin and Tavernelli [31].

Another method of the damage exponent estimation is to follow the Young's modulus degradation. When $\tilde{E}$ is actual degraded Young's modulus, the concept of effective stress together with strain equivalence hypothesis give [65]

$$D = 1 - \frac{\tilde{E}}{E}. \tag{7.7}$$

Celentano and Chaboche [127] conducted the measurement up to fracture on two steels which was later done by Tsiloufas and Plaut [180] as well. Ravindran [155] measured the Young's modulus degradation by means of cyclic test on aluminium alloy 2024-T3[16]. Displacements were controlled by cross-head of Instron 8032 servohydraulic fatigue testing machine and deformations were measured by Dantec Dynamics Q-400 DIC (Digital Image Correlation) System. Young's modulus of elasticity gradually decreased from 67.8 GPa to the value of 43.9 MPa. It is not possible to determine the ultimate tensile strength for further examination of Ravindran's results due to direct measuring of true strain.

Instead, loading/unloading testing was carried out in order to study the damage evolution here. Three specimens with geometry depicted in Figure 5.10 were loaded in tension and after each 2 % of total engineering strain unloaded and then loaded again. Testing machine Zwick Z250 Allround-Line, tCII, and Zwick multiXtens extensometer were used for the testing with the test speed 1 mm/min. Representative history of loading is given in Figure 7.6a. Values of true plastic strain were subtracted from the curves in Figure 7.6b–d at the moment when the specimens were fully unloaded. Young's moduli were estimated by using slopes produced by unloading and repetitive loading and plotted against values of true plastic strain in Figure 7.7a. Values of damage parameter were calculated by using Equation 7.7 and plotted against the ratio of true plastic strain to fracture strain in Figure 7.7b. The fracture strain 0.2346 obtained from numerical simulation conducted in Chapter 6 was used. This technique is applicable only until the ultimate tensile strength. Beyond this limit the variables are integrated along the gauge length whereas local values should have been needed to measure during necking.

[16] Solution heat treated, then cold worked.

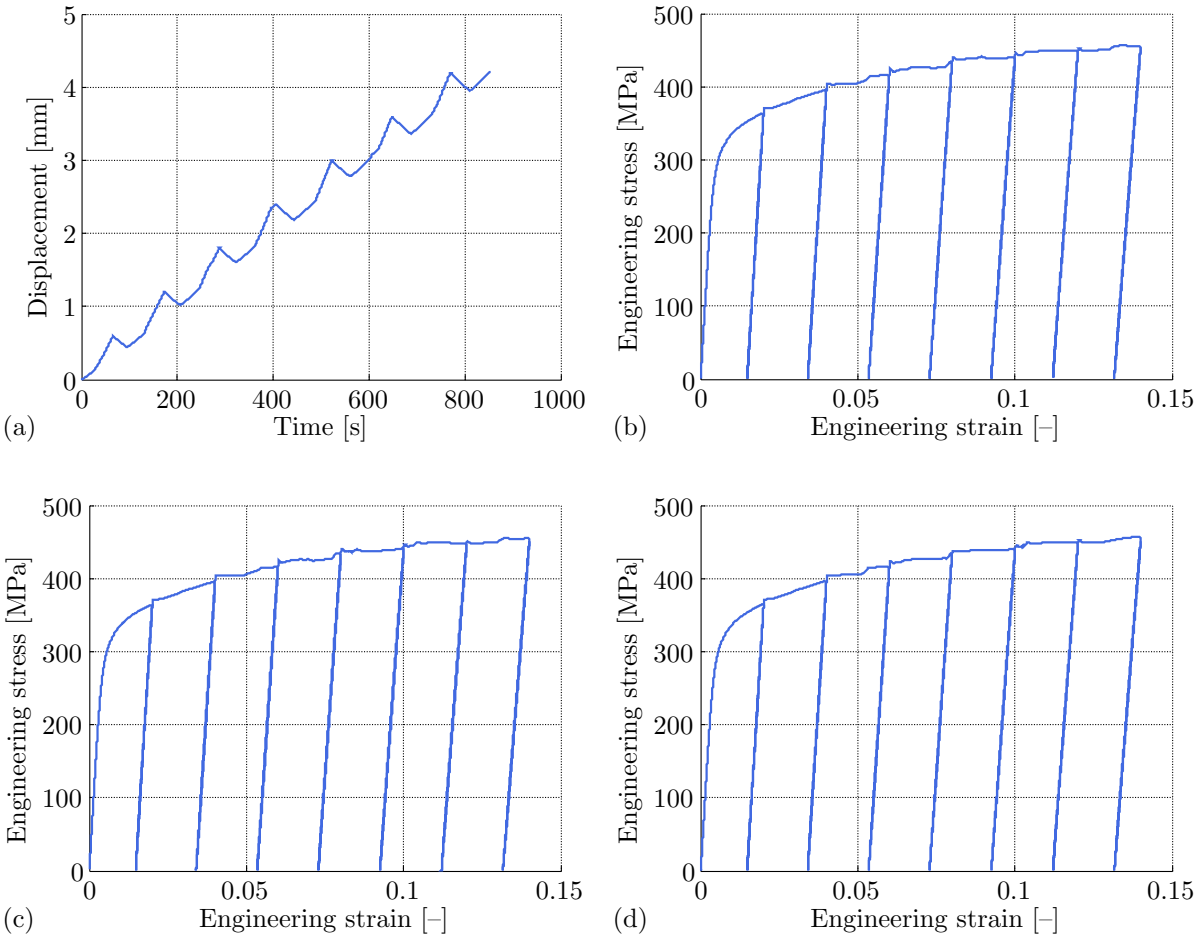

Figure 7.6: Loading/unloading in tension: (a) history of loading in time for specimen number 3; (b) stress–strain response for specimen number 1; (c) stress–strain response for specimen number 2; (d) stress–strain response for specimen number 3.

Experimentally obtained results exhibit linear trend and therefore the power-based model in Equation 7.1 is not capable to fit the data properly. The double damage curve approach introduced by Manson and Halford [67] for cumulative fatigue damage was revisited and applied to ductile fracture here. The original relationship for fatigue damage reads

$$D_f = \frac{0.35\left(\frac{N_r}{N_f}\right)^{0.25}}{1-0.65\left(\frac{N_r}{N_f}\right)^{0.25}}\frac{N}{N_f} + \left(1-\frac{0.35\left(\frac{N_r}{N_f}\right)^{0.25}}{1-0.65\left(\frac{N_r}{N_f}\right)^{0.25}}\right)\left(\frac{N}{N_f}\right)^{\left(\frac{N_f}{N_r}\right)^{0.40}}, \tag{7.8}$$

where N_r is the reference life coefficient and N is the number of cycles.

The first fraction in previous equation, which is repeated before the second term, represents the slope of the first damage accumulation line in the double linear damage rule and it is replaced by first material constant q_1. The second material constant q_2 is the exponent of the second term, so the reference life coefficient is entirely omitted.

Replacing the ratio of number of cycles to the number of cycles to failure by the ratio of equivalent plastic strain to fracture strain gives

$$D_s = q_1 \frac{\bar{\epsilon}^p}{\bar{\epsilon}^f} + (1 - q_1) \left(\frac{\bar{\epsilon}^p}{\bar{\epsilon}^f} \right)^{q_2} . \tag{7.9}$$

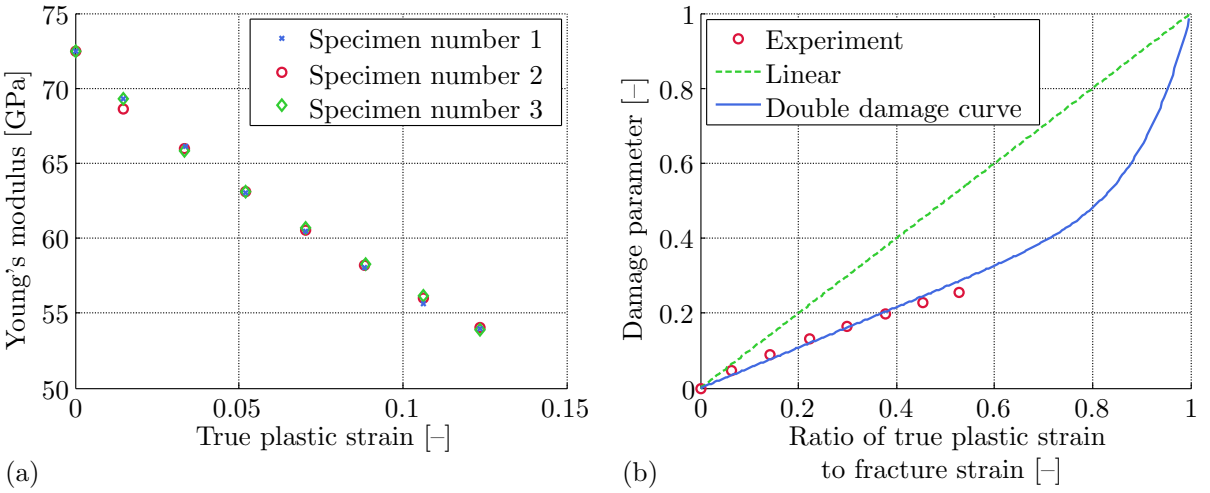

Figure 7.7: Material degradation expressed by: (a) measured Young's modulus; (b) calculated damage parameter against ratio of true plastic strain to fracture strain.

First of all, the slope of initial linear part of damage accumulation was estimated as $q_1 = 0.54$ by using the trial and error method. Then, the second material constant was estimated as $q_2 = 10$ by using the trial and error method again, in order to reasonably extrapolate the damage accumulation to failure (Figure 7.7b).

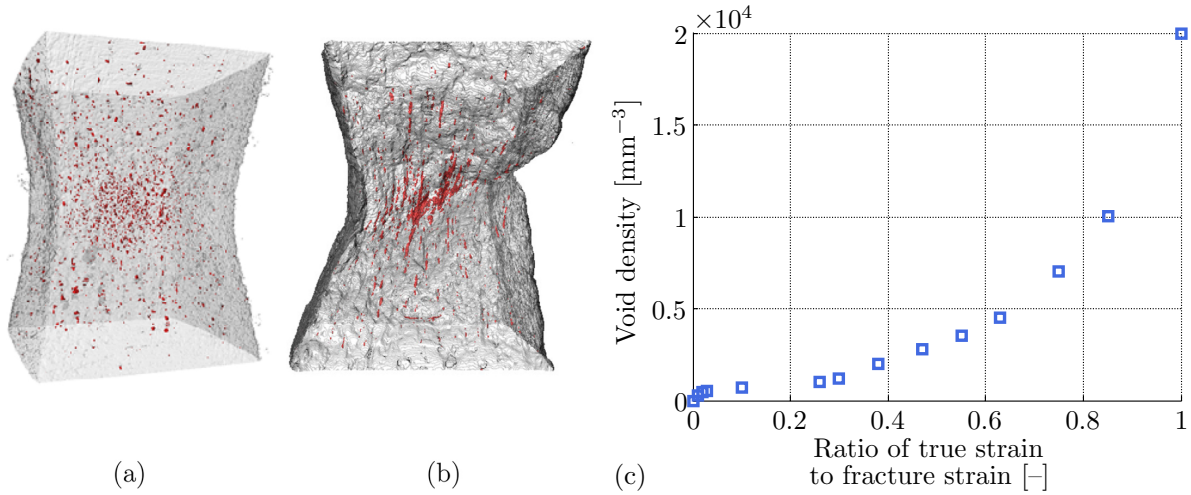

Figure 7.8: Voids: (a) in dual phase steel just before fracture; (b) in AISI 316L austenitic steel just before fracture; (c) per volume against ratio of true and fracture strain for AISI 316L by using 3D X-ray tomography (after Fabrègue et al. [198]).

The presented results are consistent with those obtained by 3D X-ray tomography in scope of micromechanics where the porosity, or void volume fraction and the void density, is related to ductile damage [170, 192, 198].

There are depicted voids in specimens in Figure 7.8a–b and void density against ratio of true strain to fracture strain in Figure 7.8c. It is apparent that the damage does not accumulate linearly but the damage rate is gradually increasing.

Extending the measurement beyond the onset of plastic instability would have been possible by employing the DIC or ultrasound, but it seems to be far more complicated.

Nevertheless, it is certain that the process of damage accumulation needs further investigation, after the plastic instability in particular.

It should be noted that there was also some anelastic behaviour observed in loading/unloading testing, as depicted in Figure 7.9, due to reversible motion of dislocations in elastic range.

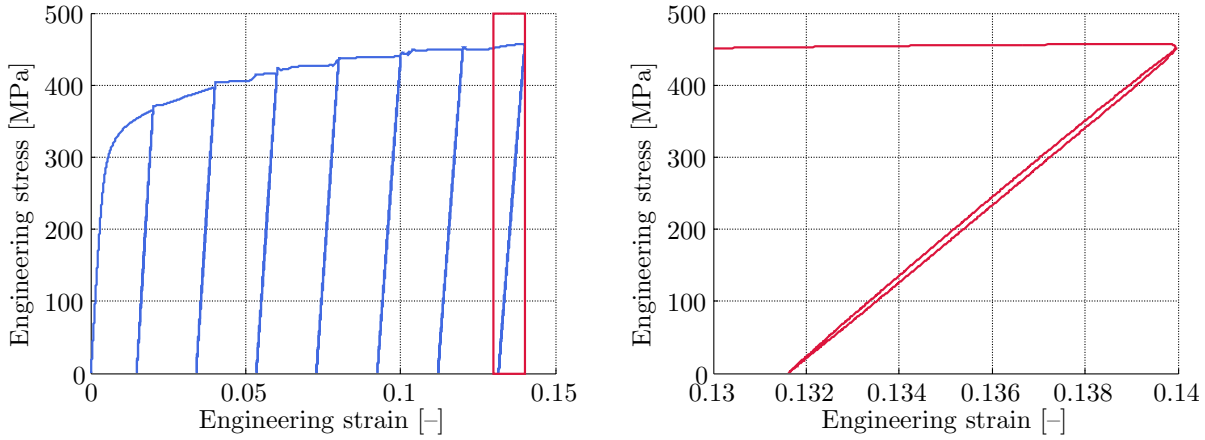

Figure 7.9: Anelastic behaviour in loading/unloading testing of specimen 3.

Nevertheless, the anelastic behaviour will not be discussed further because it is negligible in the present point of view.

8 Material weakening

Material weakening is responsible for irreversible microstructural deterioration. It is also governing the coupling of plasticity with fracture model. Basing on Equation 4.44, of which the effect is depicted in Figure 7.1b, and laying the flow curve of matrix equal to conventional flow curve[17], the yield condition may be written as

$$\Phi = \bar{\sigma} - (1 - D_s)\sigma_Y = \bar{\sigma} - (1 - D^{\beta})\sigma_Y = 0, \tag{8.1}$$

where the damage parameter from Equation 7.9 can be written in a rate form as

$$\dot{D}_s = q_1 \frac{\dot{\bar{\epsilon}}^p}{\bar{\epsilon}^f} + q_2(1 - q_1) \left(\frac{\bar{\epsilon}^p}{\bar{\epsilon}^f} \right)^{q_2 - 1} \frac{\dot{\bar{\epsilon}}^p}{\bar{\epsilon}^f}. \tag{8.2}$$

The influence of calibrated double damage curve approach together with simple coupling ($\beta = 1$) is depicted in Figure 8.1 for a tension of the smooth cylindrical specimen until fracture estimated in Chapter 6. The weakening exponent was set as $\beta = 3$ in order to keep the material behaviour unchanged until the proximity of final rupture, among others, to allow to realize the calibration as proposed further. The rapid material deterioration in the end of damage process correspondents to experimental observations and correlates to development of macrocracks in material, leading to violating the structural integrity.

However, setting the weakening exponent $\beta = 3$ itself would led in underestimating the experimentally obtained force–displacement response. Therefore, there was introduced fracture strain correction coefficient C raising the actual fracture strain. It was calibrated as $C = 0.12$ by the trial and error method until the satisfying match in force–displacement curve was reached (Figure 8.2). So the increase of fracture strain in case of tension of the smooth cylindrical specimen is approximately 51 %. Moreover, the final part beyond the ultimate tensile strength exhibited better performance when compared to simulation with no damage accumulation or material weakening (Figure 6.5). Finally, the damage evolution can be rewritten in the final integral form as

$$D_s = \int_0^{\bar{\epsilon}^f} q_1 \frac{\mathrm{d}\bar{\epsilon}^p}{C + \bar{\epsilon}^f} + \int_0^{\bar{\epsilon}^f} q_2(1 - q_1) \left(\frac{\bar{\epsilon}^p}{C + \bar{\epsilon}^f} \right)^{q_2 - 1} \frac{\mathrm{d}\bar{\epsilon}^p}{C + \bar{\epsilon}^f}. \tag{8.3}$$

[17] The conventional flow curve is in yield function in Equation 8.1 represented by σ_Y which is not used for description of stress and strain relation in Equation 6.4 where there is $\bar{\sigma}$, which might be confusing.

The simulation of tensile test was performed the same as in Chapter 6 but in explicit code of Abaqus. VUMAT was used for incorporating the double damage curve (damage accumulation) and material weakening.

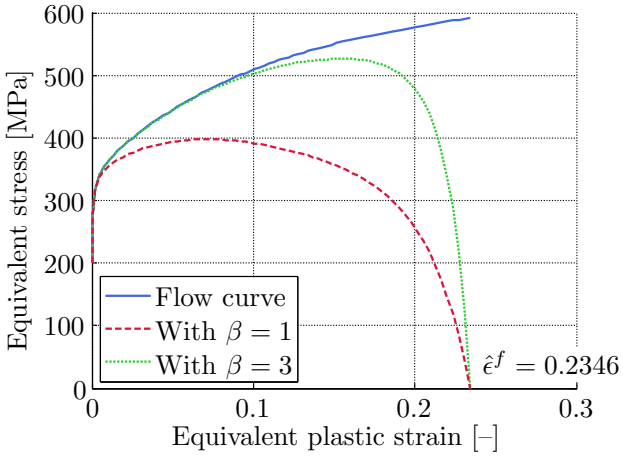

Figure 8.1: Illustration of material behaviour with incorporation the damage accumulation and material weakening in stress–strain curves of smooth round specimen.

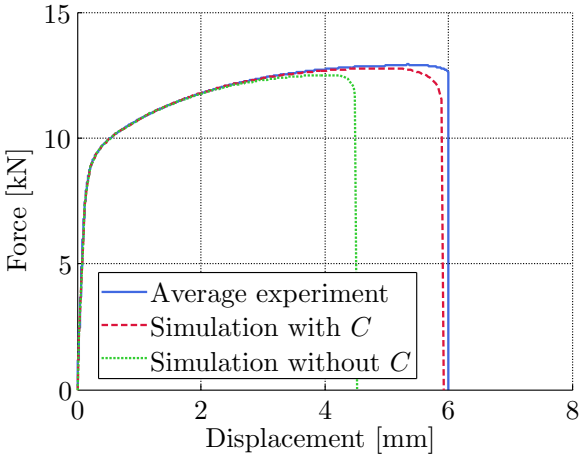

Figure 8.2: Force–displacement responses of the smooth round specimen after incorporation of the damage accumulation, material weakening and correction coefficient.

Gruben et al. [190] used $\beta = 6$ and assumed that the plastic work (the area under stress–strain curve) has to be same for coupled and uncoupled approach. Then, the fracture strain was increased by 13 %. Haltom et al. [200] compared experimentally measured strains by using a grid to strains measured on the grain level. It was found that grain based strains were between 25 % and 100 % higher than those measured by using grid.

Basically, the proposed approach combines advantages of both uncoupled and coupled ductile fracture models yielding in the approach similar to partially coupled models. Using the simplicity of calibration procedure of uncoupled models and complexity of coupled ones, it gives powerful tool for modelling the ductile fracture as illustrated in Chapter 11.

9 Plasticity

All fracture tests were simulated with the use of von Mises yield criterion using the implicit code, as described in Chapter 6. But it was found that force–displacement responses do not match the experiments, so it was necessary to employ more complex plasticity to better describe the material behaviour. It was important because results of these simulations were direct inputs into the ductile fracture model calibration procedure and because the plasticity directly influences the damage accumulation. The fracture strain may be determined directly by DIC during the experiments in the case of specimens where the crack initiation is on the surface [158]. The DIC was not employed because not all specimens have the fracture that initiates on the surface. Instead, the critical displacement or twist angle were used in order to indicate the crack initiation by means of sudden decrease of loading. It was assumed that the crack initiation was followed by rapid crack growth until total separation. Therefore, those phenomena might be considered as simultaneous. Then, the fracture strain can be obtained from numerical computations together with evolutions of state variables from the crack initiation loci. This might be determined on the basis of experimental observation or fractography.

This work does not attempt to give an extensive description of developed yield criteria but only a brief overview. In the beginnings, Tresca [2] proposed J_2 and J_3 dependent plasticity having hexagonal shaped yield locus in a deviatoric plane. Mohr [6] assumed that the critical shear stress depends also on the normal stress applied on the shearing plane and not only on maximum shear stress, and generalized Coulomb friction law [1] to form of a conical yield surface with irregular hexagon shaped yield locus in a deviatoric plane. The so-called von Mises yield criterion, which has a cylindrical shape in Haigh–Westergaard space, was first presented by Huber [7] on the basis of shear energy[18]. It was proposed by von Mises [8] that yielding occurs as J_2 reaches a critical value, hence the frequently used designation J_2 plasticity. Later, Hencky [9] interpreted it as a critical value of elastic energy of distortion. Drucker and Prager [23] presented I_1 and J_2 dependent plasticity having a conical yield surface in scope of soil mechanics. Later, Hosford [45] developed non-quadratic yield function. Brünig et al. [93] proposed I_1, J_2 and J_3 dependent plasticity with non-associated flow rule. Besides the fracture model, Bai and Wierzbicki [135] introduced plasticity dependent on all three stress invariants with deviatoric associated flow rule, which means that the direction of plastic flow is normal to the yield surface only in a deviatoric plane. Last but not least, Gao et al. [160] presented the plasticity dependent on all three stress invariants as well, but with non-associated flow rule.

[18] There is actually evidence that Maxwell communicated the idea in a letter to Kelvin in 1856 [80].

The J_2 and J_3 dependent plasticity proposed by Kroon and Faleskog [206] was adopted as it preserves the behaviour of uniaxial axisymmetric tension[19] the same as in J_2 plasticity which was used for calibration of flow curve and material weakening, so the assumption from Chapter 6 was satisfied. It is also able to describe strong Lode dependence like Tresca yield criterion. Moreover, the yield function is smooth so no singular points on the yield surface have to be treated although it is possible [56, 140].

The yield function with weakening reads

$$\Phi = \bar{\sigma} - \left(1 - D^{\beta}\right) \sigma_Y k, \tag{9.1}$$

where k is the yield correction function having the form

$$k = 1 - \gamma\omega \left(\frac{1 + \omega_0^{-a}}{\omega^{-a} + \omega_0^{-a}} \right)^a, \tag{9.2}$$

where γ, ω_0 and a are three material constants and ω is the normalized Lode parameter [141]

$$\omega = 1 - \xi^2 = \sin^2(3\theta_L). \tag{9.3}$$

The Drucker's postulate [19, 22, 30] defining the stable material was assumed. It demands for positive change in plastic work for any quasi-cycle of load

$$\mathrm{d}\boldsymbol{\sigma} : \mathrm{d}\boldsymbol{\epsilon}^p \geq 0, \tag{9.4}$$

which implies that the yield surface must be convex. It also demands for the normality of the flow rule as described further. Nevertheless, there are some cases when the metal plasticity was assumed as non-convex [167, 234].

The convexity might be verified on the basis of curvature in polar coordinates

$$\kappa = \frac{\varrho^2 + 2\left(\frac{\mathrm{d}\varrho}{\mathrm{d}\theta_L}\right)^2 - \varrho\frac{\mathrm{d}^2\varrho}{\mathrm{d}\theta_L^2}}{\left(\varrho^2 + \left(\frac{\mathrm{d}\varrho}{\mathrm{d}\theta_L}\right)^2\right)^{\frac{3}{2}}}, \tag{9.5}$$

where ϱ is the polar coordinate of the yield surface in the deviatoric plane given as

$$\varrho = \sqrt{\frac{2}{3}}\sigma_Y k. \tag{9.6}$$

Individual derivatives with respect to Lode angle are, respectively, as follows

$$\frac{\mathrm{d}k}{\mathrm{d}\theta_L} = -3\gamma \frac{\left(1 + \omega_0^{-a}\right)^a \omega_0^{-a}}{\left(\omega^{-a} + \omega_0^{-a}\right)^{a+1}} \sin(6\theta_L), \tag{9.7}$$

$$\frac{\mathrm{d}^2k}{\mathrm{d}\theta_L^2} = 9\gamma \frac{\left(1 + \omega_0^{-a}\right)^a \omega_0^{-a}}{\left(\omega^{-a} + \omega_0^{-a}\right)^{a+1}} \left[\frac{a+1}{a} \frac{\omega^{-a}}{\omega^{-a} + \omega_0^{-a}} 4(1-\omega) + 2(2\omega - 1) \right]. \tag{9.8}$$

Material constants of the plasticity were adjusted so as the yield surface was convex ($\kappa \geq 0$) and exhibited Tresca-like behaviour, yet with round corners. The curvature acquiring positive values is plotted in Figure 9.1 for constants given in Table 9.1. The yield surface in the deviatoric plane is depicted for the calibrated set of constants in Figure 9.2.

[19] And also the axisymmetric compression which was captured by von Mises plasticity well too.

Table 9.1: Material constants of Kroon–Faleskog plasticity for AA 2024-T351.

γ [–]	ω_0 [–]	a [–]
0.123	0.18	4

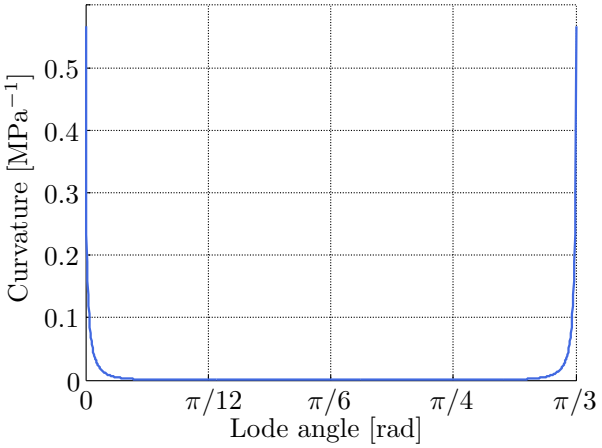

Figure 9.1: Calibrated plasticity curvature of the deviatoric plane first sextant.

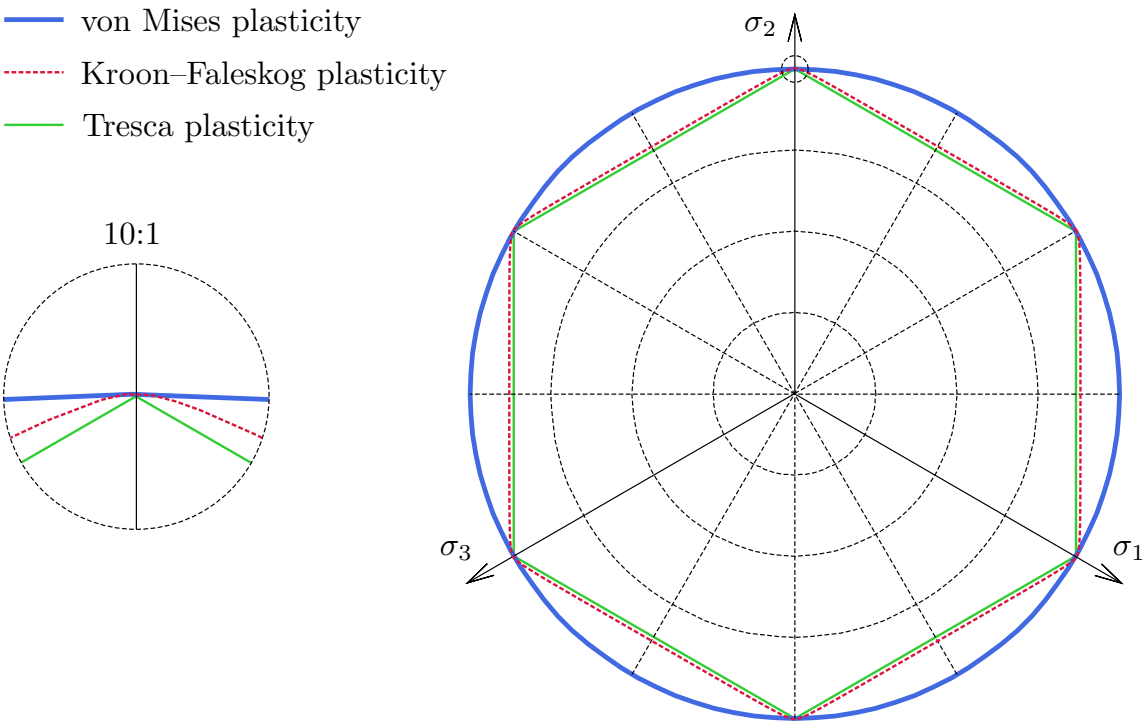

Figure 9.2: Initial yield loci at π plane for AA 2024-T351.

The additive strain decomposition was used for finite deformation kinematics. It can be written in the rate form as

$$\dot{\boldsymbol{\epsilon}} = \dot{\boldsymbol{\epsilon}}^e + \dot{\boldsymbol{\epsilon}}^p, \tag{9.9}$$

where $\boldsymbol{\epsilon}$ is the true strain tensor and $\boldsymbol{\epsilon}^e$ is the elastic strain tensor. Then, the Cauchy stress tensor can be obtained as

$$\boldsymbol{\sigma} = \boldsymbol{\mathcal{D}} : \boldsymbol{\epsilon}^e = \boldsymbol{\mathcal{D}} : (\boldsymbol{\epsilon} - \boldsymbol{\epsilon}^p), \tag{9.10}$$

where $\boldsymbol{\mathcal{D}}$ is the elastic stiffness tensor.

Saint-Venant [3] suggested that principal axes of strain increment are coincident with axes of principal stresses. Lévy [4] proposed general relationship between the stress and strain increment which was independently developed also by von Mises [8] as

$$\dot{\boldsymbol{\epsilon}} = \dot{\lambda}\mathbf{S}, \tag{9.11}$$

where λ is the plastic multiplier. Unfortunately, these equations are applicable only to material in which elastic strains are zero. Prandtl [12] made extension of Lévy–Mises equations for plane problems which was carried to complete generality by Reuss [14] as[20]

$$\dot{\boldsymbol{\epsilon}}^p = \dot{\lambda}\mathbf{S}. \tag{9.12}$$

When *the associative flow rule* or *the normality rule* is adopted, the yield function is equal to flow potential. Then, following the method of Lagrange gives

$$\dot{\boldsymbol{\epsilon}}^p = \dot{\lambda}\frac{\partial \Phi}{\partial \boldsymbol{\sigma}}, \tag{9.13}$$

where the plastic multiplier (or Lagrange multiplier) is determined on the basis of *consistency condition*[21] $\dot{\Phi} = 0$. The loading/unloading conditions defining plastic loading and elastic unloading, also known as *complementary conditions*, may be written in Kuhn–Tucker [21] form as follows

$$\Phi \leq 0,\ \dot{\lambda} \geq 0,\ \dot{\lambda}\Phi = 0. \tag{9.14}$$

The direction of plastic flow is given by an outer normal to the yield surface as

$$\tilde{\mathbf{n}} = \frac{\partial \Phi}{\partial \boldsymbol{\sigma}} = \frac{3}{2}\frac{\mathbf{S}}{\bar{\sigma}} - 3\frac{\frac{\mathrm{d}k}{\mathrm{d}\xi}}{k}\left(2\frac{3}{2}\frac{\mathbf{S}}{\bar{\sigma}} \cdot \frac{3}{2}\frac{\mathbf{S}}{\bar{\sigma}} - \mathbf{I} - \xi\frac{3}{2}\frac{\mathbf{S}}{\bar{\sigma}}\right), \tag{9.15}$$

which naturally ensures that the stress increment is normal to the yield surface (Figure 9.3a). The differential term in previous equation is following

$$\frac{\mathrm{d}k}{\mathrm{d}\xi} = 2\gamma\frac{\left(1+\omega_0^{-a}\right)^p \omega_0^{-a}}{\left(\omega^{-a}+\omega_0^{-a}\right)^{a+1}}\xi. \tag{9.16}$$

[20] Those are also known as Prandtl–Reuss equations.

[21] Also known as Prager's consistency condition.

The loading and unloading criteria are using consistency condition summarized in Table 9.2 [75, 80]. This is also graphically interpreted in Figure 9.3a [75, 80].

Table 9.2: The loading and unloading criteria [75, 80].

Yield condition	Stress increment	State
$\Phi < 0$		Initial elastic loading or unloading
$\Phi = 0$	$\tilde{\mathbf{n}} : \mathrm{d}\boldsymbol{\sigma} < 0$	Elastic unloading after previous yielding
$\Phi = 0$	$\tilde{\mathbf{n}} : \mathrm{d}\boldsymbol{\sigma} = 0$	Neutral loading
$\Phi = 0$	$\tilde{\mathbf{n}} : \mathrm{d}\boldsymbol{\sigma} > 0$	Plastic loading
$\Phi > 0$		Inadmissible

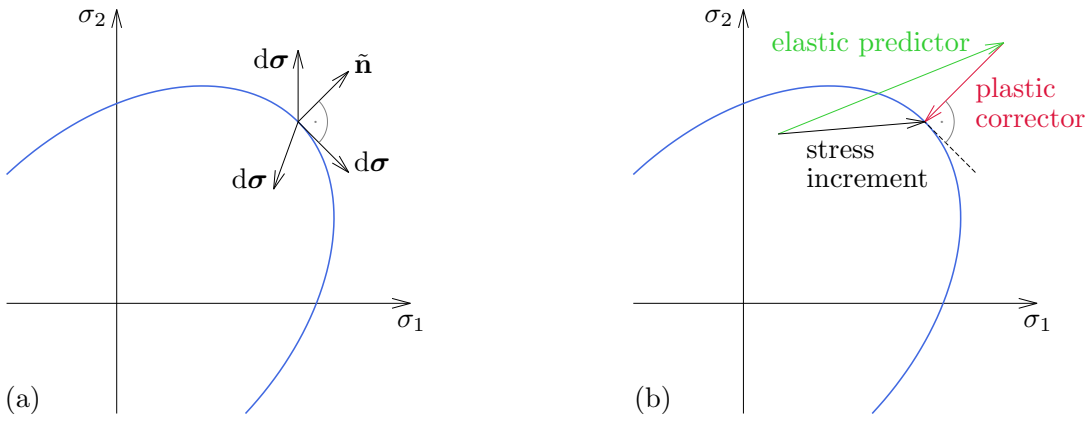

Figure 9.3: The yield surface with schematically illustrated: (a) neutral and plastic loading and elastic unloading [75, 80]; (b) radial return mapping algorithm [177].

Finally, the plastic multiplier of the J_2 and J_3 dependent plasticity is

$$\dot{\lambda} = \frac{\sqrt{\frac{2}{3}\dot{\boldsymbol{\epsilon}}^p : \dot{\boldsymbol{\epsilon}}^p}}{\sqrt{1 + 9\omega \left(\frac{\frac{\mathrm{d}k}{\mathrm{d}\xi}}{k} \right)^2}}. \tag{9.17}$$

It simplifies to J_2 theory in case of axisymmetry ($\omega = 0$) and generalized shear ($\omega = 1$) because the denominator of Equation 9.17 goes to unity in such cases.

The time integration procedure was used together with radial return mapping, which satisfies the Drucker's postulate (Figure 9.3b) [177], realized according to algorithm described in [120] and implemented in Abaqus time integration scheme using VUMAT.

Simulations of all fracture tests had to be done in order to gain state variables needed in the fracture model calibration. These simulations described in the following sections were done by using the explicit code without any influence of the damage accumulation or the material weakening. That is why the weakening effect was set up to affect the properties only in the point close to fracture, so the conditions were similar to the uncoupled approach.

9.1 Simulation of tension of smooth cylindrical specimen

Simulation of the tensile test was performed the same as in Chapters 6 and 8. There is force–displacement response from computation compared to experiment in Figure 9.4a. The von Mises plasticity did not differ in comparison to Kroon–Faleskog one as expected.

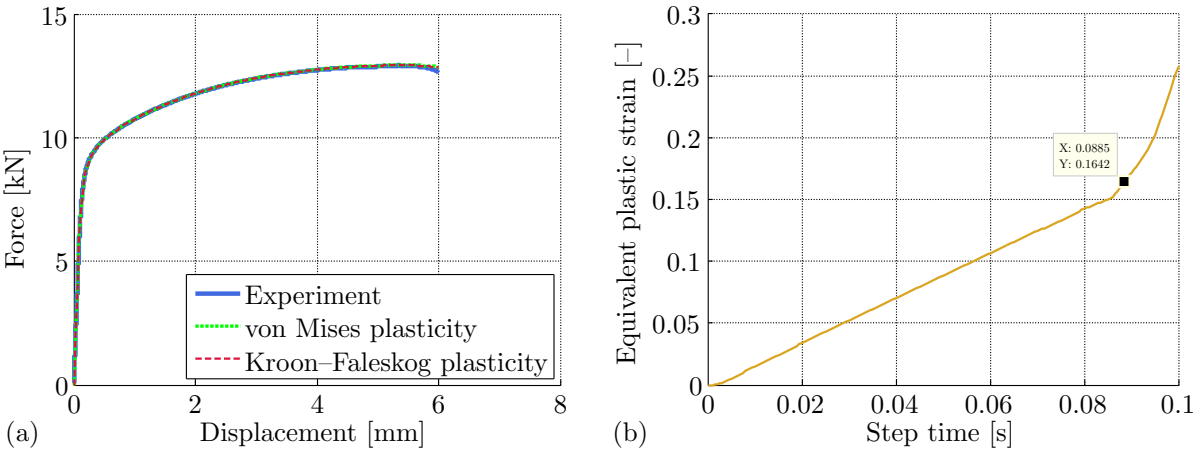

Figure 9.4: Tension of smooth specimen: (a) force–displacement responses of different plasticities compared to experiment; (b) evolution of the equivalent plastic strain.

Rapid growth of equivalent plastic strain rate is evident after the necking (Figure 9.4b), which was minor in case of smooth specimen. Because of this gradient, results are not reliable therefore the specimen was omitted from the ductile fracture calibration.

9.2 Simulations of tension of notched cylindrical specimens

All simulations were replicated in the same way as in Chapters 6 and 8, using CAX4R 4-node bilinear axisymmetric quadrilateral elements with characteristic size of 0.075 mm, reduced integration and hourglass control. Boundary conditions were also analogical.

Experimentally obtained force–displacement responses are compared to computationally obtained ones in Figure 9.5a for both von Mises and Kroon–Faleskog plasticities. It can be clearly seen that there is almost no difference between two used plasticities, as the normalized third invariants of the deviatoric stress tensor keep close to unity representing the axisymmetric stress state on axes of specimens and due to formulation of Kroon–Faleskog plasticity.

The loci for obtaining state variables were at axes in the notch region where the cracks initiated. These variables were chosen to be stress triaxiality and normalized third invariant of deviatoric stress tensor (Figure 9.5b). Hereinafter, history of those variables are not given for von Mises plasticity but for Kroon–Faleskog one only.

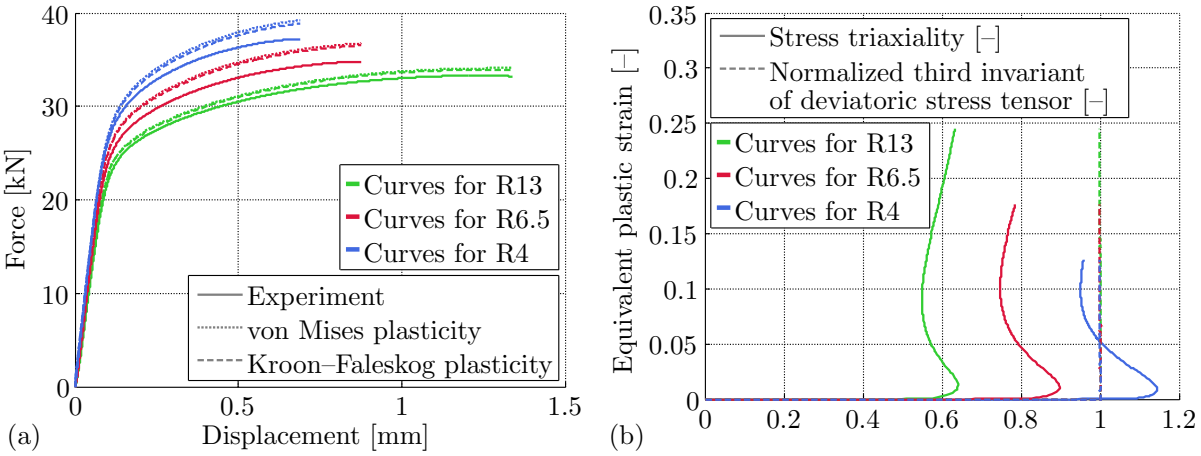

Figure 9.5: Tensile notched cylindrical specimens: (a) force–displacement responses from experiments and simulations; (b) evolution of stress triaxialities and normalized Lode angles during loading obtained by using Kroon–Faleskog plasticity.

It is obvious that introducing the pressure dependence into the plasticity would lead to improvement in force–displacement responses of tensile notched cylindrical specimens. It would also improve the responses of plane strain tests while the Lode dependence would have to be modified as well. On the other hand, it would definitely worsen the force–displacement response of upsetting test in this particular case because this plasticity assumes the same behaviour in tension and compression.

9.3 Simulation of tension of notched tubular specimen

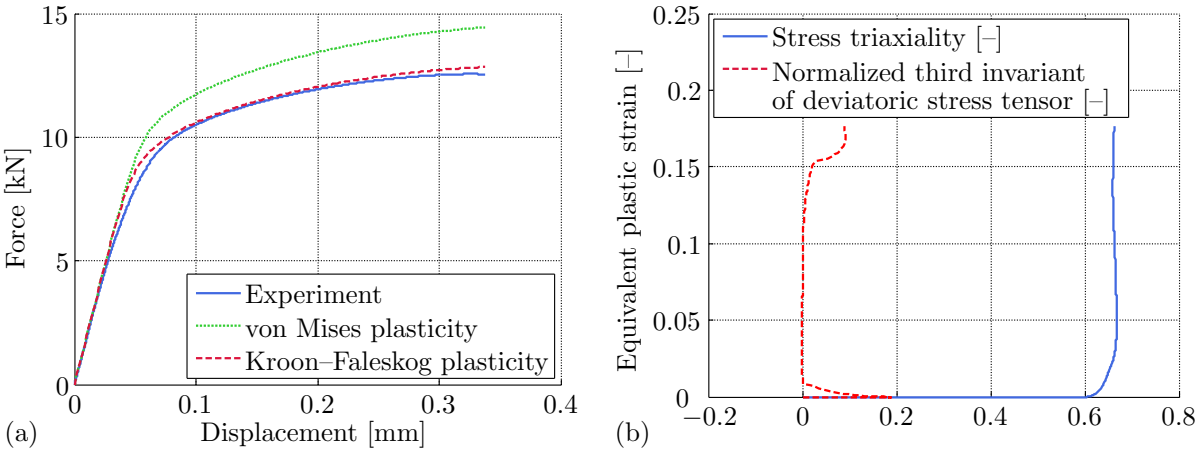

Figure 9.6: Results for tensile notched tubular specimen: (a) force–displacement responses from simulations and experiment; (b) evolution of stress triaxiality and normalized Lode angle during loading obtained by using Kroon–Faleskog plasticity.

This simulation was performed basically the same as in previous cases of notched cylindrical specimens. The axisymmetric geometry was modelled as the half of specimen with through hole. At first, this is the worse case scenario than the part with full solid body and secondly, a fewer number of elements saved computational time.

Force–displacement responses from computations and experiment are compared in Figure 9.6a.

The locus for obtaining state variables (Figure 9.6b) was approximately in the middle of the wall thickness at the notch region. It was found exactly as a locus where normalized Lode angle was close to zero and the stress triaxiality was maximal. The crack was expected to initiate there, because there is a loss of ductility with increasing stress triaxiality [35, 41] and also when moving from axial symmetry to plane strain [111, 184]. This is consistent with results of tension tests of other tubular specimens in literature [208, 221].

9.4 Simulation of torsion test

This is the only case when the computational models were not same for the simulations concerning von Mises and Kroon–Faleskog plasticities. An axisymmetric case with twist was used in implicit code, while a three dimensional model was used in case of explicit.

The axisymmetric model including twist for simulation concerning von Mises plasticity led to huge time saving. It was meshed with a 4-node generalized bilinear axisymmetric quadrilateral CGAX4R elements with reduced integration, hourglass control, twist and size of 0.075 mm.

The three dimensional model was discretized with C3D8R 8-node linear brick elements with reduced integration and hourglass control. These had characteristic size of 0.075 mm in the region of the notch and 0.2 mm in the upper tubular part.

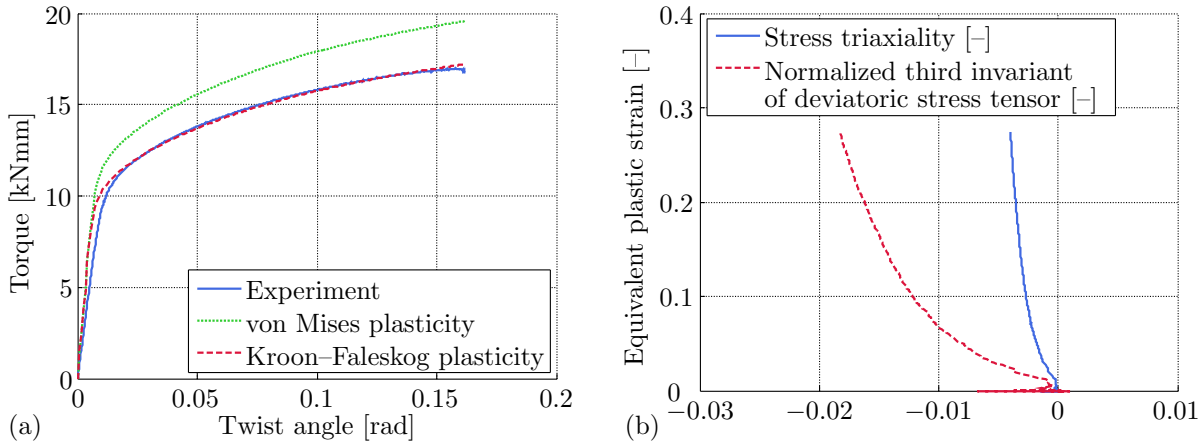

Figure 9.7: Results for torsional notched tubular specimen: (a) torque–twist angle responses from simulations and experiment; (b) evolution of stress triaxiality and normalized Lode angle during loading obtained by using Kroon–Faleskog plasticity.

The geometry was modelled as the half with through hole for the same reasons as in previous case regarding tension of notched tubular specimen. The height of the model was only 5 mm because no extensometer was employed. Additionally, the specimen was designed so as the whole straining took place only in the region of the notch. Therefore, there was no need to model larger section of the upper part which also saved some computational time, especially in the case of three dimensional model. The twist was introduced through the reference point on the axis to which the degrees of freedom regarding the twist of upper surface were coupled. The axial displacement and twist of bottom surface were constrained.

Semi-automatic mass scaling was deployed to target time increment of $1 \cdot 10^{-7}$ s to save computational time. The time increment for most critical elements was approximately $2.7 \cdot 10^{-9}$ s when the mass scaling was not accounted for. The kinetic energy was compared to the internal one in order to ensure there were negligible dynamic effects.

The torque–twist angle responses from simulations compared to experimental observation are depicted in Figure 9.7a showing very good conformity. It is obvious that the stiffness of measuring system played the role. On the other hand, it is supposed that it did not influence results much, considering there were other undetected uncertainties.

The locus for obtaining state variables (Figure 9.7b) was naturally on the outer surface in the smallest cross-section of the notch. Note the scale of horizontal axis which suggests that the loading was almost perfectly proportional.

9.5 Simulation of upsetting test

The simulation of upsetting test was performed as an axisymmetric case, again. Specimen was discretized using CAX4R 4-node bilinear axisymmetric quadrilateral 0.075 mm sized elements with reduced integration and hourglass control. Punches with 8 mm radii, of which the size did not represent a reality, were meshed with 0.075 mm RAX2 2-node linear axisymmetric rigid links.

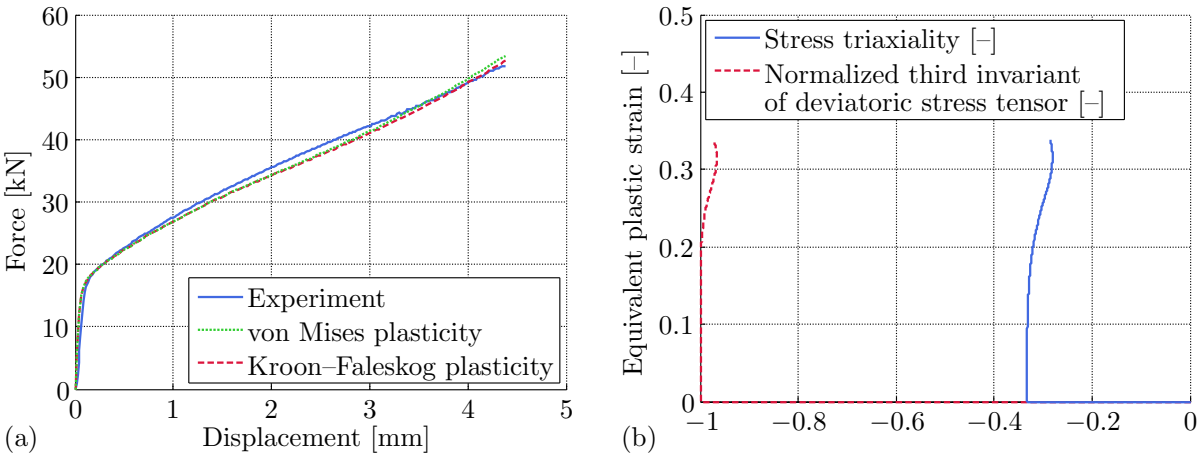

Figure 9.8: Upsetting test: (a) force–displacement curves from experiment and simulations; (b) loading paths given by stress triaxiality and normalized Lode angle.

The friction coefficient between punches and specimen was identified as 0.05 by trial and error method until the deformations (bulging or barrelling and visible stick and slip regions on upper and bottom surfaces) from simulation matched the experiments. The force–displacement curves from simulation and experiment are depicted in Figure 9.8a. Similarly as in axisymmetric tension, the Kroon–Faleskog plasticity deviated negligibly from von Mises yield criterion.

Stress triaxiality and normalized Lode angle (Figure 9.8b) were obtained from the surface node in the middle of cylinder height. The loading paths show approximate proportionality corresponding to small amount of friction.

It should be noted that there is some amount of uncertainty compared to tension or torsion tests, because of determining the friction conditions. This is a problem of all punching techniques like the small punch test [102, 117], cupping test similar to Erichsen test [241], Nakazima test[22] [204] or Hašek test [159, 205]. But still, it provided a valuable contribution to the performed experimental program.

[22] Also spelled as Nakajima test.

10 Ductile fracture criterion

The essential part of ductile fracture model is its fracture envelope defined by weighting function of damage. Besides the fracture strain, stress triaxiality and normalized third invariant of deviatoric stress tensor are inputs into the ductile fracture calibration. There are two possible calibration techniques. The first one, which was used in the present thesis, lies in the averaging of two latter mentioned state variables [146, 151]. The averaging is based on adopted damage rule. With respect to Equation 8.3, it leads to

$$\eta_{av} = \frac{q_1}{\hat{\epsilon}^f} \int_0^{\hat{\epsilon}^f} \eta \, \mathrm{d}\bar{\epsilon}^p + \frac{q_2(1-q_1)}{\hat{\epsilon}^f} \int_0^{\hat{\epsilon}^f} \eta \left(\frac{\bar{\epsilon}^p}{\hat{\epsilon}^f} \right)^{q_2-1} \mathrm{d}\bar{\epsilon}^p, \tag{10.1}$$

$$\xi_{av} = \frac{q_1}{\hat{\epsilon}^f} \int_0^{\hat{\epsilon}^f} \xi \, \mathrm{d}\bar{\epsilon}^p + \frac{q_2(1-q_1)}{\hat{\epsilon}^f} \int_0^{\hat{\epsilon}^f} \xi \left(\frac{\bar{\epsilon}^p}{\hat{\epsilon}^f} \right)^{q_2-1} \mathrm{d}\bar{\epsilon}^p. \tag{10.2}$$

Generally, the weighting function of damage $\bar{\epsilon}^f(\eta, \xi)$ has a certain number of material constants which may be represented by matrix of material constants $\mathbf{G}$. Then, it is fitted to discrete points $\hat{\epsilon}^f(\eta_{av}, \xi_{av})$ by minimizing following target function

$$\min_{\mathbf{G}} \sum_{i=1}^{M} \left[\hat{\epsilon}_i^f(\eta_{av}, \xi_{av}) - \bar{\epsilon}^f(\eta_{av}, \xi_{av}) \right]^2, \tag{10.3}$$

where i is a number of particular fracture test and M is number of all fracture tests. The disadvantage due to averaging arises when the loading is considerably nonproportional. That is why there was such an effort to keep experiments as close to proportional loading as possible. The above approach might be improved by weighting individual deviations by particular fracture strains [135].

Another approach to ductile fracture calibration defines the minimum of target function as a damage integrated up to fracture of each test averaged over all tests [153, 209]

$$\min_{\mathbf{G}} \sum_{i=1}^{M} (1 - D_{s,i})^2. \tag{10.4}$$

The advantage is in eliminating the preliminary averaging. On the other hand, calibration costs are higher than in previous approach and there is also higher global minimum uncertainty. Therefore, it is suitable to use it, for example, for final fine tuning of material constants.

There are summarized fracture strains from simulations realized in previous chapter in Table 10.1 according to numbering in Table 5.2, together with state variables, stress triaxiality and normalized third invariant of deviatoric stress tensor, averaged according to Equations 10.1 and 10.2. The averaging was done by trapezoidal numerical integration by using `trapz` function within MATLAB. Thus, there are 6 points for calibration available, which is the minimum demanded by sixth parametric criterion, as described further. It might be noted that all tension, torsion and compression experiments correspond to those obtained in [98, 111] with minor deviations.

Table 10.1: Fracture strains and averaged state variables from numerical simulations.

Fracture test number	Fracture strain [–]	Average stress triaxiality [–]	Average normalized third invariant of deviatoric stress tensor [–]
2	0.2452	0.6019	1.0000
3	0.1761	0.7812	0.9997
4	0.1259	0.9852	0.9993
5	0.1767	0.6607	0.0396
6	0.2743	−0.0033	−0.0149
7	0.3378	−0.3026	−0.9829

The fracture envelope is certainly a crucial part of each fracture criterion. The damage accumulation and material weakening related constants have been already determined but these cannot be used in the fracture envelope calibration because they are coupled with the fracture model, which is yet to be determined. A similar approach was presented by Erice and Gálvez [214]. The whole procedure may be realized through neural network as well, when all the constants would be calibrated together [189], but it is not considered in the present study because of time consumption, as previously stated. So the fracture model calibration procedure is kept as simple as possible.

The KHPS2 (Kubík Hůlka Petruška Šebek 2) criterion [224], rising from KHPS (Kubík Hůlka Petruška Šebek) criterion [224], was chosen on the basis of good approximation ability, which is partly at the expense of material constants amount, and presence of cut-off in reasonable level. The asymmetric weighting function of damage with respect to normalized third invariant of deviatoric stress tensor can be written as follows

$$\bar{\epsilon}^f(\eta,\xi) = \left[\frac{1}{2}\left(\frac{G_4}{\langle\eta+g\rangle}+\frac{G_5}{\langle\eta+g\rangle}\right)-\frac{G_6}{\langle\eta+g\rangle}\right]\xi^2 + \frac{1}{2}\left(\frac{G_4}{\langle\eta+g\rangle}-\frac{G_5}{\langle\eta+g\rangle}\right)\xi+\frac{G_6}{\langle\eta+g\rangle}, \tag{10.5}$$

where $G_1,\ldots,G_6$ are six material constants and g is a parabolic function governing the cut-off beyond which the damage is not accumulated. It reads

$$g(\xi) = \left(G_3+\frac{G_1-G_3}{2}-G_2\right)\xi^2+\frac{G_1-G_3}{2}\xi+G_2. \tag{10.6}$$

First three constants are additive inverses of cut-off plane distances in stress triaxialities, particularly G_1 at $\xi = 1$, G_2 at $\xi = 0$ and G_3 at $\xi = -1$. Latter three constants have to be positive and influence the loci of focuses of equi-axed hyperbolas, particularly G_4 at $\xi = 1$, G_5 at $\xi = -1$ and G_6 at $\xi = 0$. The semi-axis lengths of hyperbolas are quadratic functions of normalized third invariant of deviatoric stress tensor.

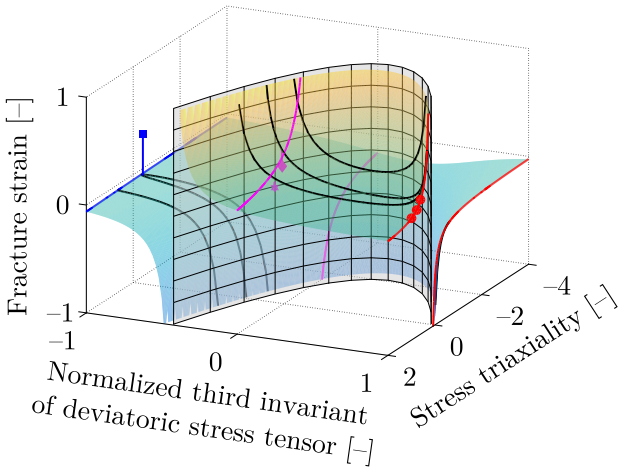

Figure 10.1: Wrongly calibrated fracture envelope of KHPS2 to fracture tests.

The criterion calibration was realized by MATLAB script. The `createOptimProblem` was used to create an optimization problem structure, including initial guess of material constants, their lower and upper boundaries to ensure the proper ranges and `fmincon` to find the minimum of constrained nonlinear multivariable target function defined within `nonlcon`. There were two types of constraints applied to cut-off. One ensures that the cut-off lies in stress triaxiality behind each experiment, so that the fracture envelope is fitted in the proper range of fracture strains, using

$$g_i = \left(G_3 + \frac{G_1 - G_3}{2} - G_2\right)\xi_{av,i}^2 + \frac{G_1 - G_3}{2}\xi_{av,i} + G_2, \tag{10.7}$$

while the following condition $-g_i - \eta_{av,i} > 0$ should apply. Without this constraint, some of experiments might be fitted wrongly to the second part of hyperbolic criterion which lies in negative fracture strains and which is physically unrealistic[23]. The situation is illustrated in Figure 10.1 where the approximation is ordinary overall, but the shape of fracture envelope is inadmissible[24].

[23] Analogical problem might arise also in case of Extended Mohr–Coulomb criterion [156], for instance. On the other hand, it is not often because the criterion is defined by goniometric functions which do not exhibit sharp curvatures in shape of fracture envelope which also results in presence of cut-off region in unrealistic levels.

[24] Similar problem might arise in case of complex phenomenological criteria without cut-off as well, like the one proposed by Bai and Wierzbicki [135]. The fracture tests are not fitted directly to negative fracture strains. The negative fracture strains can occur within remote areas from experimental data due to high number of material constants and therefore high shape flexibility. Unfortunately, this phenomenon cannot be solved by the above mentioned constraints.

The second constraint ensures the convexity of cut-off plane by using curvature in Cartesian coordinates as

$$\bar{\kappa} = \frac{\frac{\mathrm{d}^2 g}{\mathrm{d}\xi^2}}{\left(1 + \left(\frac{\mathrm{d}g}{\mathrm{d}\xi}\right)^2\right)^{\frac{3}{2}}}, \tag{10.8}$$

which must be positive. The derivatives of the cut-off with respect to normalized third invariant of deviatoric stress tensor are, respectively,

$$\frac{\mathrm{d}g}{\mathrm{d}\xi} = (G_1 - 2G_2 + G_3)\xi + \frac{G_1 - G_3}{2}, \tag{10.9}$$

$$\frac{\mathrm{d}^2 g}{\mathrm{d}\xi^2} = G_1 - 2G_2 + G_3. \tag{10.10}$$

Then, `run` method from `GlobalSearch` class was used for finding the global minimum according to Equation 10.3.

The final set of calibrated constants is given in Table 10.2. Calibrated fracture envelope with its cut-off plane is depicted in Figure 10.2a where the red line corresponds to axisymmetric tension condition, the magenta line to plane strain or generalized shear, the blue line to axisymmetric compression, the black line to plane stress, the red circles to tensions of notched cylindrical specimens, the magenta diamond to torsion test, the magenta hexagram to tension of notched tubular specimen and the blue square to compression.

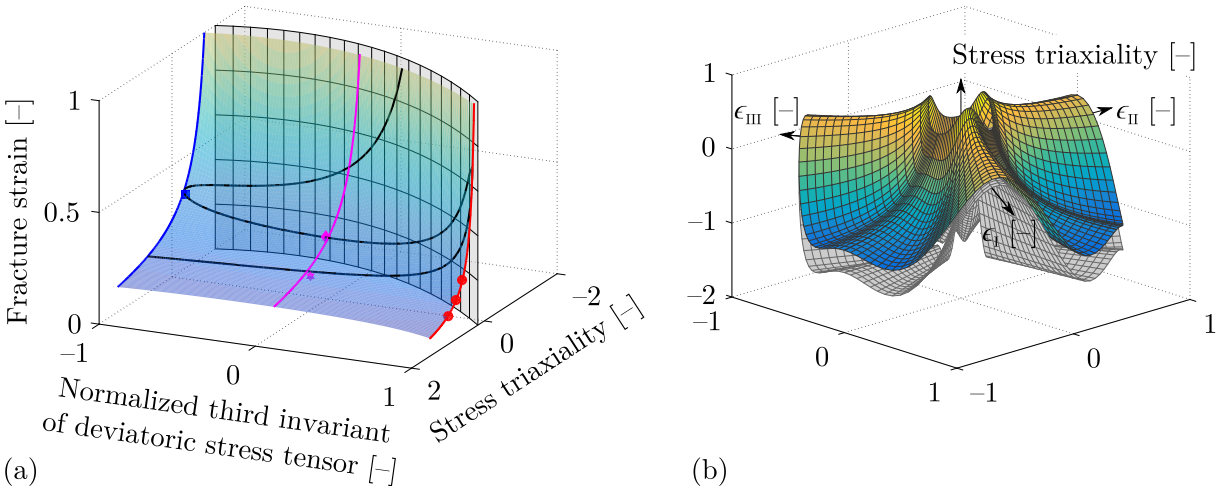

Figure 10.2: Calibrated fracture envelope of KHPS2 criterion in the space of: (a) fracture strain and state variables; (b) principal plastic strains and stress triaxiality.

There are also vertical lines connecting the fracture strains from experiment (computationally obtained) and fracture envelope in Figure 10.2a, graphically interpreting the least square errors. Unfortunately, those cannot be seen because the errors were very small.

The envelope is also depicted in the space of principal plastic strains ($\epsilon_{\mathrm{I}}, \epsilon_{\mathrm{II}}, \epsilon_{\mathrm{III}}$) and stress triaxiality, from which it can be easily transformed to stress space and may represent a limit state analogically to the yield surface (Figure 10.2b).

Table 10.2: Calibrated material constants of KHPS2 criterion for AA 2024-T351.

G_1 [–]	G_2 [–]	G_3 [–]	G_4 [–]	G_5 [–]	G_6 [–]
−0.178	1.195	1.189	0.104	0.301	0.327

It is obvious that there is significant Lode dependence from plane strain towards the axisymmetric tension, while there is almost none towards the axisymmetric compression (Figure 10.3a). One might see that the position of cut-off at plane strain is similar to one at axisymmetric compression in negative stress triaxiality, while it slightly exceeds the zero at axisymmetric tension condition. The convex curvature of cut-off can be seen in Figure 10.3b.

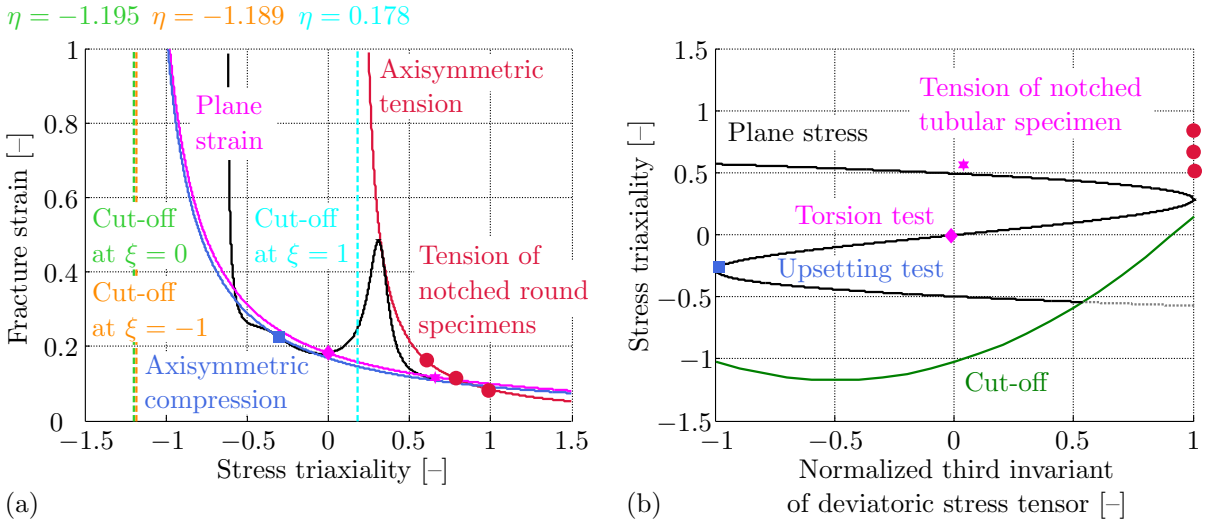

Figure 10.3: Calibrated KHPS2 in space of: (a) fracture strain against stress triaxiality; (b) stress triaxiality against normalized third invariant of deviatoric stress tensor.

There are listed errors calculated as deviations between calibrated fracture envelope and fracture strains from experiments (obtained computationally in the previous chapter) in Table 10.3 according to numbering in Table 5.2. Those are directly related to vertical lines, mentioned in one of previous paragraphs. The percentage errors can be estimated as

$$\varepsilon_i = 100 \frac{|\hat{\epsilon}_i^f(\eta_{av}, \xi_{av}) - \bar{\epsilon}_i^f(\eta_{av}, \xi_{av})|}{\hat{\epsilon}_i^f(\eta_{av}, \xi_{av})}. \tag{10.11}$$

Generally, the maximum error was 2.4 %, so there was very good approximation of experiments by the KHPS2 criterion. The average error stood approximatelly at 0.9 %.

Table 10.3: Errors of calibrated KHPS2 criterion with respect to experiments.

Test number	2	3	4	5	6	7
Error [%]	0.1	2.1	2.4	0.0	0.4	0.1

Bai and Wierzbicki [228] conducted the same error analysis for several different fracture criteria with 15 fracture tests carried out on AA 2024-T351 and the average error ranged between 14 to 43 %, excluding the result for Cockroft and Latham with only one material constant and poor approximation ability. Apart from the stress based analysis, Lou et al. [212] did the strain based analysis of the presented model with 18 experiments[25] on aluminium alloy 2024-T351 and compared it to similar phenomenological criteria. The average error was 21 % for the proposed model and 21, 19 and 19 % for reference criteria. The strain based error analysis, as in [228], seems to be more reasonable than the one based on fracture stress as in [175] because of the nature and resolution regarding the ductile fracture (Figure 1.1).

[25] It should be noted that the authors combined experiments executed by various researches. Although on the same aluminium alloy but there might be changes in microstructure.

11 Application and verification of proposed approach

The developed approach was applied to conducted fracture tests to show the prediction ability and reliability. It is always good to verify what has been calibrated and it should not be otherwise in the case of ductile fracture models. Three tests have been chosen, one of each specific stress state, the axisymmetric tension of notched cylindrical specimen, plane strain tension of notched tubular specimen and axisymmetric compression of cylinder. Attention was paid to overall description of the fracture in force–displacement responses as well as in prediction of crack initiation locus and its propagation.

11.1 Fracture at axisymmetric tension

The tensile test of notched cylindrical specimen with R13 notch radius should be closest to the one of smooth cylindrical specimen, towards which the whole approach was basically calibrated. Therefore, it should exhibit very good match with experimental observation.

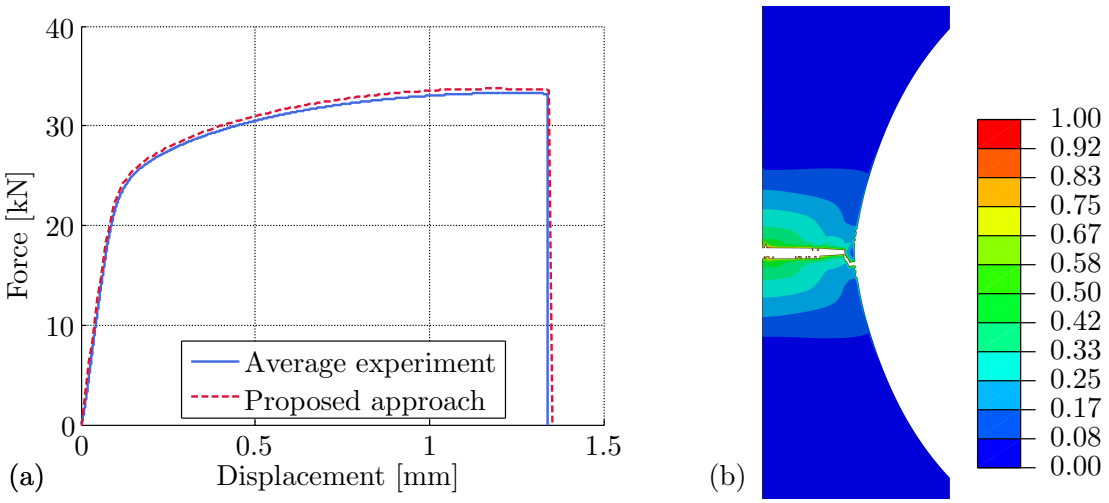

Figure 11.1: Tensile test of notched cylindrical specimen with R13 notch: (a) particular force–displacement responses; (b) field of damage parameter after the separation.

The simulation was replicated in the same way as in Section 9.2 with the difference that the specimen was not modelled as axisymmetric half, but as axisymmetric whole, so the crack propagation could be performed without being influenced by boundary conditions.

There is a force–displacement response from computation compared to experimental one in Figure 11.1a with an excellent match, as expected.

The crack initiated on the axis and propagated horizontally at first. It was followed by the slant fracture in a final stage (Figure 11.1b). The fracture surface was also swept to be compared with experiment in detail. Round specimens did not show perfect cup and cone fracture but still, there was apparent slant fracture in the final stage which is in good correspondence with computation (Figure 11.2).

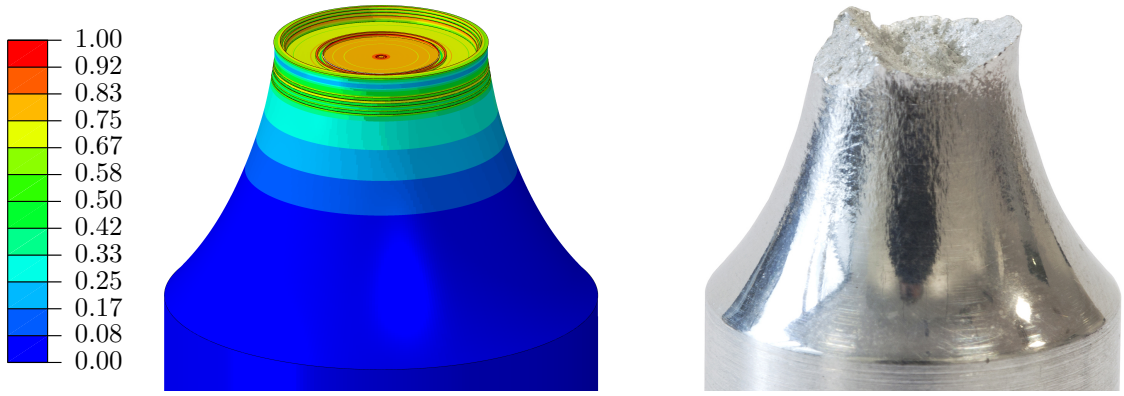

Figure 11.2: Field of damage parameter of one half of notched cylindrical specimen with R13 notch radius and one half of post-mortem specimen after the tensile test.

11.2 Fracture at plane strain tension

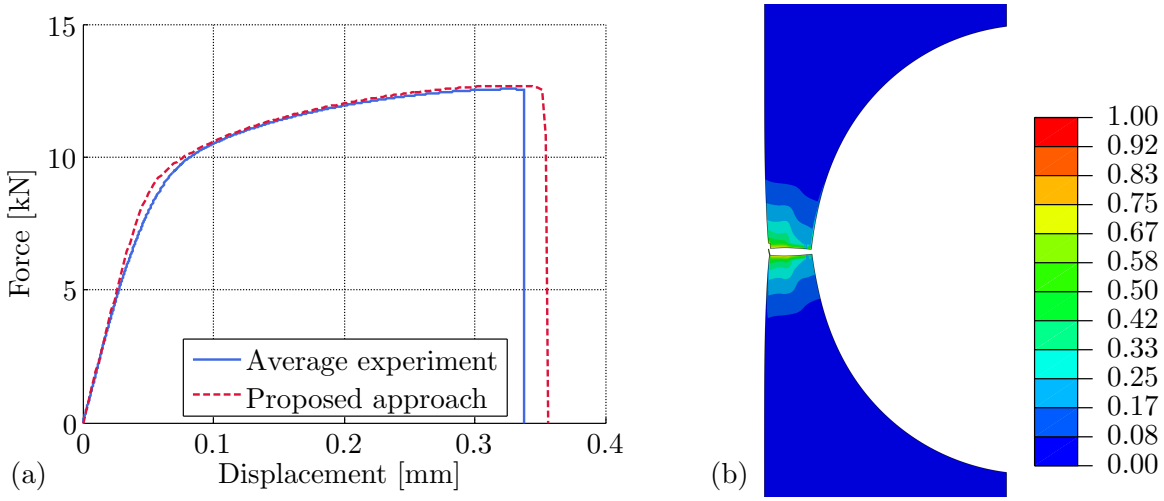

Figure 11.3: Tensile test of notched tubular specimen: (a) particular force–displacement responses; (b) field of damage parameter after the specimen separation.

The tension at plane strain should have produced the slant fracture as in the case of the notched tube.

The simulation was replicated in the same way as in Section 9.3. The only difference was modelling the whole axisymmetric specimen, in order to not influence the fracture by boundary conditions.

There are force–displacement reposes from computation and experiment which are very close due to employing the Lode dependent plasticity. Only the final fracture was slightly over predicted as shown in Figure 11.3a.

The crack initiated approximately in the middle of the specimen thickness at the notch region as assumed already in Section 9.3 during obtaining state variables for calibration procedure. Then, it propagated horizontally, which is unfortunately in contradiction with experiments.

11.3 Fracture at axisymmetric compression

In the end, the upsetting test was investigated.

The simulation was replicated as in Section 9.5 but in three dimensional space. The cylinder was discretized by mapped mesh with 8-node linear bricks C3D8R with reduced integration, hourglass control and characteristic length size of 0.075 mm. The punches were meshed with R3D4 bilinear rigid quadrilateral 4-node three dimensional elements with the same size as the cylinder. The semi-automatic mass scaling was also deployed to target time increment of $1 \cdot 10^{-7}$ s while the time increment for most critical elements were approximately $3.35 \cdot 10^{-9}$ s without accounting for mass scaling. The kinetic energy was, again, checked with respect to internal one to ensure negligible dynamic effects.

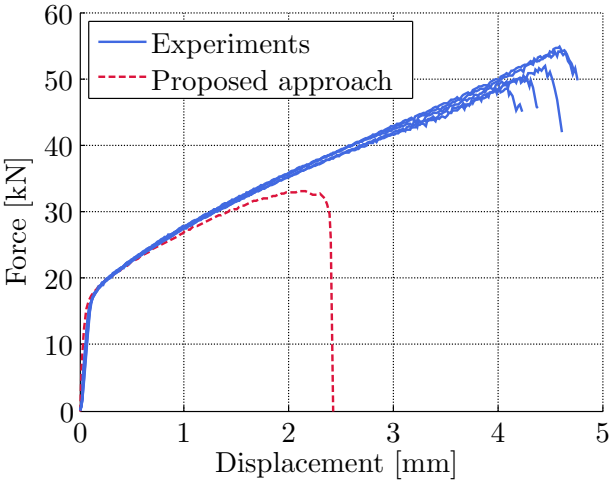

Figure 11.4: Responses of compressed cylinders from simulation and experiments.

There are force–displacement responses from experiments compared to computation in Figure 11.4. The simulation grossly underestimated the reality, because the initiation was in the centre of the specimen, whereas the equivalent plastic strain was much higher than the one on the outer surface (0.7 compared to 0.2) from which the fracture model was calibrated.

Xue [149] also reported that there was higher equivalent plastic strain in the centre of the compressed cylinder but the crack did not initiate there. Instead, it initiated in the corners of the specimen and propagated diagonally to the centre. Such behaviour was also observed experimentally [120]. Despite these facts, the fracture model was conventionally calibrated from the outer surface in the middle of the specimen height as in [98]. It is not possible to extract state variables from the specimen corners which come into contact with punches and where the results are distorted. On the other hand, the proposed model was able to perform a slant fracture as in experiment at least (Figure 11.5).

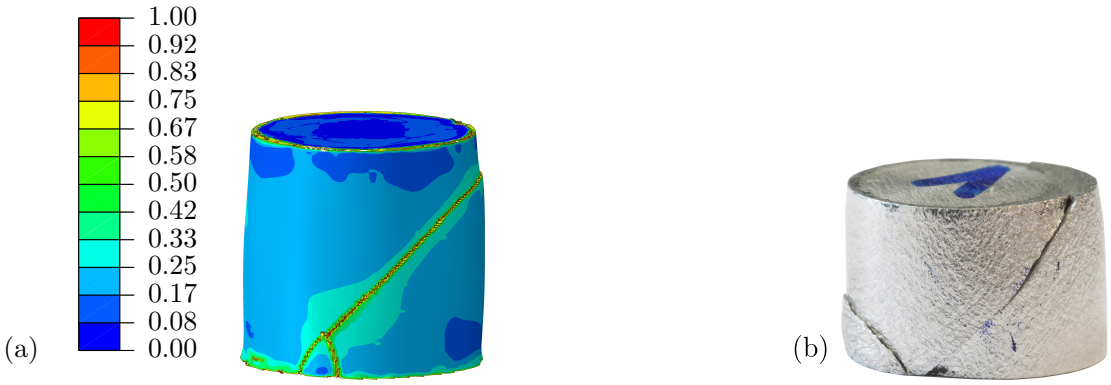

Figure 11.5: Cracked cylindrical specimen after the upsetting test: (a) with field of damage parameter obtained from numerical simulation; (b) experimentally performed.

The upsetting test has been still widely used for ductile fracture calibration [119, 186, 235], while not many authors provide information about the locus used for obtaining the state variables needed in calibration. In conclusion, the specimen is not convenient for the calibration because of problems with obtaining relevant data from the computation.

There are circumstances under which the crack, if any, initiates from the outer surface. Those correspond to compression of very ductile metals or with dry friction conditions yielding in high barrelling, which results in nonnegligible tensile circumferential stresses on the outer surface of cylinder [191, 236]. Then, the crack might even be vertical. In any event, such cases are tried to be omitted within the calibration of ductile fracture because of high nonproportionality of the loading.

Finally, it can be also seen how localized the damage parameter was (Figure 11.5). A similar situation was, of course, in previous cases as well.

12 Conclusions and future studies

The present thesis dealt with ductile fracture criteria intended for multiaxial loading and related theory, with extensive experimental testing to support the background and assumptions of proposed approach, developed respecting extensive literature survey as well. This approach balances between the coupled and uncoupled criteria trying to pick the best of both. It is based on the calibration technique of uncoupled phenomenological models which is easy to conduct. A solution to problems is documented with fitting the hyperbolic criterion, which may be applied to similar models based either on the same definition or on combination of goniometric functions. Significance of the plasticity role was also demonstrated and the implemented complex yield criterion better described the material behaviour observed in form of experimentally measured responses to loading. The importance of continuum damage mechanics approach was also reported. Nevertheless, it leads to some difficulties which have had to be solved.

12.1 Conclusions

The approach was outlined after the careful study of literature. The damage accumulation could be studied by using stepwise experimenting. Unfortunately, it was revealed that this was not reliable to prove the nonlinear damage accumulation due to high sensitivity on input parameters. Therefore, an alternative way in the form of cyclic loading, loading/unloading more precisely, was carried out. Sequentially, the double damage curve approach and material weakening related constants were estimated. After calibrating the Kroon–Faleskog plasticity and KHPS2 phenomenological ductile fracture criterion which were coupled via the including of the softening effect, the proposed methodology was applied to existing fracture tests in order to verify them. The overall experimental program counted the tension of smooth and notched cylindrical and notched tubular specimens, torsion of notched tubular specimen and compression of cylinder.

First of all, implementing of the Lode dependent plasticity led to some discrepancies in plane strain tension of plates, associated with nonnegligible change of stress state. This was mentioned only marginally and should be subjected to further investigation.

Another problem had arisen in compression testing. It was revealed that the upsetting test of simple cylinder is not suitable for calibration of ductile fracture criteria. It is due to questionable locus of crack initiation which is complicated by the presence of friction. It is obvious that the point representing the compression in space of $(\bar{\varepsilon}^f, \eta, \xi)$ is not correct.

It is supported by the location of tensile tests of cylindrical specimens suggesting that the curve corresponding to $\xi = -1$ should have been positioned towards higher fracture strains. Then, the fracture envelope would have formed a more curved shape. Moreover, it would be convenient to have two experiments on axisymmetric compression condition at least, even though it is difficult to conduct this reliably.

The approach seems to be promising, but it should be validated by conducting a broader experimental campaign with more extensive computing, of course.

Finally, it can be concluded that all the outlined goals were fulfilled.

12.2 Future studies

The obtained results imply the connection between monotonic and cyclic loading. The ultra low cycle fatigue poses together with monotonic loading the space for further study. There is certainly a smooth transition between these two phenomena. There is definitely potential in finding a unified approach to those problems, but even if the extension to or coupling with fatigue might be challenging, it has still seemed to be long term.

The damage accumulation also needs further investigation. This might be realized by using techniques such as the X-ray microtomography and there is a room for ultrasound or DIC measurement as well.

Negative stress triaxialities and cut-off region are worthy of future studies. It is connected with better description of conditions in compression. This might be comprised by the upsetting of notched cylinder as in Figure 12.1a, cylinder with specific recess (Figure 12.1b) or other shapes of cylinder as in literature [105, 162, 166]. Then, there would be more evident locus of ductile fracture initiation. Moreover, more appropriate stress state and loading history might be reached. Another alternative to describe the condition at $\xi = -1$ is in a biaxial tension of a cross-like specimen as in Figure 12.1c.

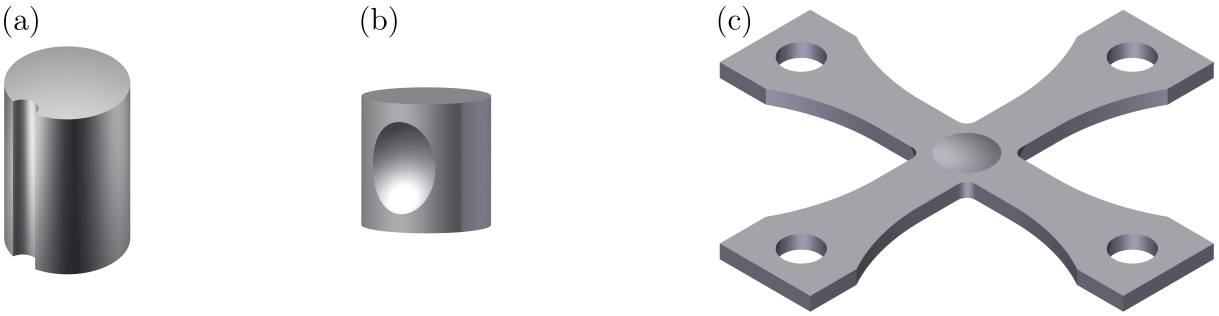

Figure 12.1: The illustration of: (a) notched cylindrical specimen [87]; (b) cylindrical specimen with a spherical recess [239]; (c) biaxially loaded cruciform specimen [218].

The probabilistic approach to ductile fracture seems to be very interesting in accounting for the deviation in identified strains to fracture [238, 240].

Accounting for reversal loading, precompression, pretension or pretorsion, which seem to play nonnegligible role in ductile fracture [100, 229, 232], might be considered as well.

References

[1] Coulomb C. A. Essai sur une application des règles *de maximis & minimis* à quelquels problèmes de statique, relatifs à l'architecture. *Mémoires présentés à l'Académie des Sciences*, 1776, pp. 343–384 (in French).

[2] Tresca M. H. Mémoire sur l'écoulement des corps solides soumis à de fortes pressions. *Compte Rendu des Séances de l'Académie des Sciences*, 1864, pp. 754–758 (in French).

[3] Saint-Venant de B. Sur l'établissement des équations des mouvements intérieurs opérés dans les corps solides ductiles au delà des limite où l'élasticité pourrauit les ramener à leur premier état. *Compte Rendu des Séances de l'Académie des Sciences*, 1870, pp. 473–480 (in French).

[4] Lévy M. Mémoire sur les équations générales des mouvements intérieurs des corps solides ductiles au delà des limites où l'élasticité pourrait les ramener à leur premier état. *Compte Rendu des Séances de l'Académie des Sciences*, 1870, pp. 1323–1325 (in French).

[5] Bauschinger J. Ueber die Veränderung der Elasticitätsgrenze und des Elasticitätsmoduls verschiedener Metalle. *Civilingenieur*, 1881, Vol. XXVII, No. 19, pp. 289–340 (in German).

[6] Mohr O. Welche Umstände bedingen die Elastizitätsgrenze und den Bruch eines Materiales? *Zeitschrift des Vereins deutscher Ingenieure*, 1900, Nr. 45, pp. 1524–1530 (in German).

[7] Huber M. T. Właściwa praca odkształcenia jako miara wytężenia materiału. *Towarzystwo Politechniczne*, 1904, Vol. 22, 38–81 (in Polish).

[8] Mises von R. Mechanik der festen Körpern im plastisch-deformablen Zustand. *Nachrichten von der Königlichen Gesellschaft der Wissenschaften zu Göttingen, Mathematisch-physikalische Klasse*, 1913, pp. 582–592 (in German).

[9] Hencky H. Zur Theorie plastischer Deformationen und der hierdurch im Material hervorgerufenen Nachspannungen. *Zeitschrift für angewandte Mathematik und Mechanik*, 1924, Vol. 4, Issue 4, pp. 323–334 (in German).

[10] Palmgren A. Die Lebensdauer von Kugellagern. *Zeitschrift des Vereins Deutscher Ingenieure*, 1924, Vol. 68, No. 14, pp. 339–341 (in German).

[11] Portevin A., LeChatelier F. Heat treatment of aluminum-copper alloys. *Transaction of American Society for Steel Treating*, 1924, pp. 457–478.

[12] Prandtl von L. Spannungsverteilung in plastischen Körpern. In *Proceedings of the 1st International Congress on Applied Mechanics*, Delft, 1924, pp. 43–54 (in German).

[13] Lode von W. Versuche über den Einflußder mittleren Hauptspannung auf die Fließgrenze. *Zeitschrift für Angewandte Mathematik und Mechanik*, 1925, Vol. 5, Issue 2, pp. 142–144 (in German).

[14] Reuss von A. Berücksichtigung der elastischen Formänderung in der Plastizitätstheorie. *Zeitschrift für Angewandte Mathematik und Mechanik*, 1930, Vol. 10, Issue 2, pp. 266–274 (in German).

[15] Hollomon J. H. Tensile deformation. *Metals Technology*, 1945, pp. 268–290.

[16] Ramberg W., Osgood W. R. *Description of stress–strain curves by three parameters.* National Advisory Committee for Aeronautics, Technical Note No. 902, 1943.

[17] Miner M. A. Cumulative damage in fatigue. *Journal of Applied Mechanics*, 1945, pp. A-159–A-164.

[18] Voce E. The relationship between stress and strain for homogeneous deformations. *Journal of the Institute of Metals*, 1948, pp. 537–562.

[19] Drucker D. C. Some implications of work hardening and ideal plasticity. *Quarterly of Applied Mathematics*, 1950, Vol. VII, No. 4, pp. 411–418.

[20] Freudenthal A. M. *The inelastic behavior of engineering materials and structures.* John Wiley & Sons, New York, 1950.

[21] Kuhn H. W., Tucker A. W. Nonlinear programming. In *Proceedings of the Second Berkeley Symposium on Mathematical Statistics and Probability*, University of California Press, Berkeley, California, 1951, pp. 481–492.

[22] Drucker D. C. A more fundamental approach to plastic stress-strain relations. In *Proceedings of the 1st U.S. National Congress on Applied Mechanics*, Chicago, 1951, pp. 487–491.

[23] Drucker D. C., Prager W. Soil mechanics and plastic analysis or limit design. *Quarterly Journal of Mechanics & Applied Mathematics*, 1952, Vol. X, No. 2, pp. 157–165.

[24] Swift H. W. Plastic instability under plane stress. *Journal of the Mechanics and Physics of Solids*, 1952, Vol. 1, Issue 1, pp. 1–18.

[25] Manson S. S. *Behavior of materials under conditions of thermal stress.* Report 1170, National Advisory Committee for Aeronautics, 1954, pp. 317–350.

[26] Coffin L. F. A study of the effects of cyclic thermal stresses on a ductile metal. *Transactions of the ASME*, 1954, pp. 931–950.

[27] Marco S. M., Starkey W. L. A concept of fatigue damage. *Transactions of the ASME*, 1954, pp. 627–632.

[28] Kachanov L. M. Rupture time under creep conditions. *Izvestia Akademii Nauk SSSR, Otdelenie Tekhnicheskich Nauk*, 1958, No. 8, pp. 26–31 (in Russian).

[29] Barenblatt G. I. The formation of equilibrium cracks during brittle fracture. General ideas and hypotheses. Axially-symmetric cracks. *Journal of Applied Mathematics and Mechanics*, 1959, Vol. 23, No. 3, pp. 622–636.

[30] Drucker D. C. A definition of stable inelastic material. *Journal of Applied Mechanics*, 1959, pp. 101–106.

[31] Coffin L. F., Tavernelli J. F. The cyclic straining and fatigue of metals. *Transactions of the Metallurgical Society of AIME*, 1959, Vol. 215, pp. 794–807.

[32] Dugdale D. S. Yielding of steel sheets containing slits. *Journal of the Mechanics and Physics of Solids*, 1960, Vol. 8, pp. 100–104.

[33] Keeler S. P., Backofen W. A. Plastic instability and fracture in sheets stretched over rigid punches. *Transactions of the ASM*, 1963, Vol. 56, pp. 25–48.

[34] Rabotnov Y. N. On the equations of state for creep. *Progress in Applied Mechanics*, 1963, the Prager Anniversary Volume, pp. 307–315.

[35] Bridgman P. W. *Studies in large plastic flow and fracture: With special emphasis on the effects of hydrostatic pressure.* Harvard University Press, Cambridge, Massachusetts, 1964.

[36] Morrow J. D. Cyclic plastic strain energy and fatigue of metals. In *Symposium on Internal Friction, Damping, and Cyclic Plasticity Phenomena in Materials*, Chicago, Illinois, 1965, pp. 45–87.

[37] Manson S. S. Interfaces between fatigue, creep, and fracture. *International Journal of Fracture Mechanics*, 1966, Vol. 2, Issue 1, pp. 327–363.

[38] Cockcroft M. G., Latham D. J. Ductility and the workability of metals. *Journal of the Institute of Metals*, 1968, Vol. 96, pp. 33–39.

[39] Goodwin G. M. Application of strain analysis to sheet metal forming problems in the press shop. *SAE Technical Paper 680093*, 1968.

[40] McClintock F. A. A criterion for ductile fracture by the growth of holes. *Journal of Applied Mechanics*, 1968, Vol. 35, No. 2, pp. 363–371.

[41] Rice J. R., Tracey D. M. On the ductile enlargement of voids in triaxial stress fields. *Journal of the Mechanics and Physics of Solids*, 1969, Vol. 17, Issue 3, pp. 201–217.

[42] Clausing D. P. Effect of plastic strain state on ductility and toughness. *International Journal of Fracture Mechanics*, 1970, Vol. 6, Issue 1, pp. 71–85.

[43] Date E. H. F., Atkins M., Beaton G. V. Measurement of the elasticity and ultrasound velocities of steel. *Ultrasonics*, 1971, Vol. 9, Issue 4, pp. 209–214.

[44] Brozzo P., Deluca B., Rendina R. A new method for the prediction of formability limits in metal sheets. In *Proceedings of the 7th Biennial Conference of the International Deep Drawing Research Group*, Amsterdam, Netherlands, 1972.

[45] Hosford W. F. A generalized isotropic yield criterion. *Journal of Applied Mechanics*, 1972, pp. 607–609.

[46] Oyane M. Criteria of ductile fracture strain. *Bulletin of the Japan Society of Mechanical Engineers*, 1972, Vol. 15, No. 90, pp. 1507–1513.

[47] Gurson A. L. *Plastic flow and fracture behavior of ductile materials incorporating void nucleation, growth, and interaction.* Ph.D. Thesis, Brown University, 1975.

[48] Gurson A. L. *Continuum theory of ductile rupture by void nucleation and growth: Part I - Yield criteria and flow rules for porous ductile media.* Technical Report No. 39, Divission of Engineering, Brown University, 1975.

[49] Hancock J. W., Mackenzie A. C. On the mechanisms of ductile failure in high-strength steels subjected to multi-axial stress-states. *Journal of the Mechanics and Physics of Solids*, 1976, Vol. 24, Issues 2–3, pp. 147–160.

[50] Gurson A. L. Continuum theory of ductile rupture by void nucleation and growth: Part I—Yield criteria and flow rules for porous ductile media. *Journal of Engineering Materials and Technology*, 1977, Vol. 99, No. 1, pp. 2–15.

[51] Gingold R. A., Monaghan J. J. Smoothed particle hydrodynamics: Theory and application to non-spherical stars. *Monthly Notices of the Royal Astronomical Society*, 1977, Vol. 181, pp. 375–389.

[52] Arcan M., Hashin Z., Voloshin A. A method to produce uniform plane-stress states with applications to fiber-reinforced materials. *Experimental Mechanics*, 1978, Vol. 18, Issue 4, pp. 141–146.

[53] Oh S. I., Chen C. C., Kobayashi S. Ductile fracture in axisymmetric extrusion and drawing: Part 2—Workability in extrusion and drawing. *Journal of Engineering for Industry*, 1979, Vol. 101, No. 1, pp. 36–44.

[54] Wilkins M. L., Streit R. D., Reaugh J. E. *Cumulative-strain-damage model of ductile fracture: Simulation and prediction of engineering fracture tests.* Technical Report UCRL-53058, Lawrence Livermore National Laboratory, California, 1980.

[55] Lindholm U. S., Nagy A., Johnson G. R., Hoegfeldt J. M. Large strain, high strain rate testing of copper. *Journal of Engineering Materials and Technology*, 1980, Vol. 102, No. 4, pp. 376–381.

[56] Owen D. R. J., Hinton E. *Finite elements in plasticity: Theory and practise.* Pineridge Press Limited, Swansea, United Kingdom, 1980, ISBN: 0-906674-05-2.

[57] Tvergaard V. Influence of voids on shear band instabilities under plane strain conditions. *International Journal of Fracture*, 1981, Vol. 17, No. 4, pp. 389–407.

[58] Le Roy G., Embury J. D., Edward G., Ashby M. F. A model of ductile fracture based on the nucleation and growth of voids. *Acta Metallurgica*, 1981, Vol. 29, Issue 8, pp. 1509–1522.

[59] Lancaster P., Salkauskas K. Surfaces generated by moving least squares methods. *Mathematics of Computation*, 1981, Vol. 37, No. 155, pp. 141–157.

[60] Tvergaard V. On localization in ductile materials containing spherical voids. *International Journal of Fracture*, 1982, Vol. 18, No. 4, pp. 237–252.

[61] Osgood C. C. *Fatigue design.* Pergamon Press, Exeter, 1982, ISBN: 0-08-026167-1.

[62] Johnson G. R., Cook W. H. A constitutive model and data for metals subjected to large strains, high strain rates and high temperatures. In *Proceedings of the 7th International Symposium on Ballistics*, The Hague, Netherlands, 1983, pp. 541–547.

[63] Hancock J. W., Brown D. K. On the role of strain and stress state in ductile failure. *Journal of Mechanics and Physics of Solids*, 1983, Vol. 31, No. 1, pp. 1–24.

[64] Tvergaard V., Needleman A. Analysis of the cup-cone fracture in a round tensile bar. *Acta Metallurgica*, 1984, Vol. 32, No. 1, pp. 157–169.

[65] Lemaitre J. Coupled elasto-plasticity and damage constitutive equations. *Computer Methods in Applied Mechanics and Engineering*, 1985, Vol. 51, pp. 31–49.

[66] Lemaitre J. A continuous damage mechanics model for ductile fracture. *Journal of Engineering Materials and Technology*, 1985, Vol. 107, No. 1, pp. 83–89.

[67] Manson S. S., Halford G. R. *Re-examination of cumulative fatigue damage analysis—An engineering perspective.* NASA Technical Memorandum 87325, 1985.

[68] Johnson G. R., Cook W. H. Fracture characteristics of three metals subjected to various strains, strain rates, temperatures and pressures. *Engineering Fracture Mechanics*, 1985, Vol. 21, No. 1, pp. 31–48.

[69] Marini B., Mudry F., Pineau A. Ductile rupture of A508 steel under nonradial loading. *Engineering Fracture Mechanics*, 1985, Vol. 22, No. 3, pp. 375–386.

[70] Pijaudier-Cabot G., Bažant Z. Nonlocal damage theory. *Journal of Engineering Mechanics*, 1987, Vol. 113, Issue 10, pp. 1512–1533.

[71] Chaboche J.-L. Continuum damage mechanics: Part I—General concepts. *Journal of Applied Mechanics*, 1988, Vol. 55, No. 1, pp. 59–64.

[72] Chaboche J.-L. Continuum damage mechanics: Part II—Damage growth, crack initiation, and crack growth. *Journal of Applied Mechanics*, 1988, Vol. 55, No. 1, pp. 65–72.

[73] Clift S. E., Hartley P., Sturgess C. E. N., Rowe G. W. Fracture prediction in plastic deformation processes. *International Journal of Mechanical Sciences*, 1990, Vol. 32, No. 1, pp. 1–17.

[74] Tai W. H. Plastic damage and ductile fracture in mild steels. *Engineering Fracture Mechanics*, 1990, Vol. 37, No. 4, pp. 853–880.

[75] Bittnar Z., Šejnoha J. *Numerical methods of mechanics 1.* Czech Technical University in Prague, Prague, 1992, ISBN: 80-01-00855-X.

[76] Xu X.-P., Needleman A. Numerical simulations of fast crack growth in brittle solids. *Journal of the Mechanics and Physics of Solids*, 1994, Vol. 42, No. 9, pp. 1397–1434.

[77] Zhang Z. L. On the accuracies of numerical integration algorithms for Gurson-based pressure-dependent elastoplastic constitutive models. *Computer Methods in Applied Mechanics and Engineering*, 1995, Vol. 121, Issues 1–4, pp. 15–28.

[78] Fischer F. D., Kolednik O., Shan G. X., Rammerstorfer F. G. A note on calibration of ductile failure damage indicators. *International Journal of Fracture*, 1995, Vol. 73, Issue 4, pp. 345–357.

[79] Belytschko T., Organ D., Krongauz Y. A coupled finite element–element-free Galerkin method. *Computational Mechanics*, 1995, Vol. 17, Issue 3, pp. 186–195.

[80] Khan A. S., Huang S. *Continuum theory of plasticity.* John Wiley & Sons, New York, 1995, ISBN: 0-471-31043-3.

[81] Atkins A. G. Fracture in forming. *Journal of Materials Processing Technology*, 1996, Vol. 56, Issues 1–4, pp. 609–618.

[82] Melenk J. M., Babuška I. The partition of unity finite element method: Basic theory and applications. *Computer Methods in Applied Mechanics and Engineering*, 1996, Vol. 139, Issues 1–4, pp. 289–314.

[83] Camacho G. T., Ortiz M. Adaptive Lagrangian modelling of ballistic penetration of metallic targets. *Computer Methods in Applied Mechanics and Engineering*, 1997, Vol. 142, Issues 3–4, pp. 269–301.

[84] Bonora N. A nonlinear CDM model for ductile failure. *Engineering Fracture Mechanics*, 1997, Vol. 58, No. 1/2, pp. 11–28.

[85] Stefanov Y. P., Makarov P. V., Burkov P. V., Matveev V. S. Dynamic simulation of chip generation and formation in metal cutting. *Theoretical and Applied Fracture Mechanics*, 1997, Vol. 28, Issue 2, pp. 117–124.

[86] Fatemi A., Yang L. Cumulative fatigue damage and life prediction theories: A survey of the state of the art for homogeneous materials. *International Journal of Fatigue*, 1998, Vol. 20, No. 1, pp. 9–34.

[87] Petruška J., Janíček L. Computationally-experimental workability determination of compressed cylindrical specimen with surface defect. *Journal of Materials Processing Technology*, 1998, Vols. 80–81, pp. 572–578.

[88] Bleck W., Deng Z., Papamantellos K., Gusek Ch. O. A comparative study of the forming-limit diagram models for sheet steels. *Journal of Materials Processing Technology*, 1998, Vol. 83, Issues 1–3, pp. 223–230.

[89] Bonora N., Newaz G. M. Low cycle fatigue life estimation for ductile metals using a nonlinear continuum damage mechanics model. *International Journal of Solids and Structures*, 1998, Vol. 35, No. 16, pp. 1881–1894.

[90] Rennie D. The present state of medical journals. *The Lancet*, 1998, Vol. 352, Supplement 2, pp. S18–S22.

[91] Jirásek M. Nonlocal models for damage and fracture: Comparison of approaches. *International Journal of Solids and Structures*, 1998, Vol. 35, Nos. 31–32, pp. 4133–4145.

[92] Belytschko T., Black T. Elastic crack growth in finite elements with minimal remeshing. *International Journal for Numerical Methods in Engineering*, 1999, Vol. 45, Issue 5, pp. 601–620.

[93] Brünig M., Berger S., Obrecht H. Numerical simulation of the localization behavior of hydrostatic-stress-sensitive metals. *International Journal of Mechanical Sciences*, 2000, Vol. 42, Issue 11, pp. 2147–2166.

[94] Børvik T., Hopperstad O. S., Berstad T., Langseth M. A computational model of viscoplasticity and ductile damage for impact and penetration. *European Journal of Mechanics - A/Solids*, 2001, Vol. 20, Issue 5, pp. 685–712.

[95] François M. A plasticity model with yield surface distortion for non proportional loading. *International Journal of Plasticity*, 2001, Vol. 17, Issue 5, pp. 703–717.

[96] Urban J. *Crushing and fracture of lightweight structures.* Ph.D. Thesis, Technical University of Denmark, 2003, ISBN: 87-89502-70-1.

[97] Törnqvist R. *Design of crashworthy ship structures.* Ph.D. Thesis, Technical University of Denmark, 2003, ISBN: 87-89502-74-4.

[98] Bao Y. *Prediction of ductile crack formation in uncracked bodies.* Ph.D. Thesis, Massachusetts Institute of Technology, 2003.

[99] Hooputra H., Gese H., Dell H., Werner H. A comprehensive failure model for crashworthiness simulation of aluminium extrusions. *International Journal of Crashworthiness*, 2004, Vol. 9, No. 5, pp. 449–463.

[100] Bao Y., Treitler R. Ductile crack formation on notched Al2024-T351 bars under compression–tension loading. *Materials Science and Engineering: A*, 2004, Vol. 384, Issues 1–2, pp. 385–394.

[101] Bao Y., Wierzbicki T. A comparative study on various ductile crack formation criteria. *Journal of Engineering Materials and Technology*, 2004, Vol. 126, Issue 3, pp. 314–324.

[102] Campitelli E. N., Spätig P., Bonadé R., Hoffelner W., Victoria M. Assessment of the constitutive properties from small ball punch test: Experiment and modeling. *Journal of Nuclear Materials*, 2004, Vol. 335, Issue 3, pp. 366–378.

[103] Teng X., Wierzbicki T. Effect of fracture criteria on high velocity perforation of thin beams. *International Journal of Computational Methods*, 2004, Vol. 1, No. 1, pp. 171–200.

[104] Gilmour K. R., Leacock A. G., Ashbridge M. T. J. The influence of plastic strain ratios on the numerical modelling of stretch forming. *Journal of Materials Processing Technology*, 2004, Vol. 152, Issue 1, pp. 116–125.

[105] Bao Y., Wierzbicki T. On fracture locus in the equivalent strain and stress triaxiality space. *International Journal of Mechanical Sciences*, 2004, Vol. 46, Issue 1, pp. 81–98.

[106] Mirone G. A new model for the elastoplastic characterization and the stress–strain determination on the necking section of a tensile specimen. *International Journal of Solids and Structures*, 2004, Vol. 41, Issue 13, pp. 3545–3564.

[107] Suresh S. *Fatigue of materials.* Cambridge University Press, New York, 2004, ISBN: 978-0-521-57046-6.

[108] Bandstra J. P., Koss D. A. A simulation of growth and coalescence of voids during ductile fracture. *Materials Science and Engineering: A*, 2004, Vols. 387–389, pp. 399–403.

[109] Bao Y., Wierzbicki T. On the cut-off value of negative triaxiality for fracture. *Engineering Fracture Mechanics*, 2005, Vol. 72, Issue 7, pp. 1049–1069.

[110] Anderson T. L. *Fracture mechanics: Fundamentals and applications.* Taylor & Francis Group, Boca Raton, 2005, ISBN: 978-0-84931-656-2.

[111] Wierzbicki T., Bao Y., Lee Y.-W., Bai Y. Calibration and evaluation of seven fracture models. *International Journal of Mechanical Sciences*, 2005, Vol. 47, Issues 4–5, pp. 719–743.

[112] Teng X., Wierzbicki T. Transition of failure modes in round-nosed mass-to-beam impact. *European Journal of Mechanics - A/Solids*, 2005, Vol. 24, Issue 5, pp. 857–876.

[113] Wierzbicki T., Bao Y., Bai Y. A new experimental technique for constructing a fracture envelope of metals under multi-axial loading. In *Proceedings of the 2005 SEM Annual Conference & Exposition on Experimental and Applied Mechanics*, Portland, Oregon, 2005, pp. 1295–1303.

[114] Komori K. Ductile fracture criteria for simulating shear by node separation method. *Theoretical and Applied Fracture Mechanics*, 2005, Vol. 43, Issue 1, pp. 101–114.

[115] Bao Y. Dependence of ductile crack formation in tensile tests on stress triaxiality, stress and strain ratios. *Engineering Fracture Mechanics*, 2005, Vol. 72, Issue 4, pp. 505–522.

[116] Saanouni K. Virtual metal forming including the ductile damage occurrence. *Journal of Materials Processing Technology*, 2006, Vol. 177, Issues 1–3, pp. 19–25.

[117] Abendroth M., Kuna M. Identification of ductile damage and fracture parameters from the small punch test using neural networks. *Engineering Fracture Mechanics*, 2006, Vol. 73, Issue 6, pp. 710–725.

[118] Teng X., Wierzbicki T. Evaluation of six fracture models in high velocity perforation. *Engineering Fracture Mechanics*, 2006, Vol. 73, Issue 12, pp. 1653–1678.

[119] Bai Y., Bao Y., Wierzbicki T. Fracture of prismatic aluminum tubes under reverse straining. *International Journal of Impact Engineering*, 2006, Vol. 32, Issue 5, pp. 671–701.

[120] Xue L. *Ductile fracture modeling - Theory, experimental investigation and numerical verification.* Ph.D. Thesis, Massachusetts Institute of Technology, 2007.

[121] Barsoum I., Faleskog J. Rupture mechanisms in combined tension and shear—Experiments. *International Journal of Solids and Structures*, 2007, Vol. 44, Issue 6, pp. 1768–1786.

[122] Barsoum I., Faleskog J. Rupture mechanisms in combined tension and shear—Micromechanics. *International Journal of Solids and Structures*, 2007, Vol. 44, Issue 17, pp. 5481–5498.

[123] Lassance D., Fabrègue D., Delannay F., Pardoen T. Micromechanics of room and high temperature fracture in 6xxx Al alloys. *Progress in Materials Science*, 2007, Vol. 52, Issue 1, pp. 62–129.

[124] Khan A. S., Kazmi R., Farrokh B. Multiaxial and non-proportional loading responses, anisotropy and modeling of Ti–6Al–4V titanium alloy over wide ranges of strain rates and temperatures. *International Journal of Plasticity*, 2007, Vol. 23, Issue 6, pp. 931–950.

[125] Mohr D., Henn S. Calibration of stress-triaxiality dependent crack formation criteria: A new hybrid experimental–numerical method. *Experimental Mechanics*, 2007, Vol. 47, Issue 6, pp. 805–820.

[126] Xue L. Damage accumulation and fracture initiation in uncracked ductile solids subject to triaxial loading. *International Journal of Solids and Structures*, 2007, Vol. 44, Issue 16, pp. 5163–5181.

[127] Celentano D. J., Chaboche J.-L. Experimental and numerical characterization of damage evolution in steels. *International Journal of Plasticity*, 2007, Vol. 23, pp. 1739–1762.

[128] Mae H., Teng X., Bai Y., Wierzbicki T. Calibration of ductile fracture properties of a cast aluminum alloy. *Materials Science and Engineering: A*, 2007, Vol. 459, Issues 1–2, pp. 156–166.

[129] Feigenbaum H. P., Dafalias Y. F. Directional distortional hardening in metal plasticity within thermodynamics. *International Journal of Solids and Structures*, 2007, Vol. 44, Issues 22–23, pp. 7526–7542.

[130] Saanouni K. On the numerical prediction of the ductile fracture in metal forming. *Engineering Fracture Mechanics*, 2008, Vol. 75, Issue 11, pp. 3545–3559.

[131] Soyarslan C. *Modelling damage for elastoplasticity.* Ph.D. Thesis, Middle East Technical University, 2008.

[132] Bai Y., Wierzbicki T. Forming severity concept for predicting sheet necking under complex loading histories. *International Journal of Mechanical Sciences*, 2008, Vol. 50, Issue 6, pp. 1012–1022.

[133] Bořkovec J. *Computer simulation of material separation process.* Ph.D. Thesis, Brno University of Technology, 2008 (in Czech).

[134] Xue L. A unified expression for low cycle fatigue and extremely low cycle fatigue and its implication for monotonic loading. *International Journal of Fatigue*, 2008, Vol. 30, Issues 10–11, pp. 1691–1698.

[135] Bai Y., Wierzbicki T. A new model of metal plasticity and fracture with pressure and Lode dependence. *International Journal of Plasticity*, 2008, Vol. 24, Issue 6, pp. 1071–1096.

[136] Düster A., Parvizian J., Yang Z., Rank E. The finite cell method for three-dimensional problems of solid mechanics. *Computer Methods in Applied Mechanics and Engineering*, 2008, Vol. 197, Issues 45–48, pp. 3768–3782.

[137] Steglich D., Brocks W., Heerens J., Pardoen T. Anisotropic ductile fracture of Al 2024 alloys. *Engineering Fracture Mechanics*, 2008, Vol. 75, Issue 12, pp. 3692–3706.

[138] Bai Y. *Effect of loading history on necking and fracture.* Ph.D. Thesis, Massachusetts Institute of Technology, 2008.

[139] Xue L. Constitutive modeling of void shearing effect in ductile fracture of porous materials. *Engineering Fracture Mechanics*, 2008, Vol. 75, Issue 11, pp. 3343–3366.

[140] Taiebat H. A., Carter J. P. Flow rule effects in the Tresca model. *Computers and Geotechnics*, 2008, Vol. 35, Issue 3, pp. 500–503.

[141] Nahshon K., Hutchinson J. W. Modification of the Gurson Model for shear failure. *European Journal of Mechanics - A/Solids*, 2008, Vol. 27, Issue 1, pp. 1–17.

[142] Hiermaier S. J. *Structures under crash and impact: Continuum mechanics, discretization and experimental characterization.* Springer, New York, 2008, ISBN: 978-0-387-73862-8.

[143] Teng X. Numerical prediction of slant fracture with continuum damage mechanics. *Engineering Fracture Mechanics*, 2008, Vol. 75, Issue 8, pp. 2020–2041.

[144] Huda Z., Taib N. I., Zaharinie T. Characterization of 2024-T3: An aerospace aluminum alloy. *Materials Chemistry and Physics*, 2009, Vol. 113, Issues 2–3, pp. 515–517.

[145] Gao X., Zhang T., Hayden M., Roe Ch. Effects of the stress state on plasticity and ductile failure of an aluminum 5083 alloy. *International Journal of Plasticity*, 2009, Vol. 25, Issue 12, pp. 2366–2382.

[146] Bai Y., Teng X., Wierzbicki T. On the application of stress triaxiality formula for plane strain fracture testing. *Journal of Engineering Materials and Technology*, 2009, Vol. 131, Issue 2, pp. 021002-1–021002-10.

[147] Marotti de Sciarra F. A nonlocal model with strain-based damage. *International Journal of Solids and Structures*, 2009, Vol. 46, Issues 22–23, pp. 4107–4122.

[148] Toribio J., Kharin V. Finite-deformation analysis of the crack-tip fields under cyclic loading. *International Journal of Solids and Structures*, 2009, Vol. 46, Issue 9, pp. 1937–1952.

[149] Xue L. Stress based fracture envelope for damage plastic solids. *Engineering Fracture Mechanics*, 2009, Vol. 76, Issue 3, pp. 419–438.

[150] Lee E. U., Vasudevan A. K., Glinka G. Environmental effects on low cycle fatigue of 2024-T351 and 7075-T651 aluminum alloys. *International Journal of Fatigue*, 2009, Vol. 31, Issues 11–12, pp. 1938–1942.

[151] Mohr D., Ebnoether F. Plasticity and fracture of martensitic boron steel under plane stress conditions. *International Journal of Solids and Structures*, 2009, Vol. 46, Issue 20, pp. 3535–3547.

[152] Beese A. M., Luo M., Li Y., Bai Y., Wierzbicki T. Partially coupled anisotropic fracture model for aluminum sheets. *Engineering Fracture Mechanics*, 2010, Vol. 77, Issue 7, pp. 1128–1152.

[153] Vaziri M. R., Salimi M., Mashayekhi M. A new calibration method for ductile fracture models as chip separation criteria in machining. *Simulation Modelling Practice and Theory*, 2010, Vol. 18, Issue 9, pp. 1286–1296.

[154] Mirone G., Corallo D. A local viewpoint for evaluating the influence of stress triaxiality and Lode angle on ductile failure and hardening. *International Journal of Plasticity*, 2010, Vol. 26, Issue 3, pp. 348–371.

[155] Ravindran S. *Prediction of material damage in orthotropic metals for virtual structural testing.* Ph.D. Thesis, Cranfield University, 2010.

[156] Bai Y., Wierzbicki T. Application of extended Mohr–Coulomb criterion to ductile fracture. *International Journal of Fracture*, 2010, Vol. 161, Issue 1, pp. 1–20.

[157] Li Y.,Wierzbicki T. Prediction of plane strain fracture of AHSS sheets with post-initiation softening. *International Journal of Solids and Structures*, 2010, Vol. 47, Issue 17, pp. 2316–2327.

[158] Dunand M., Mohr D. Hybrid experimental–numerical analysis of basic ductile fracture experiments for sheet metals. *International Journal of Solids and Structures*, 2010, Vol. 47, Issue 9, pp. 1130–1143.

[159] Luo M., Wierzbicki T. Numerical failure analysis of a stretch-bending test on dual-phase steel sheets using a phenomenological fracture model. *International Journal of Solids and Structures*, 2010, Vol. 47, Issues 22–23, pp. 3084–3102.

[160] Gao X., Zhang T., Zhou J., Graham S. M., Hayden M., Roe Ch. On stress-state dependent plasticity modeling: Significance of the hydrostatic stress, the third invariant of stress deviator and the non-associated flow rule. *International Journal of Plasticity*, 2011, Vol. 27, Issue 2, pp. 217–231.

[161] Dunand M., Mohr D. On the predictive capabilities of the shear modified Gurson and the modified Mohr–Coulomb fracture models over a wide range of stress triaxialities and Lode angles. *Journal of the Mechanics and Physics of Solids*, 2011, Vol. 59, Issue 7, pp. 1374–1394.

[162] Li H., Fu M. W., Lu J., Yang H. Ductile fracture: Experiments and computations. *International Journal of Plasticity*, 2011, Vol. 27, Issue 2, pp. 147–180.

[163] Basaran M. *Stress state dependent damage modeling with a focus on the Lode angle influence.* Ph.D. Thesis, Rheinisch-Westfälische Technische Hochschule Aachen, 2011.

[164] Kamaya M., Kawakubo M. A procedure for determining the true stress–strain curve over a large range of strains using digital image correlation and finite element analysis. *Mechanics of Materials*, 2011, Vol. 43, Issue 5, pp. 243–253.

[165] Seidenfuss M., Samal M. K., Roos E. On critical assessment of the use of local and nonlocal damage models for prediction of ductile crack growth and crack path in various loading and boundary conditions. *International Journal of Solids and Structures*, 2011, Vol. 48, Issue 24, pp. 3365–3381.

[166] Bouchard P.-O., Bourgeon L., Fayolle S., Mocellin K. An enhanced Lemaitre model formulation for materials processing damage computation. *International Journal of Material Forming*, 2011, Vol. 4, Issue 3, pp. 299–315.

[167] Chocron S., Erice B., Anderson Ch. E. A new plasticity and failure model for ballistic application. *International Journal of Impact Engineering*, 2011, Vol. 38, Issues 8–9, pp. 755–764.

[168] Kossa A. *Exact stress integration schemes for elastoplasticity* Ph.D. Thesis, Budapest University of Technology and Economics, 2011.

[169] Dunand M., Mohr D. Optimized butterfly specimen for the fracture testing of sheet materials under combined normal and shear loading. *Engineering Fracture Mechanics*, 2011, Vol. 78, Issue 17, pp. 2919–2934.

[170] Landron C., Maire E., Bouaziz O., Adrien J., Lecarme L., Bareggi A. Validation of void growth models using X-ray microtomography characterization of damage in dual phase steels. *Acta Materialia*, 2011, Vol. 59, Issue 20, pp. 7564–7573.

[171] Giglio M., Manes A., Vigano F. Ductile fracture locus of Ti–6Al–4V titanium alloy. *International Journal of Mechanical Sciences*, 2012, Vol. 54, Issue 1, pp. 121–135.

[172] Kweon S. Damage at negative triaxiality. *European Journal of Mechanics - A/Solids*, 2012, Vol. 31, Issue 1, pp. 203–212.

[173] Graham S. M., Zhang T., Gao X., Hayden M. Development of a combined tension–torsion experiment for calibration of ductile fracture models under conditions of low triaxiality. *International Journal of Mechanical Sciences*, 2012, Vol. 54, Issue 1, pp. 172–181.

[174] Hammer J. T. *Plastic deformation and ductile fracture of Ti-6Al-4V under various loading conditions.* M.Sc. Thesis, Ohio State University, 2012.

[175] Khan A. S., Liu H. A new approach for ductile fracture prediction on Al 2024-T351 alloy. *International Journal of Plasticity*, 2012, Vol. 35, pp. 1–12.

[176] Zhu X.-K., Joyce J. A. Review of fracture toughness (G, K, J, CTOD, CTOA) testing and standardization. *Engineering Fracture Mechanics*, 2012, Vol. 85, pp. 1–46.

[177] Wu S. R., Gu L. *Introduction to the explicit finite element method for nonlinear transient dynamics.* John Wiley & Sons, Hoboken, New Jersey, 2012, ISBN: 978-0-470-57237-5.

[178] Luo M. *Anisotropic ductile fracture of metal sheets: Experimental investigation and constitutive modeling.* Ph.D. Thesis, Massachusetts Institute of Technology, 2012.

[179] Lou Y., Huh H., Lim S., Pack K. New ductile fracture criterion for prediction of fracture forming limit diagrams of sheet metals. *International Journal of Solids and Structures*, 2012, Vol. 49, Issue 25, pp. 3605–3615.

[180] Tsiloufas S., Plaut R. Ductile fracture characterization for medium carbon steel using continuum damage mechanics. *Materials Sciences and Applications*, 2012, Vol. 3, No. 11, pp. 745–755.

[181] Luo M., Dunand M., Mohr D. Experiments and modeling of anisotropic aluminum extrusions under multi-axial loading – Part II: Ductile fracture. *International Journal of Plasticity*, 2012, Vols. 32–33, pp. 36–58.

[182] Saanouni K. *Damage mechanics in metal forming: Advanced modeling and numerical simulation.* John Wiley & Sons, Hoboken, 2012, ISBN: 978-1-84821-348-7.

[183] Zhang T. *Development of plasticity and ductile fracture models involving three stress invariants.* Ph.D. Thesis, The University of Akron, 2012.

[184] Gruben G., Hopperstad O. S., Børvik T. Evaluation of uncoupled ductile fracture criteria for the dual-phase steel Docol 600DL. *International Journal of Mechanical Sciences*, 2012, Vol. 62, Issue 1, pp. 133–146.

[185] Benzerga A. A., Surovik D., Keralavarma S. M. On the path-dependence of the fracture locus in ductile materials – Analysis. *International Journal of Plasticity*, 2012, Vol. 37, pp. 157–170.

[186] Zhou J., Gao X., Hayden M., Joyce J. A. Modeling the ductile fracture behavior of an aluminum alloy 5083-H116 including the residual stress effect. *Engineering Fracture Mechanics*, 2012, Vol. 85, pp. 103–116.

[187] Beese A. M., Mohr D. Anisotropic plasticity model coupled with Lode angle dependent strain-induced transformation kinetics law. *Journal of the Mechanics and Physics of Solids*, 2012, Vol. 60, Issue 11, pp. 1922–1940.

[188] De Borst R., Crisfield M. A., Remmers J. J. C., Verhoosel C. V. *Nonlinear finite element analysis of solids and structures.* John Wiley & Sons, Chichester, 2012, ISBN: 978-0-470-66644-9.

[189] Abbassi F., Belhadj T., Mistou S., Zghal A. Parameter identification of a mechanical ductile damage using artificial neural networks in sheet metal forming. *Materials & Design*, 2013, Vol. 45, pp. 605–615.

[190] Gruben G., Hopperstad O. S., Børvik T. Simulation of ductile crack propagation in dual-phase steel. *International Journal of Fracture*, 2013, Vol. 180, Issue 1, pp. 1–22.

[191] Cao T.-S., Gaillac A., Montmitonnet P., Bouchard P.-O. Identification methodology and comparison of phenomenological ductile damage models via hybrid numerical–experimental analysis of fracture experiments conducted on a zirconium alloy. *International Journal of Solids and Structures*, 2013, Vol. 50, Issue 24, pp. 3984–3999.

[192] Fansi J., Balan T., Lemoine X., Maire E., Landron C., Bouaziz O., Bettaieb M. B., Habraken A. M. Numerical investigation and experimental validation of physically based advanced GTN model for DP steels. *Materials Science and Engineering: A*, 2013, Vol. 569, pp. 1–12.

[193] Komori K. Simulation of crack arrest in blanking using the node separation method. *International Journal of Mechanical Sciences*, 2013, Vol. 68, pp. 150–159.

[194] Lou Y., Huh H. Extension of a shear-controlled ductile fracture model considering the stress triaxiality and the Lode parameter. *International Journal of Solids and Structures*, 2013, Vol. 50, Issue 2, pp. 447–455.

[195] Broumand P., Khoei A. R. The extended finite element method for large deformation ductile fracture problems with a non-local damage-plasticity model. *Engineering Fracture Mechanics*, 2013, Vols. 112–113, pp. 97–125.

[196] Mirone G., Corallo D. Stress–strain and ductile fracture characterization of an X100 anisotropic steel: Experiments and modelling. *Engineering Fracture Mechanics*, 2013, Vol. 102, pp. 118–145.

[197] Buyuk M. *Development of a tabulated thermo-viscoplastic material model with regularized failure for dynamic ductile failure prediction of structures under impact loading.* Ph.D. Thesis, The George Washington University, 2013.

[198] Fabrègue D., Landron C., Bouaziz O., Maire E. Damage evolution in TWIP and standard austenitic steel by means of 3D X ray tomography. *Materials Science and Engineering: A*, 2013, Vol. 579, pp. 92–98.

[199] Woelke P. B., Shields M. D., Abboud N. N., Hutchinson J. W. Simulations of ductile fracture in an idealized ship grounding scenario using phenomenological damage and cohesive zone models. *Computational Materials Science*, 2013, Vol. 80, pp. 79–95.

[200] Haltom S. S., Kyriakides S., Ravi-Chandar K. Ductile failure under combined shear and tension. *International Journal of Solids and Structures*, 2013, Vol. 50, Issue 10, pp. 1507–1522.

[201] Lou Y., Huh H. Prediction of ductile fracture for advanced high strength steel with a new criterion: Experiments and simulation. *Journal of Materials Processing Technology*, 2013, Vol. 213, Issue 8, pp. 1284–1302.

[202] Cao T.-S. *Modeling ductile damage for complex loading paths.* Ph.D. Thesis, École Nationale Supérieure des Mines de Paris, 2013.

[203] Seidt J. D., Gilat A. Plastic deformation of 2024-T351 aluminum plate over a wide range of loading conditions. *International Journal of Solids and Structures*, 2013, Vol. 50, Issue 10, pp. 1781–1790.

[204] Björklund O., Larsson R., Nilsson L. Failure of high strength steel sheets: Experiments and modelling. *Journal of Materials Processing Technology*, 2013, Vol. 213, Issue 7, pp. 1103–1117.

[205] Ebnoether F., Mohr D. Predicting ductile fracture of low carbon steel sheets: Stress-based versus mixed stress/strain-based Mohr–Coulomb model. *International Journal of Solids and Structures*, 2013, Vol. 50, Issues 7–8, pp. 1055–1066.

[206] Kroon M., Faleskog J. Numerical implementation of a J_2- and J_3-dependent plasticity model based on a spectral decomposition of the stress deviator. *Computational Mechanics*, 2013, Vol. 52, Issue 5, pp. 1059–1070.

[207] Malcher L., Reis F. J. P., Pires F. M. A., César de Sá J. M. A. Evaluation of shear mechanisms and influence of the calibration point on the numerical results of the GTN model. *International Journal of Mechanical Sciences*, 2013, Vol. 75, pp. 407–422.

[208] Xue Z., Faleskog J., Hutchinson J. W. Tension–torsion fracture experiments – Part II: Simulations with the extended Gurson model and a ductile fracture criterion based on plastic strain. *International Journal of Solids and Structures*, 2013, Vol. 50, Issues 25–26, pp. 4258–4269.

[209] Kofiani K., Nonn A., Wierzbicki T. New calibration method for high and low triaxiality and validation on SENT specimens of API X70. *International Journal of Pressure Vessels and Piping*, 2013, Vols. 111–112, pp. 187–201.

[210] Pereira J. C. R., de Jesus A. M. P., Xavier J., Fernandes A. A. Ultra low-cycle fatigue behaviour of a structural steel. *Engineering Structures*, 2014, Vol. 60, pp. 214–222.

[211] Ranjbar M., Mashayekhi M., Parvizian J., Düster A., Rank E. Using the finite cell method to predict crack initiation in ductile materials. *Computational Materials Science*, 2014, Vol. 82, pp. 427–434.

[212] Lou Y., Yoon J. W., Huh H. Modeling of shear ductile fracture considering a changeable cut-off value for stress triaxiality. *International Journal of Plasticity*, 2014, Vol. 54, pp. 56–80.

[213] Španiel M., Prantl A., Džugan J., Růžička J., Moravec M., Kuželka J. Calibration of fracture locus in scope of uncoupled elastic–plastic-ductile fracture material models. *Advances in Engineering Software*, 2014, Vol. 72, pp. 95–108.

[214] Erice B., Gálvez F. A coupled elastoplastic-damage constitutive model with Lode angle dependent failure criterion. *International Journal of Solids and Structures*, 2014, Vol. 51, Issue 1, pp. 93–110.

[215] Tutyshkin N., Müller W. H., Wille R., Zapara M. Strain-induced damage of metals under large plastic deformation: Theoretical framework and experiments. *International Journal of Plasticity*, 2014, Vol. 59, pp. 133–151.

[216] Pack K., Luo M., Wierzbicki T. Sandia Fracture Challenge: Blind prediction and full calibration to enhance fracture predictability. *International Journal of Fracture*, 2014, Vol. 186, Issues 1–2, pp. 155–175.

[217] Malcher L., Mamiya E. N. An improved damage evolution law based on continuum damage mechanics and its dependence on both stress triaxiality and the third invariant. *International Journal of Plasticity*, 2014, Vol. 56, pp. 232–261.

[218] Cláudio R. A., Reis L., Freitas M. Biaxial high-cycle fatigue life assessment of ductile aluminium cruciform specimens. *Theoretical and Applied Fracture Mechanics*, 2014, Vol. 73, pp. 82–90.

[219] Kõrgesaar M., Romanoff J. Influence of mesh size, stress triaxiality and damage induced softening on ductile fracture of large-scale shell structures. *Marine Structures*, 2014, Vol. 38, pp. 1–17.

[220] Cao T.-S., Gachet J.-M., Montmitonnet P., Bouchard P.-O. A Lode-dependent enhanced Lemaitre model for ductile fracture prediction at low stress triaxiality. *Engineering Fracture Mechanics*, 2014, Vols. 124–125, pp. 80–96.

[221] Papasidero J., Doquet V., Mohr D. Determination of the effect of stress state on the onset of ductile fracture through tension-torsion experiments. *Experimental Mechanics*, 2014, Vol. 54, Issue 2, pp. 137–151.

[222] Kiran R., Khandelwal K. Gurson model parameters for ductile fracture simulation in ASTM A992 steels. *Fatigue & Fracture of Engineering Materials & Structures*, 2014, Vol. 37, Issue 2, pp. 171–183.

[223] Abaqus. *Abaqus 6.14 Documentation.* Dassaul Systèmes Simulia Corporation, Providence, Rhode Island, 2014.

[224] Hůlka J. *Computational prediction of ductile fracture.* Ph.D. Thesis, Brno University of Technology, 2014 (in Czech).

[225] Zhou J., Gao X., Sobotka J. C., Webler B. A., Cockeram B. V. On the extension of the Gurson-type porous plasticity models for prediction of ductile fracture under shear-dominated conditions. *International Journal of Solids and Structures*, 2014, Vol. 51, Issue 18, pp. 3273–3291.

[226] Roth Ch. C., Mohr D. Effect of strain rate on ductile fracture initiation in advanced high strength steel sheets: Experiments and modeling. *International Journal of Plasticity*, 2014, Vol. 56, pp. 19–44.

[227] Mohr D., Marcadet S. J. Micromechanically-motivated phenomenological Hosford–Coulomb model for predicting ductile fracture initiation at low stress triaxialities. *International Journal of Solids and Structures*, 2015, Vols. 67–68, pp. 40–55.

[228] Bai Y., Wierzbicki T. A comparative study of three groups of ductile fracture loci in the 3D space. *Engineering Fracture Mechanics*, 2015, Vol. 135, pp. 147–167.

[229] Marcadet S. J., Mohr D. Effect of compression–tension loading reversal on the strain to fracture of dual phase steel sheets. *International Journal of Plasticity*, 2015, Vol. 72, pp. 21–43.

[230] Basu S., Benzerga A. A. On the path-dependence of the fracture locus in ductile materials: Experiments. *International Journal of Solids and Structures*, 2015, Vol. 71, pp. 79–90.

[231] Wang K., Greve L., Wierzbicki T. FE simulation of edge fracture considering pre-damage from blanking process. *International Journal of Solids and Structures*, 2015, Vol. 71, pp. 206–218.

[232] Papasidero J., Doquet V., Mohr D. Ductile fracture of aluminum 2024-T351 under proportional and non-proportional multi-axial loading: Bao–Wierzbicki results revisited. *International Journal of Solids and Structures*, 2015, Vols. 69–70, pp. 459–474.

[233] Kubík P. *Implementation, calibration and application of ductile fracture conditions in FEM programs.* Ph.D. Thesis, Brno University of Technology, 2015 (in Czech).

[234] Algarni M., Bai Y., Choi Y. A study of Inconel 718 dependency on stress triaxiality and Lode angle in plastic deformation and ductile fracture. *Engineering Fracture Mechanics*, 2015, Vol. 147, pp. 140–157.

[235] Ma H., Xu W., Cheng Jin B., Shan D., Nutt S. R. Damage evaluation in tube spinnability test with ductile fracture criteria. *International Journal of Mechanical Sciences*, 2015, Vol. 100, pp. 99–111.

[236] Gilioli A., Manes A., Giglio M., Wierzbicki T. Predicting ballistic impact failure of aluminium 6061-T6 with the rate-independent Bao–Wierzbicki fracture model. *International Journal of Impact Engineering*, 2015, Vol. 76, pp. 207–220.

[237] Gu G., Mohr D. Anisotropic Hosford–Coulomb fracture initiation model: Theory and application. *Engineering Fracture Mechanics*, 2015, Vol. 147, pp. 480–497.

[238] Růžička J. *Method of fracture locus calibration and a stochastic modification of the uncoupled ductile damage material models.* Ph.D. Thesis, Czech Technical University in Prague, 2015 (in Czech).

[239] Kubík P., Šebek F., Hůlka J., Petruška J. Calibration of ductile fracture criteria at negative stress triaxiality. *International Journal of Mechanical Sciences*, 2016, Vols. 108–109, pp. 90–103.

[240] Tancogne-Dejean T., Roth Ch. C., Woy U., Mohr D. Probabilistic fracture of Ti–6Al–4V made through additive layer manufacturing. *International Journal of Plasticity*, 2016, Vol. 78, pp. 145–172.

[241] Roth Ch. C., Mohr D. Ductile fracture experiments with locally proportional loading histories. *International Journal of Plasticity*, 2016, Vol. 79, pp. 328–354.

[242] Šebek F., Kubík P., Hůlka J., Petruška J. Strain hardening exponent role in phenomenological ductile fracture criteria. *European Journal of Mechanics - A/Solids*, 2016, Vol. 57, pp. 149–164.

Nomenclature

Latin symbols

a	material constant
A	loading asymmetry parameter
$A_1, \ldots, A_3$	material constants
A_B, B_B, C_B, D_B	material constants
A_{JC}, B_{JC}, C_{JC}, D_{JC}	material constants
$B_1, \ldots, B_6$	material constants
c	fatigue ductility exponent
c_η, c_θ^s, c_θ^{ax}	material constants
C	fracture strain correction coefficient
$C_1, \ldots, C_4$	material constants
C_B	material constant
C_{CL}	material constant
C_F	material constant
C_L	parameter representing the cut-off value sensitivity
C_{MCL}	material constant
C_{RT}	material constant
d	actual diameter of cylindrical bar
d_0	initial diameter of cylindrical bar
d_f	diameter of round bar specimen after fracture test
d_h	diameter of the hole
D	damage parameter related to reduction of ductility
D_0	initial amount of damage
$D_1, \ldots, D_6$	material constants
D_c	critical damage
D_{cr}	critical value of damage parameter
D_f	fatigue damage
D_p	damage parameter at the moment of crack initiation
D_{RTCL}	critical damage
D_s	damage parameter related to reduction of load carrying area
$\boldsymbol{\mathcal{D}}$	elastic stiffness tensor
e	engineering strain
e^p	deviatoric plastic strain
E	Young's modulus

$E_1,\ E_2$	material constants
$\tilde{E}$	actual degraded Young's modulus
$f^\star$	void volume function
$f_1, \ldots, f_3$	normalized Lode angle dependent trigonometric functions
f_c	critical value of void volume fraction
f_F	void volume fraction at fracture
f_G	void volume fraction
F	force
F_f	relative hole growth factor
g	parabolic function governing the cut-off
$\mathbf{G}$	matrix of material constants
$G_1, \ldots, G_6$	material constants
h	cylinder height
i	number of particular fracture test
$\mathbf{I}$	identity matrix
I_1	first invariant of the Cauchy stress tensor
$J_2,\ J_3$	second and third invariants of the stress deviator, respectively
k	yield correction function
$\hat{k}$	Lode dependence exponent
K	strength coefficient
Δl	elongation
l_0	gauge length
$L_1, \ldots, L_3$	material constants
m	damage exponent
$\bar{m}$	weakening parameter
M	number of all fracture tests
$M_1, \ldots, M_5$	material constants
n	strain hardening exponent
$\tilde{n}$	plastic flow direction
N	number of cycles
$N_1, \ldots, N_5$	material constants
N_f	number of cycles to fracture
N_r	reference life coefficient
p	hydrostatic pressure
p_{lim}	limiting pressure
q	hydrostatic axis where the principal stresses are equal
$\hat{q}$	shape parameter
q_1, q_2	material constants
q_{GTN}	material constant
r	radius in the cylindrical coordinate system
r_c	critical distance
R	notch or neck radius
s	engineering stress
s_r	material dependence parameter
S	deviatoric stress
S_0	initial cross-sectional area

S_1, S_2, S_3	first, second and third principal stress deviators, respectively
S_r	temperature dependence parameter
t	time
T	temperature
T_h	homologous temperature
T_m	melting temperature
T_r	room temperature
v	wave velocity
w	weakening factor
w_1	hydrostatic pressure weighting function
w_2	asymmetric strain weighting function
$W_1, \ldots, W_3$	material constants
x, y, z	Cartesian or spatial coordinates
Y	damage strain energy release rate

Greek symbols

α	exponent of damage
β	weakening exponent
γ	material constant
$\hat{\gamma}$	fracture strain ratio
ε	error
ϵ	true strain
$\bar{\epsilon}$	total equivalent strain
ϵ^0	reference strain
ϵ_{I}, ϵ_{II}, ϵ_{III}	first, second and third principal plastic strains, respectively
$\dot{\bar{\epsilon}}^0$	reference strain rate
ϵ^e	elastic strain
$\tilde{\epsilon}^e$	effective elastic strain
ϵ'_f	fatigue ductility coefficient
$\bar{\epsilon}^f$	fracture strain
$\hat{\epsilon}^f$	fracture strain for a given loading path
$\bar{\epsilon}^{f,1}$	fracture strain of specimen number 1
$\bar{\epsilon}^{f,2}$	fracture strain of specimen number 2
$\bar{\epsilon}^{f,12}$	fracture strain of specimen 1 after prestraining using specimen 2
$\tilde{\epsilon}^f$	uniaxial tensile fracture strain without confining pressure
ϵ^p	plastic strain
$\tilde{\epsilon}^p$	effective plastic strain
$\bar{\epsilon}^p$	cumulative equivalent plastic strain
$\bar{\epsilon}^{pl}$	instantaneous equivalent plastic strain
$\bar{\epsilon}^{p,0}$	value of prestrain
$\epsilon^{p,a}$	plastic strain amplitude
$\bar{\epsilon}^{th}$	damage strain threshold
$\dot{\tilde{\epsilon}}^{p\star}$	dimensionless effective plastic strain rate

$\dot{\bar{\epsilon}}^{p\star}$	dimensionless equivalent plastic strain rate
η	stress triaxiality
η_0	reference value of stress triaxiality
η_{av}	average stress triaxiality
$\bar{\theta}$	normalized Lode angle
θ_A	azimuth angle
θ_L	Lode angle
κ	curvature in polar coordinates
$\bar{\kappa}$	curvature in Cartesian coordinates
λ	plastic multiplier
μ	Lode parameter
ν	Poisson's ratio
ξ	normalized third invariant of deviatoric stress tensor
ξ_{av}	average normalized third invariant of deviatoric stress tensor
ρ	density
ϱ	polar coordinate of the yield surface in the deviatoric plane
$\boldsymbol{\sigma}$	Cauchy stress tensor
$\tilde{\sigma}$	effective stress
$\bar{\sigma}$	equivalent stress
σ_1, σ_2, σ_3	first, second and third principal stresses, respectively
σ_a	applied stress in major direction
σ_b	applied stress in minor direction
σ_m	mean stress
σ_M	equivalent matrix stress
σ_z	axial stress
σ_Y	yield stress
φ	elevation angle in the spherical coordinate system
Φ	yield function
ω	normalized Lode parameter
ω_0	material constant

Notations

$(\cdot)$	dot product or scalar product or inner product
$(:)$	double dot product or contraction of tensors
$\overrightarrow{(\ )}$	vector
$\lvert\ \rvert$	absolute value
$\lVert\ \rVert$	norm of the vector
$\langle\ \rangle$	Macaulay bracket notation denoting the positive part
$\dot{(\ )}$	time derivative
tr( )	trace
det( )	determinant
boldface	denotes tensors

Abbreviations

AA	Aluminium Alloy
CDM	Continuum Damage Mechanics
DIC	Digital Image Correlation
EDS	Energy Dispersive X-ray Spectroscopy
FEA	Finite Element Analysis
FEM	Finite Element Method
FLD	Forming Limit Diagram
FFLD	Fracture Forming Limit Diagram
GTN	Gurson Tvergaard Needleman
KHPS	Kubík Hůlka Petruška Šebek
KHPS2	Kubík Hůlka Petruška Šebek 2
RTCL	Rice Tracey Cockcroft Latham
RVE	Representative Volume Element
VUMAT	Vectorized User MATerial
XFEM	eXtended Finite Element Method

List of Tables

List of Figures

A Tensile tests of flat plate specimens

There were conducted 3 tensile tests of flat plate specimens, as depicted in Figure A.1, which should describe the plane strain under high stress triaxiality[26].

Zwick Z250 Allround-Line, tCII, and extensometer Zwick multiXtens were used for tensile testing under the displacement control. To ensure the quasi-static loading, the test speed was 1 mm/min during the whole test. The gauge length was 22 mm.

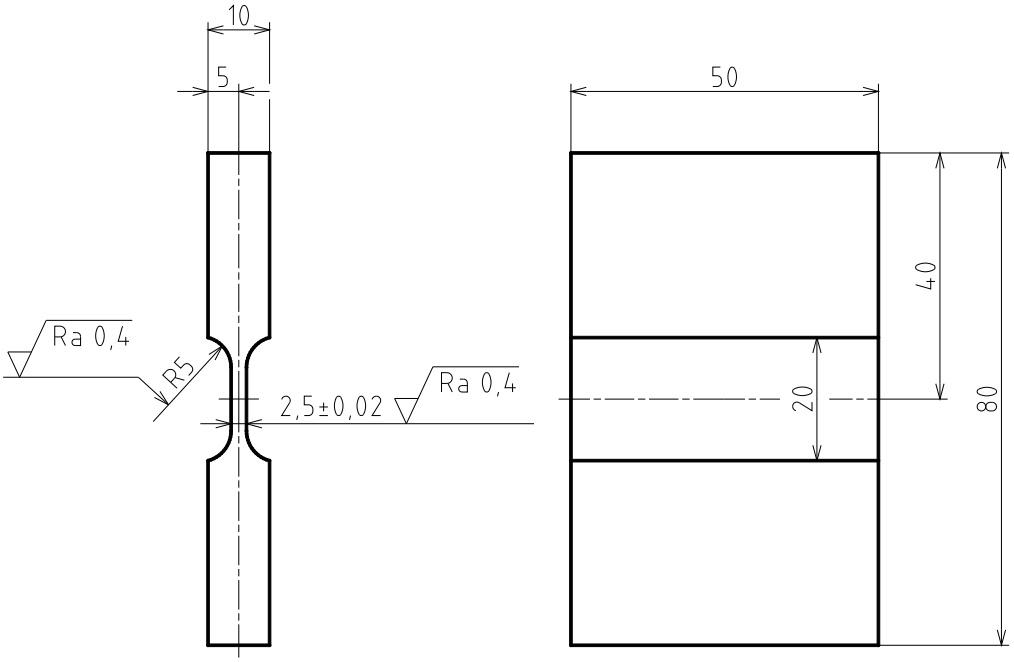

Figure A.1: Detailed drawing of the flat plate specimen.

Post-mortem specimens are depicted in Figure A.2 where the slant fracture may be clearly observed and which is consistent with results obtained by Teng [143].

Force–displacement responses from average experiment together with the ones from simulations are depicted in Figure 9.6a.

[26] There were also tested another grooved plate specimens where various stress triaxialities were achieved by changing the groove radius. Those were designed in order to have the same stress triaxialities as tensile notched cylindrical specimens with sharper notch radii. Unfortunately, the situation was the same or worse than in case of flat plate, so only the flat plate specimen is described in detail.

Figure A.2: Post-mortem flat plate specimens.

Simulations were performed the same as in Chapters 6 and 8. One eighth of geometry was discretized with C3D8R 8-node linear brick elements with reduced integration, hourglass control and characteristic size of 0.075 mm across the thickness and 1.25 mm along the width. Semi-automatic mass scaling was employed to target time increment of $1 \cdot 10^{-7}$ s, similarly as previously. The time increment for most critical elements without accounting for mass scaling was approximately $2.6 \cdot 10^{-9}$ s. The kinetic energy was compared to the internal one so as to ensure that there were negligible dynamic effects.

There are depicted histories of normalized Lode angle for von Mises and Kroon–Faleskog plasticities in Figure A.3b. It is clear that the Kroon–Faleskog plasticity had tendency to describe the state as plane stress in contrary to von Mises plasticity and theoretical value of $\bar{\theta} = 0$. The initial stress triaxiality is theoretically $\sqrt{3}/3$. Average stress triaxiality given by von Mises plasticity was 0.5384 and by Kroon–Faleskog plasticity 0.3954.

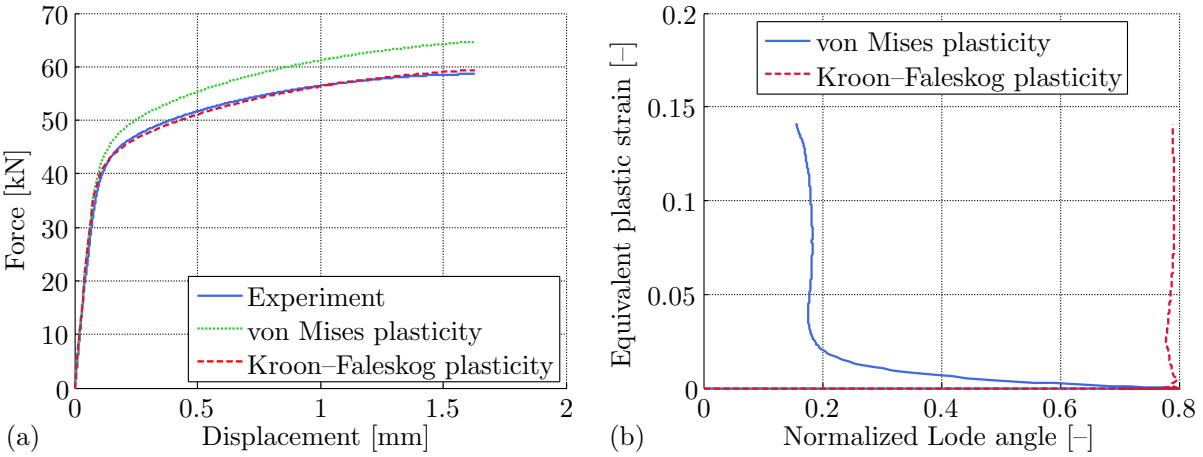

Figure A.3: Flat plate specimen: (a) force–displacement responses for simulations and average experiment; (b) evolutions of normalized Lode angles during loading.

This problem was alo reported by Kroon and Faleskog [206]. The stronger the Lode dependence of plasticity was, the more the problem was significant. Algarni et al. [234] presented modification of I_1, J_2 and J_3 dependent plasticity with deviatorically associted flow rule proposed by Bai and Wierzbicki [135], and the discrepancy in normalized Lode angle accounted for specimen geometry, which is probably not the case. It might be solved by using the non-associative flow rule as in [160].

B Case study of using different damage accumulation laws

The importance of damage accumulation form arises especially with nonproportional loading. There is shown the difference between linear and nonlinear damage accumulation for damage exponents $m = 1$ and $m = 2$ of Equation 7.1. Different stress states causes different fracture strains as in Figure 3.1. If the specimen was loaded under some certain hydrostatic pressure, which would cause fracture strain 0.3, not until fracture but only to some level of equivalent plastic strain, 0.15 in this case, and then pulled under the hydrostatic pressure higher than the previous one, which would cause fracture strain 0.5, until fracture, it has to be less than 0.5 to satisfy the condition of Equation 7.2. The whole situation is illustrated in Figure B.1.

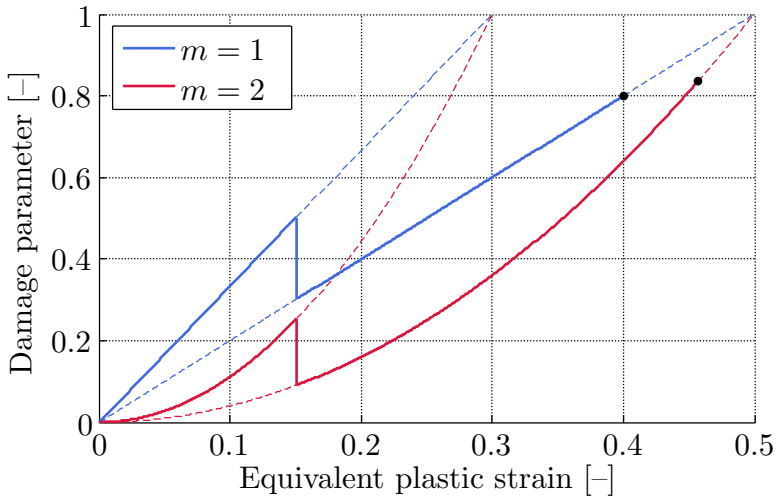

Figure B.1: Damage evolutions plotted with the usage of linear and nonlinear laws.

It is clear that these two cases do not result in the same value of final fracture strain. While in case of $m = 1$ the final fracture strain was 0.40, in case of $m = 2$ the final fracture strain was approximately 0.46.

It might be crucial to use correct damage evolution law especially within complex loading paths induced in real industrial applications where the errors due to incorrectly predicted fracture initiation might distort the solution of whole problem.

The issue was described using variations in stress triaxiality which have large impact. Nevertheless, the same conclusion implies to varying the deviatoric stress state, of course. Therefore, there is not an one to one relationship between fracture strain and average state variables for nonradial loadings [185].

C Damage exponent calculations

Here follows the damage exponent calculations derived from stepwise experiments of Marini et al. [69] and Tai [74]. It exhibits considerable scatter in results (Tables C.1–C.3).

Table C.1: Damage exponents for A508 medium strength steel [69].

$\bar{\epsilon}_{p,0}$ [–]	$\bar{\epsilon}_{f,1}$ [–]	$\bar{\epsilon}_{f,2}$ [–]	$\bar{\epsilon}_{f,12}$ [–]	m [–]
0.3093	0.6172	0.3865	0.4296	3.08
0.3113			0.4305	3.07
0.4365			0.5180	1.89
0.4927			0.5657	1.16
0.3093	0.6172	0.4673	0.4893	3.19
0.4596			0.5593	1.80
0.4748			0.5558	2.30
0.4927			0.5670	2.03

Table C.2: Damage exponents for low carbon steel No. 20 [74].

$\bar{\epsilon}_{p,0}$ [–]	$\bar{\epsilon}_{f,1}$ [–]	$\bar{\epsilon}_{f,2}$ [–]	$\bar{\epsilon}_{f,12}$ [–]	m [–]
0.20	0.75	0.39	0.53	0.66
0.30	1.05	0.57	0.65	1.55
0.38	1.05	0.75	0.85	1.09
0.50	1.15	0.90	1.08	0.37

Table C.3: Damage exponents for low carbon steel A3 [74].

$\bar{\epsilon}_{p,0}$ [–]	$\bar{\epsilon}_{f,1}$ [–]	$\bar{\epsilon}_{f,2}$ [–]	$\bar{\epsilon}_{f,12}$ [–]	m [–]
0.30	1.07	0.58	0.72	0.98
0.40	1.10	0.80	0.95	0.66
0.43	1.10	0.80	0.98	0.51
0.50	1.10	0.80	1.05	0.21